Characterization of Residual Stress and Precipitate Evolution in Aluminum 2xxx Self-Reacting Friction Stir Welds

A Dissertation Presented for the
Doctor of Philosophy
Degree
The University of Tennessee, Knoxville

Benjamin Joe Wing
August 2023

Copyright © 2023 by Benjamin Joe Wing
All rights reserved.

ACKNOWLEDGEMENTS

The author would like to acknowledge partial support though the Manufacturing and Materials Joining Innovation Center (Ma2JIC) University of Tennessee, Knoxville site. Ma2JIC is funded by the National Science Foundation (NSF) through the Industry/University Cooperative Research Center (I/UCRC) program award number IIP 1822186.

This research used resources at the High Flux Isotope Reactor a DOE Office of Science User Facility operated by the Oak Ridge National Laboratory.

This research used resources of the Advanced Photon Source, a U.S. Department of Energy (DOE) Office of Science user facility operated for the DOE Office of Science by Argonne National Laboratory under Contract No. DE-AC02-06CH11357.

This research used resources of the Diffraction Facility at the Institute for Advanced Materials and Manufacturing.

This research used resources of the Polymer Characterization Laboratory at the Institute for Advanced Materials and Manufacturing.

ABSTRACT

2xxx series aluminum alloys possess attractive properties for structural aerospace applications including high strength to weight ratio, corrosion resistance, and stable cryogenic performance. Solid state joining processes are often employed to reduce weld defects and improve weld performance/consistency as many alloys of this range have poor weldability for traditional fusion based joining techniques. One such process, self-reacting friction stir welding (SRFSW) allows for consistent high-quality, welding of large and curved articles is often used in the construction of large structures such as launch vehicle liquid propellant tanks.

Despite the merits of this process, joint softening (a decrease in mechanical properties related to the base material) remains a persistent issue. This phenomenon has two principal sources: residual stresses formed due to the thermomechanical nature and high restraint conditions involved and coarsening/over-ageing of strengthening precipitates.

This research focuses on the evaluation of aluminum 2xxx SRFSWs via neutron scattering methods. Residual stress was evaluated in the longitudinal, normal, and transverse directions via neutron diffraction and quantified throughout the entire subsurface region and informed by metallography and microhardness studies. Precipitate evolution evaluation was carried out via small-angle scattering (SAS) techniques and supported by scanning electron microscopy (SEM), x-ray diffraction (XRD), and wide-angle X-ray scattering (WAXS) – pending transmission electron microscopy (TEM) and atom probe tomography (APT). Variations in both residual stress and precipitation are observed and described. Residual stress displayed an ‘M-shaped’ profile with highest tensile values occurring in the thermomechanically affected zone (TMAZ). XRD and WAXS identified three secondary phases: θ [theta] and θ’ [theta prime] precipitates (Al_2Cu) and an intermetallic ω [omega] (Al_7Cu_2Fe). SAS indicates that prior to solvation in the stir zone (SZ) the θ’ [theta prime] precipitates coarsen and decrease in volume fraction to the heat affected zone (HAZ) while the θ [theta] precipitates coarsen and increase in volume fraction to the TMAZ.

TABLE OF CONTENTS

INTRODUCTION 1
CHAPTER I BACKGROUND INFORMATION AND REVIEW OF RESIDUAL STRESS AND PRECIPITATE EVOLUTION 3
Abstract 4
1.1 Aluminum 2000 Series Alloys 4
1.1.1 2219-T87 and 2219-T851 4
1.1.2 2195-T88 and 2195-T8M4 5
1.2 Friction Stir Welding 6
1.2.1 Nomenclature 7
1.2.2 Macrostructure and Microstructure 7
1.2.3 Processing Parameters 8
1.2.4 Dissimilar Material Joining 8
1.3 Self-Reacting Friction Stir Welding 9
1.4 Residual Stress 10
1.4.1 Definition and Theory 10
1.4.2 Residual Stress Characterization Techniques 13
1.4.3 Neutron Diffraction Residual Stress 14
1.4.5 FSW and SRFSW Residual Stress Measurements 20
1.5 Precipitate Evolution 22
1.5.1 Precipitate Strengthening 22
1.5.2 Precipitates of 2219 and 2195 23
1.6 Precipitate Characterization 25
1.6.1 Local Techniques 25
1.6.2 Global Techniques 28
1.7 Small angle scattering (SAS) 29
1.7.1 Principles 29
1.7.2 Mathematical Basis 30
1.7.3 Data Representation 31
1.7.4 Small-angle Scattering in FSW 32
1.8 Aluminum 2xxx (SR)FSW Precipitate Review 33
1.8.1 AA2219 33
1.8.2 AA2195 35
1.8.3 AA2219/AA2195 36
Appendix 37
CHAPTER II NEUTRON DIFFRACTION RESIDUAL STRESS STUDY OF A AA2219-T87 SELF-REACTING FRICTION STIR WELD – PART I 53
2.1 Abstract 54
2.2 Introduction 55
2.3 Experiment/Methods 56
2.3.1 Microstructure 56
2.3.2 Microhardness 57
2.3.3 Neutron Diffraction Measurements 57
2.3.4 Force Balance 60

2.4 Results 61
2.4.1 Macro and Microstructure 61
2.4.2 Microhardness 61
2.4.3 Neutron Diffraction 62
2.5 Discussion 63
2.5.1 Macro-Microstructure 63
2.5.2 Microhardness 65
2.5.3 Strain 66
2.5.3 Stress 66
2.6 Conclusion 68
2.7 Acknowledgements 68
Appendix 69
CHAPTER III NEUTRON DIFFRACTION METHODS FOR RESIDUAL STRESS DETERMINATION IN WELDED ALUMINUM ALLOYS – PART II 77
3.1 Abstract 78
3.2 Introduction and Background 78
3.2.1 Gauge Volume 78
3.2.2 Determination of d-spacing, strain, and residual stress 79
3.3 Sample Considerations 80
3.3.1 Composition Variation and Stress-free Reference (d_0) 80
3.3.2 Sampled Location 81
3.3.3 Texture and Grain Size 82
3.3.4 Sample Preparation 83
3.3.5 Gauge volume selection 83
3.3.6 Chemical Composition 84
3.4 Measurement Considerations 88
3.4.1 Characteristic Peak 88
3.4.2 Partially Buried Gauge Volume 88
3.4.3 Location Selection 89
3.4.4 d_0 Interpolation 91
3.5 Conclusion 92
3.6 Acknowledgements 93
Appendix 94
CHAPTER IV RESIDUAL STRESS STUDY OF DISSIMILAR AA2219/AA2195 SELF-REACTING FRICTION STIR WELDS WITH NEUTRON DIFFRACTION 107
4.1 Abstract 108
4.2 Introduction 109
4.3 Experiment/Methods 111
4.3.1 Microstructure 111
4.3.2 Microhardness 111
4.3.3 Neutron Diffraction Measurements 112
4.3.4 Force Balance 114
4.4 Results 115
4.4.1 Macro and Microstructure 115
4.4.2 Microhardness 115

4.4.3 Neutron Diffraction 116
4.5 Discussion 117
4.5.1 Macro-Microstructure 118
4.5.2 Microhardness 118
4.5.3 Strain 119
4.5.4 Stress 119
4.6 Conclusion 120
4.7 Acknowledgements 121
Appendix 122
CHAPTER V PRECIPITATE EVOLUTION IN A 2219-T87 SELF-REACTING FRICTION STIR WELD 131
5.1 Abstract 132
5.2 Introduction 133
5.3 Experiment/Methods 134
5.3.1 Microstructure 134
5.3.2 Microhardness 135
5.3.3 X-ray Fluorescence (XRF) 135
5.3.4 X-ray Diffraction (XRD) 135
5.3.5 Small-angle Neutron Scattering (SANS) 135
5.3.6 USAXS/SAXS/WAXS 136
5.4 Results 137
5.4.1 Macro and Microstructure 137
5.4.2 Microhardness 137
5.4.3 X-ray Fluorescence (XRF) 137
5.4.4 HTXRD 137
5.4.5 WAXS 138
5.4.6 Small-angle Neutron Scattering 138
5.4.7 USAXS/SAXS 140
5.5 Discussion 141
5.5.1 Micro-Macrostructure 141
5.5.2 Microhardness 141
5.5.3 X-ray Fluorescence (XRF) 142
5.5.4 HTXRD 142
5.5.5 WAXS 143
5.5.6 Small-angle Scattering 144
5.6 Conclusion 145
5.7 Acknowledgements 145
Appendix 147
REFERENCES 162
VITA 172

LIST OF TABLES

Table A1-1: Composition limits of AA2219 (wt.%) [5] 37
Table A1-2: Composition limits of AA2195 (wt.%) [13] 37
Table A1-3: Comparison of residual stress measurement techniques adapted from [35] 42
Table A1-4: Advantages and disadvantages of residual stress measurement techniques [29] 43
Table A1-5: Lattice planes and intergranular strain response *adapted from* [32] 46
Table A1-6: Literature for SAXS precipitate characterization in aluminum alloys 51
Table A1-7: Literature for SANS precipitate characterization 52
Table A1-8: DSC Analysis results of different samples [58] 52
Table A1-9: Observed precipitate phases and weld locations *adapted from* [59] 52
Table A2-1: Image analysis of macroprecipitates from optical micrographs - number and linear number density for each weld zone 71
Table A2-2: Grain size comparison for 2219-T87 SRFSW 76
Table A3-1: Residual stress difference (maximum and minimum values) after force balance application 101
Table A3-2: Copper concentration (at%), a_0 (Å), *d*-spacing (Å), microstrain difference, and stress difference (MPa) 102
Table A3-3: Lattice planes and intergranular strain response *adapted from* [32] 102
Table A5-1: Image analysis of macroprecipitates from optical micrographs - number and linear number density for each weld zone is given 149
Table A5-2: Composition of 2219-T87 base metal measured via XRF and 2219 composition limits (wt%) [5] 151
Table A5-3: R_g values for each averaging approach 156
Table A5-4: Grain size comparison for 2219-T87 SRFSW 161

LIST OF FIGURES

Figure A1-1 Schematic of the FSW process [18] 37
Figure A1-2 Weld plate and weld directions 38
Figure A1-3 Schematic of FSW zones: (a) Base metal, (b) Heat-affected zone, (c) Thermo-mechanically affected zone, (d) Stir zone adapted from [21] 38
Figure A1-4 SRFSW schematic showing weld process (top) and tool (bottom) [27] 39
Figure A1-5 Cause and effect diagram for defect-free BTFSW joint [25] 39
Figure A1-6 Residual stress length scale variation for (left) Type I, (center) Type II, and (right) Type III [32] 40
Figure A1-7 Three bar problem stresses during (a) heating and (b) cooling *adapted from* [33] 40
Figure A1-8 Stress and temperature change during welding [34] 41
Figure A1-9 Web of Science Literature Search results for the topic “Residual Stress” by year 41
Figure A1-10 Illustration of incident and diffracted beam related to scattering angle change [37] 44
Figure A1-11 Illustration of (a) reactor based diffractometer (b) spallation based diffractometer for residual stress experiment [39] 44
Figure A1-12 Schematic of reactor-based instrument optics (PSD is position-sensitive detector) [41] 44
Figure A1-13 Schematic of gauge and scattering volumes for the transverse, normal, and longitudinal directions 45
Figure A1-14 (a) reflection geometry and (b) transmission geometry [40] 45
Figure A1-15 2θ (311) reflection Ni (a) reflection geometry (b) transmission geometry [40] 45
Figure A1-16 Apparent microstrain vs composition [32] (left) lattice constant vs copper concentration in for the $Al_{1-x}Cu_x$ solid solution [43] (right) 46
Figure A1-17 Typical heat treatment regime for precipitation hardenable aluminum alloys adapted from [4] 46
Figure A1-18 Hypothetical binary phase diagram for a precipitation-hardenable alloy of composition C_0 [51] 47
Figure A1-19 Al-Cu binary phase diagram (left) [51] and with approximate metastable precipitate solvus temperature (right) [52] 47
Figure A1-20 Precipitate strengthening mechanisms: dislocations either shear particles (top) or loop around particles (bottom) [53] 48
Figure A1-21 Age-hardening behavior of Al-Cu system showing the precipitates formed at 150 °C over time and the preferred dislocation motion mechanism 48
Figure A1-22 Effective size range of microscopy and scattering techniques [73] 49
Figure A1-23 Schematic of small-angle scattering [74] 49
Figure A1-24 2D scattering pattern from a dilute solution of identical ellipsoids of principal axis ratio 2:1:1 with (a) the long axis aligned with the z direction and (b) random orientation [73] 50
Figure A1-25 1D SAS pattern information [75] 50

Figure A2-2 Stress-free reference comb illustrating large (blue) and small (orange) gauge volumes 69
Figure A2-4 Average Δd in each direction 70
Figure A2-6 2219-T87 SRFSW macrograph 70
Figure A2-7 Micrographs of each weld zone in 2219-T87 SRFSW 71
Figure A2-8 Horizontal and vertical grain sizes for each weld zone with standard deviation 71
Figure A2-9 Microhardness (top) mid-thickness averaged line graph (1σ) (bottom) contour plot 72
Figure A2-10 Normal, transverse, longitudinal, and d_0 d-spacing 72
Figure A2-11 d-spacing contour plots for (a) d_0, (b) normal, (c) transverse, and (d) longitudinal directions 73
Figure A2-12 FWHM contour plots in the a) normal, b) transverse, and c) longitudinal directions 73
Figure A2-13 Residual strain in the normal, transverse, and longitudinal directions 74
Figure A2-14 Residual strain contour plots in the (a) normal, (b) transverse, and (c) longitudinal directions 74
Figure A2-15 Residual stress in the normal, transverse, and longitudinal directions 75
Figure A2-16 Residual stress contour plots in the (a) normal, (b) transverse, and (c) longitudinal directions 75
Figure A3-1 Schematic of reactor-based instrument optics (PSD is position-sensitive detector) [41] 94
Figure A3-2 Schematic of gauge and scattering volumes for the transverse, normal, and longitudinal directions 94
Figure A3-3 (a) reflection geometry and (b) transmission geometry [40] 94
Figure A3-4 Illustration of incident and diffracted beam related to scattering angle change [37] 95
Figure A3-5 Apparent microstrain vs composition [32] (left) lattice constant vs copper concentration in for the $Al_{1-x}Cu_x$ solid solution [43] (right) 95
Figure A3-6 Apparent microstrain and stress due to chemical and microstructural changes 96
Figure A3-7: Positioning of original 2 x 20 x 2 mm (blue) and 2 x 10 x 2 mm (orange) gauge volumes 96
Figure A3-8: Transverse direction d-spacing measurement for the 80 mm^3 (2 x 20 x 2 mm) and the 40 mm^3 (2 x 10 x 2 mm) gauge volumes at (a) mid-thickness and (b) all thicknesses 97
Figure A3-9: 80 mm^3 and 40 mm^3 gauge volume d-spacing highlighting regions of difference (orange dashed lines) on the advancing and retreating sides 97
Figure A3-10: Regions of interest for EDS measurement highlighted in orange 98
Figure A3-11: Selected sample locations for EDS measurement highlighted in orange and blue 98
Figure A3-12: Composition (at% Cu) of the matrix for 0 mm (saw cut), 15 mm, and 80 mm locations from plate end (error bars are 1σ) 99
Figure A3-13: Calculated lattice parameter (left y-axis) and d-spacing (right y-axis) vs (a) Composition (at% Cu) and (b) sample number 99

Figure A3-14: Calculated microstrain (left axis) and stress difference (right axis) vs sample number 100
Figure A3-15: Calculated microstrain and stress difference (MPa) contour plots for the 80 mm^3 and 40 mm^3 gauge volume measurement conditions across the weld. EDS measurement region is denoted by the dashed lines 100
Figure A3-16: Residual stress comparison (a) with and (b) without application of force balance 100
Figure A3-17 Δd between EDS measurement locations 101
Figure A3-18 Difference between a typical longitudinal residual stress trend (grey) and constant extrapolation (orange) 101
Figure A3-19 2θ (311) reflection Ni (a) reflection geometry (b) transmission geometry [40] 103
Figure A3-20 Transverse direction *d*-spacing measurements for 4mm interval and variable measurement schemes 103
Figure A3-21 Approximate location of measurement planes; initial measurement (orange), repeatability measurements (blue) 104
Figure A3-22 *d*-spacing of transverse direction measurements at (a) +75 mm, (b) +150 mm, (c) +243 mm compared to original measurement position 104
Figure A3-23 *d*-spacing of normal direction measurements at +243 mm compared to original measurement position 105
Figure A3-24 Microstrain and stress difference between transverse direction measurements at (a) +75 mm, (b) +150 mm, (c) +243 mm and the original measurement position 105
Figure A3-25 Mid-thickness d_0 measurements with (a) linear, (b) cubic interpolation, (c) both – enlarged to display trends 106
Figure A3-26 Mid-thickness variable d_0 measurements with linear and cubic interpolation 106
Figure A4-1 Plate geometry for 2195-T88/2219-T87 and (b) 2195-T8M4/2219-T851. 122
Figure A4-2 Weld plates with stress-free reference comb (left) 2195-T88/2219-T87 (right) 2195-T8M4/2219-T851 122
Figure A4-3 2195-T88/2219-T87 SRFSW macrograph 123
Figure A4-4 Micrographs of each weld zone in 2195-T88/2219-T87 SRFSW 123
Figure A4-5 2195-T8M4/2219-T851 SRFSW macrograph 123
Figure A4-6 Micrographs of each weld zone in 2195-T8M4/2219-T851 SRFSW 124
Figure A4-7 Midthickness averaged microhardness plot (a) 2195-T88/2219-T87, (b) 2195-T8M4/2219-T851, (c) dissimilar SRFSWs, and (d) dissimilar and similar SRFSWs 124
Figure A4-8 Microhardness contour plot (a) 2195-T88/2219-T87, (b) 2195-T8M4/2219-T851 125
Figure A4-9 Normal, transverse, longitudinal, and d_0 *d*-spacing (a) 2195-T88/2219-T87 and (b) 2195-T8M4/2219-T851 125
Figure A4-10 2195-T88/2219-T87 *d*-spacing contour plots for (a) normal, (b) transverse, and (c) longitudinal directions 126
Figure A4-11 2195-T8M4/2219-T851 *d*-spacing contour plots for (a) normal, (b) transverse, and (c) longitudinal directions 126

Figure A4-12 2195-T88/2219-T87 FWHM contour plots in the a) normal, b) transverse, and c) longitudinal directions 127
Figure A4-13 2195-T8M4/2219-T851 FWHM contour plots in the a) normal, b) transverse, and c) longitudinal directions 127
Figure A4-14 Residual strain in the normal, transverse, and longitudinal directions for (a) 2195-T88/2219-T87 and (b) 2195-T8M4/2219-T851 128
Figure A4-15 2195-T88/2219-T87 residual strain contour plots in the (a) normal, (b) transverse, and (c) longitudinal directions 128
Figure A4-16 2195-T8M4/2219-T851 residual strain contour plots in the (a) normal, (b) transverse, and (c) longitudinal directions 129
Figure A4-17 Residual stress in the normal, transverse, and longitudinal directions for (a) 2195-T88/2219-T87 and (b) 2195-T8M4/2219-T851 129
Figure A4-18 2195-T88/2219-T87 residual stress contour plots in the (a) normal, (b) transverse, and (c) longitudinal directions 130
Figure A4-19 2195-T8M4/2219-T851 residual stress contour plots in the (a) normal, (b) transverse, and (c) longitudinal directions 130
Figure A5-1 SANS measurement scheme with approximate weld zone locations 147
Figure A5-2 GP-SANS experiment setup 147
Figure A5-3 USAXS/SAXS/WAXS experiment setup 148
Figure A5-4 USAXS/SAXS/WAXS measurement scheme 148
Figure A5-5 2219-T87 SRFSW macrograph 148
Figure A5-6 Micrographs of each weld zone in 2219-T87 SRFSW 149
Figure A5-7 Horizontal and vertical grain sizes for each weld zone with standard deviation 149
Figure A5-8 Mid-thickness averaged line microhardness (1σ error bars) 150
Figure A5-9 Microhardness contour plot 150
Figure A5-10 Fitted XRF spectra of the 2219-T87 base metal 151
Figure A5-11 Stacked plot of 2219-T87 HTXRD data with secondary phases (ω, θ, and θ') noted 152
Figure A5-12 Waterfall plot of background subtracted 2219-T87 HTXRD data indicating secondary phases 152
Figure A5-13 Stacked plot of WAXS data with secondary phases (ω, θ, and θ') noted 153
Figure A5-14 Waterfall plot of midthickness WAXS showing intensity related to position and 2θ with secondary phases noted 153
Figure A5-15 2D SANS patterns of 2219-T87 SRFSW for the (a) base metal, (b) HAZ, and (c) stir zone 154
Figure A5-16 Azimuthally averaged SANS I vs q plots 154
Figure A5-17 SANS I vs q plots for (a) horizontal and (b) vertical wedges 155
Figure A5-18 SANS I vs q plots comparing the horizontal and vertical wedge schemes (a) SZ and (b) BM 155
Figure A5-19 Fitting regions of the base metal and stir zone 155
Figure A5-20 Comparison of Rg values for each averaging strategy (a) Rg1 and (b) Rg2 156
Figure A5-21 Rg comparison for azimuthal and stir zone subtraction methods (a) Rg1 and (b) Rg2 156

Figure A5-22 Relative volume fraction of the L1 and L2 scattering populations (3 point moving average)..... 157
Figure A5-23 Relative volume fraction of the combined fitting levels (L1 and L2)..... 157
Figure A5-24 2219-T87 SRFSW SAXS summed intensity 158
Figure A5-25 Slit-smeared USAXS/SAXS/WAXS I vs q plots at weld midthickness.. 158
Figure A5-26 Midline USAXS/SAXS radius of gyration for (a) L1, (b) L2, (c) L3, and (d) L4 159
Figure A5-27 Normalized microhardness, macroprecipitate number, SAXS intensity, and SANS intensity correlation 160
Figure A5-28 Comparison of midline USAXS/SAXS AND SANS radius of gyration (a) L1 and (b) L2 160
Figure A5-29 2219-T87 HTXRD experiment temperature vs time profile..... 161

INTRODUCTION

Aluminum alloys of the 2xxx series possess high strength and ductility, low density, good corrosion resistance, stable cryogenic performance, and precipitation hardening. These properties make the 2xxx series particularly attractive for structural aerospace applications such as the liquid propellant rocket fuel tanks of NASA's Space Launch System (SLS). Due to its immense size, the SLS core stage tank is constructed with welded panels. Since traditional fusion-based welding processes can produce defects and inconsistency in 2xxx series alloys, joining is accomplished by a solid-state process known as friction stir welding (FSW). In FSW, a rotating tool is pressed against and travels along abutting or overlapping plates. This tool generates frictional heat, softening the material while the shearing action of the shoulder and protruding pin provide mixing and bonding of the plates. The circumferential construction and critical nature of the fuel tanks introduces the need to produce a backing or reactive force and improve weld consistency. For this, a variant of FSW called self-reacting friction stir welding (SRFSW) is employed. SRFSW incorporates two opposing shoulders on the crown and root sides of the weld joint with a connecting pin which produces a consistent, balanced force along the weld. While this configuration achieves its goal, joint softening remains an issue for 2xxx alloys and this process.

Joint softening, a loss of mechanical properties along the weld, in 2xxx alloys is often due to changes in precipitate size and distribution as well as increased residual stresses. In FSW, residual stresses are primarily the result of differences in thermomechanical deformation within the joint under restraint conditions while precipitate over-ageing is due to elevated temperatures during welding, a combination which can negatively impact material performance and hasten failure. Joint softening has been noted in AA6061, AA6056-T78, and AA2024 SRFSWs though the extent of its effects and relation to residual stresses are not well documented. Unfortunately, though a large amount of information on residual stress is available for conventional FSW there is a scarcity of research on residual stress and precipitate evolution for SRFSWs and many 2xxx alloys.

Information obtained from SRFSW weld characterization will be employed toward a predictive modeling effort aimed at residual stress and precipitate evolution prediction and process improvement.

This is a multi-part dissertation with five main chapters:

Chapter 1 The first chapter is background information related to aluminum 2xxx series alloys of interest – 2219 and 2195, FSW, and SRFSW as well as a comprehensive review of residual stress, precipitation, and the relevant characterization techniques with a focus on neutron and X-ray scattering methods.

Chapter 2 The second chapter characterizes the residual stress in a AA2219-T87 SRFSW via neutron diffraction as well as mechanical properties using microhardness and grain size and texture with metallography. Residual stresses were noted to follow an 'M-shaped' distribution in each direction with the highest tensile values approximating the material yield stress.

Chapter 3 The third chapter summarizes methods and corrections for residual stress studies in aluminum alloys. This section contains additional follow-up and data treatment related to the 2219-T87 SRFSW described in Chapter 2.

Chapter 4 The fourth chapter characterizes residual stress in two dissimilar AA2195/AA2219 SRFSWs. An 'M-shaped' distribution was observed for both SRFSWs with maximum residual stress reaching less than 50% of the material yield.

Chapter 5 The fifth chapter uses complementary advanced characterization techniques to determine precipitate identity, morphology, and evolution in a 2219-T87 SRFSW. Two precipitates θ and θ' and an intermetallic were identified with the precipitates increasing in size to the TMAZ and HAZ, respectively. Partial precipitate dissolution was observed toward the SZ.

CHAPTER I
BACKGROUND INFORMATION AND REVIEW OF RESIDUAL STRESS AND PRECIPITATE EVOLUTION

Abstract

In this Chapter, background information will be introduced concerning the aluminum alloys/tempers of focus (2219 and 2195), relevant welding processes (FSW and SRFSW), residual stress, precipitate evolution, and process modeling.

1.1 Aluminum 2000 Series Alloys

Aluminum 2000 series alloys are those in which copper is the principal alloying element and notably consists of Al-Cu, Al-Cu-Li, and Al-Cu-Mg alloys. Alloys in this series possess high strength-to-weight ratios (i.e. specific strength) and see wide use in structural automotive and aerospace applications. [1], [2] These alloys are heat treatable meaning the principal alloying element(s) have increased solid solubility in aluminum with increased temperature. This solubility allows for the formation of small precipitates which can impede dislocation motion and slow plastic deformation (i.e. improvement of mechanical properties such as hardness). [3], [4] This process known as precipitation hardening, or age-hardening, is achieved via a three-stage heat treatment. First, the alloy is heated until it reaches a single-phase region (i.e. alloying elements are solutionized) and quenched to room temperature to prevent diffusion-controlled precipitation solute-rich precipitates, forming a solid-solution. The alloy then undergoes a lower temperature heat treatment in which precipitates form. Precipitate evolution is determined by the time and temperature used and can vary greatly based upon the adopted regime. [3], [4] This concept is detailed in section 3.5.

1.1.1 2219-T87 and 2219-T851

2219, commonly known by the Aluminum Association designation of AA2219, is a precipitation hardenable aluminum-copper alloy which was developed in the early 1950s and received standardization in 1954. [5], [6] 2219 possesses low density, high strength, stable cryogenic performance, high fracture toughness, resistance to stress corrosion cracking, and good weldability. This alloy found primary use in structural aerospace components such as liquid propellant tanks like NASA's External Tank (ET) and Space Launch System (SLS) core stage. [1], [7], [8] The composition range of AA2219 is given by **Table A1-1**.

Cu serves a primary role in solid-solution and precipitation strengthening. Zn adds corrosion resistance and contributes slightly to solid-solution strengthening. Zr and Mn assist in recrystallization and texture control and V raises the recrystallization temperature and improves solidification grain refinement. Impurity elements, Fe and Si, are known to negatively affect fracture toughness, fatigue, and corrosion. [1], [9]

T87 and T851 refer to specific tempers of the alloy. The -T8 designation of both tempers denotes that the material underwent solution heat-treatment and cold working, followed by artificial ageing. [2], [10] Additional digits refer to "a variation in treatment which significantly alters the characteristics of the product". [11] In the case of the T87 condition, this refers to solution heat treatment at 535-545 °C for 20-270 minutes depending on plate thickness, 7% strain hardening, and ageing between 170 ± °C for 18 h. The -TX51 condition refers to stress-relief by stretching following solution heat-treatment by 1.5-3% the permanent set for aluminum plate. In the case of -T851 this results in solution heat treatment at 535-545 °C for 20-270 minutes depending on plate thickness, stress-relief by stretching to 1.5-3% the permanent set for aluminum plate, and ageing between 170 ± °C for 18 h. [2], [10]

1.1.2 2195-T88 and 2195-T8M4

2195, Aluminum Association designation AA2195, is a 3rd generation age-hardenable aluminum-copper-lithium alloy developed by Martin Marietta (now Lockheed Martin) circa 1992 for NASA as a replacement for 2219 in aerospace and cryogenic tank applications. [12] Compared to 2219, 2195 offers improved strength, modulus, and lower density though decreased weldability. [6], [13] In 1994, NASA selected 2195 for incorporation into the Super Light Weight External Tank (SLWT) of the Space Shuttle launch vehicle due to the need for increased lift capability to reach the higher orbital inclination of the International Space Station (ISS) accounting for a weight reduction of approximately 7,500 lbs. [8]

The composition range of AA2195 is given by **Table A1-2**.

The roles of the elemental alloying additions in 2195 are similar to those in 2219 with additions of Li, Ag, Ti, increased levels of Mg, and absence of V. Like, Cu, Ag also serves to improve solid-solution and precipitation strengthening. Li and Mg additions are primarily responsible for density reduction though contribute to solid-solution and precipitation strengthening as well. Ti is responsible for grain refinement improvements during solidification. Impurity elements, Fe and Si, are known to negatively affect fracture toughness, fatigue, and corrosion. [1], [9], [12]

Two tempers examined during this project are T88 and T8M4. The -T88 condition undergoes similar treatment process to the -T87 temper of the previous section except the strain hardening is 8% instead of 7%. Literature on the specifics of the T8M4 temper was not readily available during literature review.

1.2 Friction Stir Welding

Friction stir welding (FSW) is a solid-state joining process developed at The Welding Institute (TWI) in 1991. In FSW a rotating tool consisting of a shoulder and pin travels along abutting or overlapping plates and mixes the joint edges, **Figure A1-1**. Frictional heat produced by the rotating tool softens the material while the shearing action of the tool shoulders and pin provide material mixing and bonding of the plates. [14]–[16]

As FSW is a solid-state process (i.e. melting of the material does not occur), many of the issues associated with traditional fusion based processes can be avoided such as porosity, solidification cracking, oxide formation, thermal distortion from asymmetric heat application, voids, and weakened joints. As such, FSW sees wide use in alloys that have poor weldability with fusion-based processes such as the aluminum 2xxx, 6xxx, and 7xxx series and dissimilar materials joining. [14], [15]

FSW also tends to produce welds with more repeatable and stable properties compared to fusion-based processes. Fusion welding processes also tend to produce higher residual stresses with less repeatability than solid-state processes such as friction stir welding owing in part to greater thermal gradients. [14], [17] Joint efficiency – a ratio of the

ultimate tensile strength (UTS) of the weld compared to the UTS of the alloy – improves from approximately 50-60% for fusion-based processes to upwards of 80% (and theoretically 100%) for FSW adjacent processes. [14], [19], [20] Additionally, improved fatigue performance as well as low weld variability and repair rate make this process ideal for critical service applications.

1.2.1 Nomenclature

There are several unique features and designations related to FSW. The sides of a FSW are referenced in relation to tool rotation and traverse direction. The 'advancing side' (AS) is where tool rotation is aligned with the traverse direction while on the 'retreating side' (RS) tool rotation is opposite the traverse direction, **Figure A1-1**. Convention for micrograph depictions display the RS to the left with the AS on the right. [14] There are three weld directions: longitudinal, transverse, and normal. The longitudinal direction follows the weld traverse, the transverse direction is perpendicular to the weld traverse along the width of the plate, and the normal direction is along the thickness of the workpiece, **Figure A1-2**.

1.2.2 Macrostructure and Microstructure

FSW produces four distinct regions: the base metal (BM), heat-affected zone (HAZ), thermo-mechanically affected zone (TMAZ), and stir zone (SZ), **Figure A1-3**. The base metal, or parent metal, is the material that is unaffected by the welding process and thus unaltered in terms of physical properties, composition, and microstructure. The HAZ is the region in which physical properties and/or microstructure have been altered due to the weld process thermal cycle. The TMAZ, located between the HAZ and SZ, is a region unique to FSW processes in which material undergoes significant plastic deformation and heat. The TMAZ is notable for highly deformed, elongated grain structure. The stir zone, also known as the 'weld nugget' or 'dynamically recrystallized region', lies at the center of the weld (i.e. where the pin travels during welding) and experiences high degrees of shear and heat resulting in fine, equiaxed grains. The stir zone shape tends to follow either an asymmetric drop-like structure (as in **Figure A1-3**) or a symmetric, circular 'onion ring' structure.

1.2.3 Processing Parameters

The integrity and shape of the microstructure regions depends greatly on the processing parameters used. Aside from weld plate considerations such as alloy, size, preparation, and constraint are tool and process specific factors such as traverse speed, tool rotation, tool geometry/design, tool pitch relative to the workpiece, and applied force. For new applications or changes in equipment or alloys, a processing window can be developed via adjustment of these factors, with traverse and tool rotation typically proving most effectual. The processing window highlights issues within various processing parameter ranges in addition to defect-free parameter combinations. Suffice it to say careful selection of processing parameters for FSW produces more stable and repeatable weld joint properties when compared to its fusion-based counterparts.

1.2.4 Dissimilar Material Joining

Dissimilar material joining refers to the joining of two or more materials which are of a different (or more appropriately distinct) composition. This nomenclature has been used to specify large differences in composition and properties such as in Al-steel and Al-Ti as well as less severe differences such as aluminum 6061 and aluminum 2024. As atomic bonding is the primary mechanism of bonding and fusion is not involved, FSW is an excellent candidate for welding of dissimilar metals. However, due to the asymmetrical nature of the process and the different properties of the materials involved careful processing parameter control is needed. The tool rotation and travel speeds have a significant effect on the weld with increasing rotation speed and decreased travel speed promoting mixing and interface disruption.[15], [21] In addition to the tool parameter choices, the choice of the advancing and retreating sides and tool offset from the centerline should be considered. In general, the material with the higher hardness and strength will be placed on the retreating side as the superior mechanical properties allow for easier entry and mixing into the softer, lower strength material, resulting in a stronger weld. [22]–[24]

There are two general material flow conditions to considered in dissimilar FSW. A “sharp interface” which presents macrostructurally as a zig zag pattern/shape and a “vortex-like flow” which produces a banded lamellar microstructure containing regions of the other

material. One theory proposes that the “sharp interface” is expected to produce decreased weld strength and be the product of insufficient heat input and thereby poor material intermixing in many material combinations. However, this is a general observation and has been countered in systems such as Al-Mg which possess similar melting and plasticization temperatures. Similarly, the “vortex-like flow” pattern is thought to signify improved intermixing and weld properties and is thus generally preferred if similar material flow stress and weld temperature are expected. [24]

1.3 Self-Reacting Friction Stir Welding

Self-reacting friction stir welding (SRFSW), also known as bobbin tool friction stir welding (BTFSW) or self-support friction stir welding (SSFSW), is a variant of conventional FSW (CFSW) which incorporates the use of a tool composed of two shoulders connected by a thru-thickness pin, **Figure A1-4**. The addition of a secondary shoulder at the root of the weld provides a backing force which eliminates the need for a separate backing plate.

In addition to joining thick and curved workpieces, this variation offers other advantages compared to CFSW including increased efficiency, improved heat distribution and microstructure, and full penetration of thick plates which eliminates the need for multi-pass welds. However, this comes with increases in equipment and tool costs, limiting its adoption. [25], [26] Among industries adopting SRFSW are the aerospace industry where it sees use by Boeing, NASA, and Mitsubishi in circumferential welds for rocket tanks and the high-speed rail industry where it is used for carriage construction. [26]

SRFSW shares the same weld regions as CFSW though with some differences. The stir zone of SRFSW takes on an ‘hourglass-shape’ with the TMAZ following a similar distribution. The TMAZ tends to cover a greater area on the retreating side compared to the advancing side leading to a hazy or diffuse appearance on macrographs. This is suspected to be due to a combination of the material flow conditions and greater temperatures associated with the retreating side. [26]

The process is simple in principle, however, in practice there are numerous factors to control which contribute to weld performance and properties. In addition to the weld plate dimensions and properties, these include traverse and rotation speed, shoulder pinching gap, tilt angle, pin offset, shoulder and pin design, and dwell time among several others, **Figure A1-5**. Of these factors, traverse speed, rotation speed, and shoulder pinching gap are considered the primary independent process parameters for SRFSW. [25]

1.4 Residual Stress

1.4.1 Definition and Theory

Residual stresses are self-equilibrating stresses present in a material in the absence of an external force. As a result, these stresses are balanced in terms of force and moment over the part volume (i.e. $\sum F = 0 \; and \; \sum M = 0$, where F is force and M is moment). These stresses result from several sources inherent in material processing, post-processing, and service conditions which induce "misfits". These misfits originate from differences between local and global thermal gradient (or cooling rates), chemical and phase changes, and plastic flow/deformation as well as interaction of parts within an assembly. [28, p. 2], [29]–[31]

Classification of residual stresses consists of two categories (macrostresses and microstresses) and three types (I, II, and III) where the macro- and micro- designations describe the scale of residual stress variation while the types more precisely describe regional variation [28], [29], [32]:

> **Type I:** Macrostresses which differ on the scale of the part (i.e. greater than the material grain size; often in the multi-millimeter range). These stresses are continuous from grain-grain and phase-phase and equilibrate over the scale of the component (**Figure A1-6a**). Type I stresses are observed for processes such as welding, heat treatments, machining, and shot peening.
>
> **Type II:** Microstresses related to intergranular variation and equilibrate over the material grain size (~ a few microns). Type II stresses arise from grain-grain or

phase-phase misfits in polycrystalline, composite, or multi-phase materials and as such are discontinuous over this range (**Figure A1-6b**). Such stresses are prevalent in polycrystalline materials and increasingly likely in materials with highly anisotropic elastic and thermal properties.

Type III: Microstresses which vary and equilibrate on the sub-grain length scale (i.e. intragranular) and are discontinuous, **Figure A1-6c**. Type III stresses are caused by crystal defects, dislocations, vacancies, or interstitials.

Figure A1-6 relates the length scale variation of Type I, II, and III residual stresses where l_0^I, l_0^{II}, and l_0^{III} are the length scale variation of Type I, II, and III stresses respectively; σ^I is the Type I residual stress; σ_R^{II} and σ_M^{II} are Type II compressive stress in the reinforcement and tensile stress in the matrix; σ_M^{III} is Type III tensile residual stress in the matrix. [32]

Type I/II/III stresses contribute to the overall residual stress state; however, the focus of this work is Type I residual stresses as these are of primary importance in weld evaluation, modeling, and process parameter improvement.

Residual Stresses in Welding

The welding process confers significant differences in local heating which can produce distinct microstructural zones, phase transformations, and in the case of solid-state joining processes (such as FSW and SRFSW) plastic deformations all of which produce Type I residual stress. The introduction of residual stresses greatly influences the performance of welds (typically to their detriment), especially for properties such as fatigue life, fracture toughness, corrosion resistance, and failure mode. [14], [29] Further, the weld residual stress level can be substantial and approximate the material or weld metal yield strength leading to warping, decreased service life, and premature/unexpected failure upon further stress application. [14] As such, there has been a considerable push towards understanding, quantifying, and predicting residual stresses in welds to improve processing parameters and mitigate the effects of residual stress.

Residual stress evolution in fusion welding under constraint conditions is simplified via a concept known as the three-bar problem as explained by Kou. [33] Consider two rigid blocks connected by three metal bars of equal size (**Figure A1-7**) at constant ambient temperature. The middle bar is then heated, typically resulting in expansion. The two unheated metal bars restrict the expansion resulting in a compressive stress. Constrained the compressive stress increases until reaching the material's yield strength, which is the limit of the material's internal and residual stress. Subsequently the middle bar is cooled back to ambient temperature. Conversely as the bar cools, its thermal contraction is also constrained causing its compressive stresses to decrease until they become tensile and the yield strength is achieved. In the final state the system consists of a central bar with tensile stress equal to the yield strength and two side bars with compressive stress which is half of the yield strength. [33] In this analogy, the side bars are the unaffected and restrained base metal while the center bar represents the weld metal.

This concept is further developed and illustrated in **Figure A1-8** which represents the temperature and residual stress evolution during fusion welding. The A-A line is the unwelded and unaffected region whose temperature change and stress are zero. B-B represents the behavior at the welding arc where the initial heating occurs. Here the thermal gradient is steepest - having a sharp peak at the weld center which quickly recedes and approaches zero at the far reaches of the base metal. The residual stresses along B-B are zero in the center as the material beneath the arc is molten and does not support loading conditions. To either side of the middle, slight compressive stresses are observed due to the constraint of the weld pool thermal expansion by the rigid base metal. The increased temperature results in significantly reduced yield strength thereby limiting the compressive stresses to that of the surrounding material. Finally, at the ends of the section tensile stresses are noted which balance the compressive stresses.

Section C-C which represents a post-weld region which continues to cool. It shows the gradual decrease of the thermal gradient as heat diffuses to the section edges. Tensile residual stresses peak in the weld center due to material contraction with adjacent

compressive regions increasing in magnitude and distance. The far ends of C-C now possess slight tensile residual stresses which are close to zero.

Finally, section D-D represents the cooled and completed weld. Here the thermal gradient is zero as the ambient temperature has been achieved across the section and the residual stresses have further developed. The central tensile residual stress has significantly increased in magnitude and covers a greater distance while the compressive regions have similarly evolved and extended to the section edges. [33], [34]

The development of residual stresses in solid-state joining processes such as FSW and SRFSW is similar with the exception of the B-B region as the material at and adjacent to the tool is softened instead of melted.

1.4.2 Residual Stress Characterization Techniques

The study of residual stress has greatly improved over the past several decades due to advances in instrumentation and an increasing number of characterization techniques. Greater accessibility in residual stress determination has resulted in a boon in literature reports for the topic and increased interest, **Figure A1-9**.

Residual stress measurement is a bit of misnomer. In fact, all residual stress determination methods rely on measurement and/or calculation of residual strain (also known as eigenstrain) from which residual stress is then calculated using known material parameters. Characterization methods of residual stress are divided into two broad groups: destructive (stress-relaxation) and non-destructive techniques.

Destructive techniques are mechanical methods which rely on destructive or semi-destructive removal of sample material to infer residual stress. The local stress relaxation from this action is measured via strain gauges or a combined profilometry-modeling approach to determine the residual strain and calculate residual stress. Examples of destructive techniques include hole drilling, nanoindentation, layer removal, sectioning, contour, and ring-core methods.

Non-destructive techniques measure changes in the sample physical properties often without compromising the material, meaning that the service life of the sample is potentially unaffected. Examples include diffraction (neutron, synchrotron, and X-ray), ultrasonic, magnetic, and Raman methods. [29], [35], [36]

A comparison of these techniques is presented in **Table A1-3** and **Table A1-4**.

For the purposes of this work, Type I residual stress evaluation techniques and neutron diffraction residual stress is given particular attention. Background on other techniques is omitted. Should alternate techniques be of interest, the author advises consulting the references in this section for further reading.

1.4.3 Neutron Diffraction Residual Stress

Neutron diffraction is a non-destructive diffraction-based approach to residual stress determination. It is a relatively recent technique with first experimental use for measurement of residual strain being conducted at the beginning of the 1980s. [32] Since that time neutron diffraction has become increasingly important to the study of residual stress and is considered a "gold standard" for weld evaluation.

Principle - Determination of d-spacing, strain, and residual stress
As a material undergoes tension or compression, the interplanar spacing (or *d*-spacing) changes, increasing when in tension and decreasing under compression while the scattering angle varies in the opposite manner, **Figure A1-10**.

Neutron diffraction residual stress determination relies upon the principle of scattering as defined by Bragg's Law, equation 1-1, which correlates wavelength (λ), interplanar spacing aka *d*-spacing (*d*), and scattering angle (2θ).

$$\lambda = 2dsin\theta \tag{1-1}$$

This allows for the calculation of a change in *d*-spacing from change in scattering angle using a known wavelength, equation 1-2.

$$d = \frac{\lambda}{2\ sin\theta} \tag{1-2}$$

A stress-free reference *d*-spacing, known as d_0, can then be used to define the measured residual strain (ε) by relating the d-spacing difference between the measured point (d) and its stress-free reference (d_0) divided by the stress-free reference *d*-spacing (d_0) as per equation 1-3.

$$\varepsilon = \frac{d-d_0}{d_0} \tag{1-3}$$

Strain can be measured in each direction (nine in total) to provide a comprehensive understanding of the material strain state for the triaxial state. Strain is a symmetric rank 2 tensor consisting of six shear strain components and 3 normal strain components. Rotation of this tensor to a principal strain direction (i.e. one in which all shear strains are zero) yields a simplified relation which aids further calculation, equation 1-4, where ε and γ are the normal and shear strain components, respectively. [3] The strain assumption in welds is that the weld plate's orthogonal directions – normal, transverse, and longitudinal – serve as the principal strain directions. [38]

$$\varepsilon_{ij} = \begin{bmatrix} \varepsilon_{11} & \gamma_{12} & \gamma_{13} \\ \gamma_{21} & \varepsilon_{22} & \gamma_{23} \\ \gamma_{23} & \gamma_{32} & \varepsilon_{33} \end{bmatrix} = \begin{bmatrix} \varepsilon_{11} & 0 & 0 \\ 0 & \varepsilon_{22} & 0 \\ 0 & 0 & \varepsilon_{33} \end{bmatrix} \tag{1-4}$$

Using the computed residual strain in each principal direction as in equation 1-3, the calculation of residual stress becomes possible. [32], [38] Hooke's Law, equation 1-5, is applied along with standard environment and isotropic conditions assumptions to provide the following relation, equation 1-6:

$$\sigma = E\varepsilon \tag{1-5}$$

$$\sigma_i = \frac{E}{1+\nu}\left[\varepsilon_{ii} + \left(\frac{\nu}{1-2\nu}\right)\left(\varepsilon_{11} + \varepsilon_{22} + \varepsilon_{33}\right)\right] \tag{1-6}$$

where σ_i is the component of residual stress, E is the elastic (Young's) modulus, ν is Poisson's ratio, and ε_{ii} is the component of residual strain.

Instruments and Sources

Neutron diffraction instruments employ two basic designs based upon the neutron source: reactor and spallation.

A reactor source instrument generates a continuous beam of polychromatic neutrons via nuclear fission. The neutrons are guided away from the reactor and toward a sample by neutron guide tubes. These neutrons are then converted to a single wavelength by a monochromator and the measured 2θ range is varied. Neutron diffraction experiments in reactor source instruments, therefore, cover a small defined range of 2θ (~18° at HIDRA) and one or two diffraction peaks. This range is also limited as the scattering angle is generally kept at 90° to ensure a cubic gauge volume. *Gauge volume is discussed in the following section.*

Spallation source instruments generate polychromatic neutrons by the collision of high-energy proton pulses on a heavy metal target (W, Ta, or liquid Hg) – a process known as spallation. The difference is that the moment of neutron generation is known as is detector distance which allows for determination of time-of-flight (TOF) for each neutron. This setup provides a polychromatic wavelength and a large but fixed 2θ range enabling the measurement of multiple diffraction peaks and/or directions simultaneously.

An illustration of the reactor and spallation designs in relation to neutron diffraction residual stress measurement is given in **Figure A1-11**.

Gauge Volume

Neutron diffraction is unique in that it offers complete sub-surface residual stress evaluation in three dimensions. This allows the full mapping of the residual stress condition which is helpful for modeling and process parameter development. This is accomplished using a concept known as a gauge volume. The gauge volume is a measurement volume defined by the intersection of the incident and diffracted beam where the scattering vector Q (i.e. direction of measurement) is along the bisector. Gauge volume size and shape can be adjusted with the aid of slits at the incident and diffracted beam positions to those required for the measurement, **Figure A1-12**.

Orienting the sample in relation to the incident and diffracted beam path allows for the measurement of the principal strain directions (transverse, normal, and longitudinal), where the scattering vector, Q, is aligned along measured direction denoted by the arrow in **Figure A1-13**.

The incident and diffracted beam path can be described in terms of beam geometry in relation to a sample, represented in **Figure A1-14** for reflection and transmission geometries. Reflection geometry is typically used for the normal direction measurement while transmission geometry is typically used for the transverse and longitudinal direction measurements.

Beam geometry can have importance consequences for neutron diffraction experiments particularly when a portion of the gauge volume lies outside the sample - a condition known as a partially buried gauge volume. In an experiment quantifying the effects of partially buried gauge volumes on the Ni (311) reflection of a stress-free nickel specimen, Wang et al. noted that while the transmission geometry displayed little to no peak shift "until the specimen was almost completely out of the sampling volume" the reflection geometry was affected by even a slight partial burial of the gauge volume, **Figure A1-15**. [40] This peak shift leads to a skewed *d*-spacing and correspondingly incorrect strain/stress, leading to erroneous results.

Characteristic peak

Another consideration is the selection of a characteristic peak for evaluation. A characteristic peak is defined as one which is not readily affected by intergranular strain and shows strain linearity under at least uniaxial loading conditions. This is essential as certain planes can be significantly affected by texture (as well as loading and plastic deformation) leading to inaccurate strain and stress determinations. For aluminum alloys, the (311), (422), and (220) planes are recommended for residual stress experiments while the (200) plane is strong affected by intergranular strains and avoided. A summary of the Versailles Project on Advanced Materials and Standards (VAMAS) standard for characteristic peak selection is provided in **Table A1-5**. [39]

Considerations for FSW evaluation

In addition to the above noted instrumental factors, successful neutron diffraction of FSW/SRFSW require several important sample-specific considerations to be made for accurate residual stress determination.

Grain Size and Texture

In terms of neutron diffraction, large grain size (> 50 μm) and grain asymmetry can lead to inaccuracy in peak positions and thereby residual strain and stress. [30] Grain size attributable error occurs via two methods – insufficient counting statistics and asymmetric diffraction with the risk/likelihood of these errors being directly proportional to increasing grain size. Diffraction conditions are limited by the incident beam's angular divergence which results in a small angular range over which grains can diffract. Further, in a reactor-based experimental setup, only grains oriented in the chosen plane(s) will diffract when interacting with the gauge volume. In the first case, large grain size reduces the number of diffracting grains within the gauge volume which increases uncertainty in peak position for a given location. Additionally, even when large grains are oriented to diffract they may do so in an asymmetric manner (i.e. large changes in peak position with small orientation change).

Ensuring grain size related error is avoided can be accomplished in several ways. In preparation for the experiment, intensity (counts/s) should be measured at several locations and determined to be well above background (> 400 counts above) with well-defined peaks for all gauge volumes. Second, microstructural studies and grain size measurements should assist in the appropriate selection of gauge volume dimensions. For measurements of a welded structure in which texture and grain size invariably change, the gauge volume must contain enough diffracting grains for statistical significance. Typically, at least 10,000 grains are required to meet this condition so a calculation should be used to determine the expected number of grains contained within the smallest gauge volume to be used.

Additional verification can be accomplished at the instrument by performing a rocking curve measurement on the sample. In a rocking curve measurement, the detector is placed at the peak diffraction angle while the sample stage moves over θ and/or ω over a small

angular range (± 5°). Variation in the measured intensity below the square root of intensity is considered sufficient for the measurement condition. In this case either increasing the gauge volume size and/or including rotational/translational sample oscillations during measurement should mitigate the effect of large grain size.

Large grain size and significant textural evolution which can also produce an "edge effect" within the specimen. Large grain sizes result in fewer grains which meet the diffraction conditions (i.e. poor counting statistics) and increased possibility of erroneous peak-shift leading to an erroneously high compressive or tensile strain at that location. [30] One method of evaluating the presence of potential edge effects within a specimen is to interrogate normalized intensity plots (I/I_0) for each direction for large deviations from the baseline.

Stress-free reference – d_0

The stress-free reference allows the quantification of residual stress from a sample. Notably, this reference is not necessary for all weld measurements but is critical for alloys which undergo chemical changes such as precipitation-hardened materials. During the welding process many precipitation hardened alloys such as aluminum 2219 and 2195 undergo dissolution due to the elevated temperature. For the case of 2219 as these precipitates solutionize, increasing amounts of copper are incorporated into the solid solution ($Al_{1-x}Cu_x$) thus linearly decreasing the lattice parameter in accordance with Vegard's Law. [32], [42] This leads to a considerable decrease in *d*-spacing in the weld zones compared to the base metal and a potentially large apparent tensile strain, **Figure A1-16**. Vegard's law also applies to the opposite scenario, as the precipitates coarsen/grow, the lattice parameter and thus the *d*-spacing increase.

Continued post-weld natural ageing can also impact the measurement of residual stress in a similar manner though not as significantly. Aval noted in study of 8 mm thick plate FSW AA6082-T6 and AA7075-T6 that X-ray residual stress measurements at 7 days and 365 days post weld resulted in a residual stress reduction of between 15-20 MPa for the stir zone and TMAZ. [44]

If the selected location of the coupon or comb, for the d_0 measurement, is not the same as other measurement positions, as is the case for most neutron experiments, the effect of stress relaxation should be considered. Avoiding stress relaxation is accomplished by selecting a region which is offset approximately eight times the weld tool diameter so 90% of residual stresses are maintained. [45], [46] It has been suggested that some experiments fail to meet this guidance and residual stress values are under-reported as a result. [14] Finally, the selected location should be at a position representative of the desired weld location (i.e. having achieved steady state conditions) – typically far from the weld onset and terminus.

1.4.5 FSW and SRFSW Residual Stress Measurements

A review of residual stress measurements of similar and dissimilar aluminum welds studies using both FSW and SRFSW was conducted to obtain relevant background information and inform expectations. Comparison with similar alloys and tempers to those in this proposal were also considered. General observations are stated and a few specific examples of residual stress measurement studies are presented.

Residual Stress Distribution

Longitudinal residual stresses are typically considerably larger than the transverse or normal directions and follow a "M-" or "W" shaped distribution. Peak longitudinal residual stresses are tensile in nature and extend to slightly outside the tool shoulder region (near or within the HAZ) before decreasing significantly toward the base metal of either side. Compressive longitudinal residual stresses are observed toward the base metal and workpiece edges. Residual stress also varies as a function of plate thickness and traverse. The highest stresses are typically located near the surface close to the edge of the tool shoulder and increase along the traverse toward the weld terminus. [14]

In general, fusion welding processes tend to produce higher residual stresses than solid-state processes such as friction stir welding though this can vary considerably. [14], [17] Direct comparison of residual stress magnitude in aluminum FSW and SRFSW is convoluted owing to the diverse range of processing parameters, tool design, alloys, and weld plate dimensions, however, general trends can be established. Woo et al. complied

neutron diffraction residual stress studies of various FSW aluminum alloys and noted that the ratio of maximum longitudinal residual stress to yield strength was 20-70%. [38]

Martukanitz et al. conducted a neutron diffraction residual stress experiment on 5 mm thick AA2219-T87 and AA2195-T8 single-pass variable polarity plasma arc (VPPA) welds using 2319 filler alloy to calculate the residual strain and stress in the longitudinal, normal, and transverse directions. [41] The study noted that peak tensile and compressive residual stresses were related to the position of minimum hardness in the HAZ just outside the fusion zone. The normal and transverse directions were tensile until ~16 mm from the fusion zone where they decreased into the compressive region. Maximal tensile residual stresses for the 2219-T87 plate were 50-, 10-, and 90- MPa for the transverse, normal, and longitudinal directions, respectively. The largest compressive residual stresses were ~ -50 MPa for all directions.

Albertini et al. compared TOF neutron and X-ray residual stress measurements on 6.5 mm thickness AA2219-T87 via VPPA. [47] X-ray residual stress determination showed that stresses incurred by mechanical polishing were removed with electropolishing. Neutron diffraction provided longitudinal and transverse strains, noting highest compressive stresses in the HAZ (-150 MPa) and highest tensile stresses in the fusion zone (80 MPa).

In work on a similar 2219-T87 SRFSW plate of 15.875 mm thickness and proprietary tool and processing parameters, Anderson used x-ray diffraction to determine the surface residual stress. Measurements were taken on the weld crown to a penetration depth of 94.16 μm (working volume 0.296 μm^3) along the transverse direction to $\pm$50 mm from the weld center and $\pm$152 mm from the origin along the longitudinal direction. Longitudinal residual stresses values were higher on the advancing side and remained consistent along the weld traverse while those on the retreating side were lower and increased significantly (5.9 to 109.3 MPa) along the weld. The maximal longitudinal residual stress was 117 MPa and occurred in the stir zone. The minimal longitudinal residual stress achieved was -94 MPa at the retreating-side TMAZ. Transverse residual stresses were generally compressive with a minimum of -75.3 MPa.

Xu et al. evaluated longitudinal residual stress in 12 mm thick FSW AA2219-T62 using the hole-drilling method. [48] Due to limitations in the measurement technique selected, only the crown and root surfaces were evaluated. A variety of processing conditions were evaluated, concluding that although increased traverse and rotation speed result in increased longitudinal residual stress, rotation speed had a greater overall effect. Maximum longitudinal residual stress for a sound weld were 171 MPa on the crown surface. An asymmetric "M" shaped distribution was observed with higher residual stresses toward the advancing side for the crown surface while an inverted "V" profile was observed for the root surface. The peak tensile longitudinal residual stress value for the root surface was 99 MPa for a sound weld. Maximum residual stresses increased to 243 MPa (77% yield strength) in the presence of a defect.

1.5 Precipitate Evolution

1.5.1 Precipitate Strengthening

History

In 1906, Alfred Wilm discovered the phenomenon of age- or precipitation- hardening while working with aluminum-copper alloys. He related that after quenching from a temperature slightly below the melting point the hardness of an aluminum alloy (4% Cu and 0.5% Mg) increased over time at while room temperature. [49] Since that time, the mechanistic understanding of the phenomenon has greatly developed and the Al-Cu system he described is a common example in textbooks owing to its general simplicity.

Theory

Precipitation strengthening relies on a specific sequence of heat treatments. A solution heat treatment near the solidus/liquidus temperature allows for the complete dissolution of solute. The alloy is then quenched to room temperature (or a temperature in the two-phase region) to retain a supersaturated solid solution (SSSS). Finally, the ageing heat treatment is conducted at either room temperature (natural ageing) or at an elevated temperature (artificial ageing) resulting in precipitate formation/growth, **Figure A1-17**. The desired ageing/precipitation state is determined by temperature and time constraints and is further described in the temper designations. [2], [10], [50]

This set of heat treatments is visualized on a hypothetical phase diagram (**Figure A1-18**) where T_0 is the solution heat treatment temperature, T_1 is the temperature upon quenching (room temperature), and T_2 is the artificial ageing temperature. Here C_0 is the alloy composition when undergoing the heat treatment and C_α and C_β are the compositions of the α and β phases, respectively. Quenching from T_0 to T_1 does not allow for the formation of the β phase and produces a nonequilibrium condition in which the α phase is supersaturated with B atoms. Increasing the temperature to T_2 allows for diffusion to take place and formation of fine β precipitates of C_β composition to form. [51]

This is the same process followed for the Al-Cu system where the binary phase diagram is provided with and without relation to metastable precipitate formation is given by **Figure A1-19**.

Precipitate Strengthening Mechanisms

Precipitates strengthening occurs in alloys due to the hinderance of dislocation motion and interaction. When a dislocation encounters a precipitate the resulting interaction can manifest as either particle shearing or Orowan looping, **Figure A1-20**. [3], [4] Particle shearing typically occurs when dislocations meet fine, dispersed precipitates while Orowan looping is the result of relatively large, coarse precipitates.

For highest strength, particle shearing and thus a high volume of small precipitates is preferred. The precipitation strengthening effect decreases as precipitates coarsen and overage as visualized in **Figure A1-21**.

1.5.2 Precipitates of 2219 and 2195

AA2219

The precipitates of 2219 are θ”, θ’, θ (~Al_2Cu) and follow the precipitation sequence:

$$SSSS \rightarrow GP\ zones \rightarrow \theta'' \rightarrow \theta' \rightarrow \theta$$

Guinier-Preston (GP) zones form first in the precipitation sequence from a SSSS and are the consequence of local atom clustering during diffusion. Due to lower interfacial energy and full coherency with the matrix GP I zones are the first to form in the precipitation sequence. These are metastable single layers of Cu atoms aligned along the

{100} planes, possess a plate-like appearance, and span several atoms in thickness and approximately 25 atoms in diameter. [4]

θ" (sometimes referred to as GP II) are coherent with the matrix and measure approximately 10 atoms in thickness and 75 atoms in diameter. [4] There is some debate regarding the stoichiometry and structure of the GP II zone. Descriptions are large clusters of Cu atoms aligned along the {100} planes with stoichiometry of AlCu [3], [4] and as two layers of Cu atoms aligned along the {002} plane separated by three layers of Al atoms, yielding a stoichiometry of Al_3Cu. [54] These differing determinations are incidental to this work and as such assessment of their validity lies beyond its scope.

θ' are metastable, semi-coherent, platelet-shaped precipitates with a body centered tetragonal crystal structure (*I4/mmm*) and stoichiometry of Al_2Cu. [55] Sizes for this phase vary somewhat but typically range from 20-30 nm in length and 1.5-2.5 nm thickness to 100-340 nm in length and 15-20 nm thickness. [56], [57] These serve as the primary strengthening agent of the alloy.

θ is the equilibrium phase and marks the completion of the precipitation sequence. θ precipitates These particles are incoherent with the matrix, have Al_2Cu stoichiometry, and a tetragonal C16 structure (*I4/mcm*). These precipitates can take on a globular or spherical shape and can be quite large with dimensions generally less than 25 μm. [58]

Additionally, the formation of brittle intermetallics, Al_7Cu_2Fe and Mg_2Si, which decrease strength and toughness are possible due to the presence of impurity atoms Fe and Si, respectively. The intermetallic Al_7Cu_2Fe also affects precipitation response due to the decrease in copper availability.

AA2195

There are a wide variety of possible precipitates in 2195: θ'-type (~Al_2Cu – θ", θ', θ), T (AlLiSi), T_1 (Al_2CuLi), T_B (Al_7Cu_4Li), T_2 (Al_6CuLi_3), δ' (Al_3Li), β' (Al_3Zr), $Al_{20}Cu_2Mn_3$ and possibly Ω and S'. As with 2219, the formation of the Al_7Cu_2Fe intermetallic is possible and is responsible for the same effects. [12], [59], [60] Of these possible precipitates/phases T_1, δ', and θ'-type precipitates are those most responsible for strength

improvement and thereby greatest interest to the proposed study. T_1 also contributes to toughness control along with T_2, β', and $Al_{20}Cu_2Mn_3$.

A defined precipitation sequence for 2195 is not available owing to the multitude of potential phases in the ternary system and instead depends upon the actual composition and thermomechanical processing conditions. [61] There is direct phase competition between the two primary strengthening precipitates, θ' (Al_2Cu) and T_1 (Al_2CuLi), for Cu solute atoms. Preferential formation of T_1 over of θ' was linked to the presence of Mg (0.35 wt%) and dislocations. [62]–[64]

1.6 Precipitate Characterization

Precipitate characterization is a complex task owing to the broad range of desirable precipitate information. Complete precipitate characterization requires determination of distribution (size, size distribution, volume fraction, and number density), chemistry (composition), morphology (shape and orientation), and structure (phase identity and stability). Due to the nature of the problem, several techniques are required to obtain an in-depth and quantitative understanding of the precipitate state. These techniques can be grouped into local and global techniques with local techniques providing specific information related to a small sample size and global techniques relating averaged information of a larger sample size. [65]

Here several methods of precipitate characterization are briefly described. Particular attention is given to transmission electron microscopy (TEM), small-angle scattering (SAS), and atom probe tomography (APT) with an additional section devoted to the principles of SAS.

1.6.1 Local Techniques

Local techniques are important for the determination of morphological, structural, and local compositional information and can be further subdivided into microscopy and other methods.

Microscopy

Microscopy methods are the most utilized method for determining precipitate evolution in materials. These methods are advantageous as they offer direct, visual confirmation of

the precipitate state and ready measurement of size, shape and when combined with other techniques orientation and composition.

Optical microscopy (OM) is primarily used for grain size measurements, weld defect characterization, and qualitative understanding of texture. OM sees limited use in identification of precipitate size and shape as most precipitates studies are nano-scale and below the limits of visual detection. However, characterization of larger macroprecipitates is possible and can prove useful for understanding the overall precipitation state. Similarly, use of scanning electron microscopy (SEM) is limited for nanoprecipitate characterization. SEM when equipped with EDS is able to identify precipitate composition and offer a rough visual approximation of coarse precipitate volume fraction.

Oertelet et al. in work on thermal cycling of 5.8 mm thick AA2195-T8 FSW employed SEM micrographs and a National Institute of Health (NIH) image analysis program, a precursor of *ImageJ*, to analyze coarse second-phase precipitates in terms of volume fraction. [66] Comparison of precipitate volume fraction via this method for the as-welded condition and a thermal cycle (430 °C followed by continuous cooling) showed 1.8606 $\pm$.731% and 5.349 $\pm$1.209%, respectively.

Transmission electron microscopy (TEM) is the preferred microscopic method for precipitate characterization and is utilized in a majority of studies. In TEM, electrons are accelerated through a vacuum and focused by electromagnetic lenses resulting in a thin beam. This beam is directed at and passes through the sample of interest and impacts a detector, producing an image.

Nano-scale precipitates are readily identifiable, and shape and size measurements can be taken reliably. The resolution of TEM is excellent and can distinguish features as small as ~0.2 nm for electron energy loss events and 1 nm from x-ray emission. [67] Precipitate volume fraction and number density can also be interrogated with TEM. The combination of electron-energy loss spectroscopy (EELS) and convergent beam electron diffraction (CBED) allow for conversion of the “mean-free path length” to nanometers while precipitate number density can be calculated by dividing the precipitate count by the

analyzed volume (area and foil thickness). Structurally, precipitates can be identified via selected-area electron diffraction (SAED or SAD) which can also provide qualitative information regarding specific precipitate volume fraction.

Unfortunately, TEM comes with significant downsides. The instrumentation and maintenance cost are high with instruments costing approximately $5-10 per electron volt (eV) and beam energies between 100-400 keV. Typical sample volume is low, estimated at 10^3 mm^3, and highly localized making it difficult to make definitive statements regarding the bulk material. [68] Further sample preparation can be difficult and costly with prepared samples being small and fragile.

Sample preparation is conducted by thinning a sample to 100-200 μm, sectioning a 3 mm disk from the bulk sample, and finally thinning the central region to less than 100 nm. The final thinning step is typically conducted via focused ion beam (FIB) or twin-jet electropolishing in the case of metals. [68] In the case of aluminum alloys, twin-jet electropolishing is preferred to avoid preferential inclusion of gallium at interfaces which occurs with Ga-FIB.

Atom Probe Tomography (APT)

Atom probe tomography offers a unique combination of atomic scale 3D imaging and composition analysis which provides detailed information regarding precipitates. In APT, the sample material is milled into a needle-like specimen with a radius of curvature of ~50 nm. The sample is then placed in ultrahigh vacuum, cooled to 80 K, and biased with high voltage (1-15 kV) which produces a strong electric field. The sample is ionized atom by atom using high voltage or laser pulses and the atoms are accelerated and collected on an ion detector. Time of flight, 3D position, and mass spectrometry (ion mass-to-charge ratio) is then used to produce a three-dimensional reconstruction of the sample. [67], [69]

APT possesses excellent spatial resolution (0.3 nm or better in all directions) and compositional analysis for precipitates and their interfaces. However, it is limited to a relatively small sample volume (~10^6 nm^3) and precipitates in the range of 100 nm or less. [67] APT is also able to measure the solute concentration of the matrix which allows

for positive identification of precipitate related local composition changes and aids in volume fraction determination with complementary SAS studies.

1.6.2 Global Techniques

Differential Scanning Calorimetry (DSC)

Differential scanning calorimetry is a technique that measures the heat flow of a sample by comparing its thermal response to that of a reference material over a given temperature range. As such, DSC is capable of determining the onset and completion phase changes such as the formation or dissolution or precipitates as well as the ageing state of a material. It is also possible to obtain precipitate volume fraction from DSC results as observed by Esmaeili et al. study of precipitation in AA6111 and Wang and Shenoy's study of AA1460 and AA2195. [70], [71]

Scattering Methods

Scattering methods refer to techniques which rely on the scattering of incident particles or radiation (light, X-ray, neutrons, etc.) to obtain information related to particles or defects.

In X-ray diffraction (XRD), the scattering of X-rays from electron sites in the crystal lattice (as in Bragg's Law) relates information on the lattice spacing and crystal structure based upon the appearance of reflections. This information can be used for precipitate identification and quantification with Rietveld refinement.

Small angle scattering (SAS)

Small angle scattering techniques offer several advantages to precipitate characterization. Scattering provides an average of the bulk which can provide or semi-quantitative information related to precipitate size, number, distribution, shape, morphology, local interactions, and polydispersity. Further, composition measurement is possible for wide-angle scattering measurements.

Additional advantages of SAS techniques are an increase in sample volume compared to other measurement techniques. Panagos *et. al* notes, "In SAXS, the sampling volume is typically more than 10^9 times that of TEM, assuming a foil thickness of 100 nm and a field of view of 500 × 500 nm for TEM and an X-ray beam diameter of 300 μm with a

sample thickness of 250 μm for SAXS." [72] The technique is able to evaluate a large size scale (1 Å to ~6 μm) when factoring in ultra-small and wide-angle measurements. Further, measurements are typically non-destructive (with the exceptions of radiation sensitive materials and high energy experiments) and in-situ and time resolved studies are possible.

SAS also has significant disadvantages. Concern for convolution of scattering data from multiple scatterers/geometries such as grain texture variation, precipitate anisotropy, and heterogeneous microstructure is significant. Unsurprisingly, data obtained from SAS can be difficult to process and generally only relative relations (qualitative and semi-quantitative results) are possible. Therefore, it is necessary to pursue other techniques such as TEM and APT for complementary and confirmatory measurements.

A comparison of techniques highlighting effective size ranges and structures is provided in **Figure A1-22**.

1.7 Small angle scattering (SAS)

1.7.1 Principles

The operating principle of SAS is relatively simple and similar in some regards to diffraction. As illustrated in **Figure A1-23**, a source generates X-rays or neutrons which travel through a monochromator that provides the desired wavelength. The beam is defined via collimation and area of coverage is determined by the aperture. This beam travels through the sample and is scattered by particles or objects within after which it is detected and converted to a signal. The difference between the vectors for the uninterrupted, transmitted beam ($\vec{k}_i$) and scattered beam ($\vec{k}_s$) define the scattering vector ($\vec{q}$).

The $\vec{q}$ range probed can be altered by varying the distance between the sample and detector. Moving the detector close to the sample results in collection of wider scattering angles and provides information in the high $\vec{q}$ region (atomic scale) – known was wide-angle X-ray scattering (WAXS) or wide-angle neutron scattering (WANS). Conversely,

increasing the detector distance selects for the low $\vec{q}$ region (i.e. larger size) and is known as ultra-small angle scattering (USAXS/USANS depending on X-ray or neutron source).

1.7.2 Mathematical Basis

Conversion of $\vec{q}$ into a real-spacing measurement requires introducing the concept of momentum transfer. Momentum transfer (q) is defined as the magnitude of the difference between the scattered and incident beam, equation 1-7. Momentum transfer is related directly to wavelength and angle and not real, physical space as in equation 1-8.

$$|\vec{q}| = \left|\vec{k}_s - \vec{k}_i\right| = q \tag{1-7}$$

$$q = {}^{4\pi}/_{\lambda}\, sin\theta \tag{1-8}$$

Momentum transfer can be related to a real space orientation by conversion to *d*, feature size, equation 1-9.

$$d = {}^{2\pi}/_{q} \tag{1-9}$$

A simplified synthesis of the information contained in the scattering pattern can be represented by equation 1-10.

$$I(q) = n|F(q)|^2 S(q) \tag{1-10}$$

where the total intensity (I) as a function of momentum transfer (q) is related to the number density of the particles (n), the form factor (i.e. particle size/shape) - F(q), and structure factor, S(q), which can be thought of as the packing or particle interactions/distance.

Scattering intensity from a single particle $I_1(q)$ is related it to the electronic density of the particle (ρ_p) and matrix (ρ_m), particle volume (V_p), and radius of gyration (R_g) defined as the density distribution around the center of mass as in equation 1-11. With this equation inference of particle volume and/or gyration radius is possible.

$$I_1(q) \underset{q\to 0}{\equiv} (\rho_p - \rho_m)^2 V_p^2 e^{\left(-\frac{q^2 R_g^2}{3}\right)} \tag{1-11}$$

Total scattering intensity is the contribution of the individual scatterers and a size dispersion model, f(R), as in equation 1-12.

$$I(q) = \int_0^\infty f(R) I_1(q, R) dR \quad (1\text{-}12)$$

Finally, the invariant Q_v (integrated intensity) can be directly related to the volume fraction (f_v) and electronic density of the particle and matrix via equation 1-13.

$$Q_v = 2\pi^2 \left(\rho_p - \rho_m\right)^2 f_v (1 - f_v) = \int_0^\infty I q^2 dq \quad (1\text{-}13)$$

1.7.3 Data Representation

Data from SAS studies can be represented via either 2D or 1D scattering patterns each providing specific sample information.

2D

SAS experiments can be represented in a 2D fashion which provides useful information regarding overall scattering intensity as well as sample anisotropy or texture. Overall scattering intensity can be qualitatively related to the number of scatterers or volume fraction. In the case of anisotropy, the ratio of the long and short axes provides an estimation of scatterer geometry or scatterer texture, **Figure A1-24**.

Importantly, data obtained from 2D scattering patterns is qualitative and interpretation easily biased.

1D

The resultant 2D pattern can be converted to a one-dimensional pattern allowing extraction of additional information with either an azimuthal average or region average approach. A typical 1D scattering pattern is presented in **Figure A1-25** and illustrates the entire SAS range including USAS and WAS.

The small q region (Figure A1-left) represents the Guinier region. This region typically relays information regarding scattering size and is so named as at small q anything that can reasonably be considered a discrete object follows Guinier's approximation. Just outside the Guinier region the curve shape provides an indication of shape. The Porod region represents the scattered intensity separated from the matrix by a sharp interface

and interrogates the particle (boundary) smoothness. Finally, the wide-angle scattering region provides information related to atomic structure.

In order to extract information from the 1D scattering pattern, it must undergo fitting to determine relevant scattering parameters. This can be accomplished using either a model driven approach for known or approximate scatterer size, shape, dispersity, and matrix composition or a law driven approach which applies fitting of general relations and equations to obtain this information.

1.7.4 Small-angle Scattering in FSW

The application of small-angle scattering techniques to precipitate characterization in welds and in particular FSW is a relatively recent development. This section provides a brief comparison of SANS and SAXS and their respective uses as well as a summary of relevant literature.

SAXS and SANS

In SAXS X-rays strike the sample material and are scattered by electrons. Sources are widely available and can be accessed at the laboratory level as well as synchrotron sources. The large fluxes and fast collection times (on the order of seconds or less) allows for time resolved and in-situ studies. The beam size is also smaller and typically provides better spatial resolution.

Drawbacks to SAXS center on its lower penetration which limits sampling volume, potential for radiation damage, and sample/surface preparation requirements.

SAXS is typically used in age-hardenable aluminum alloys due to its ability to rapidly map the precipitate evolution over large sections with smaller beam size and often better resolution. It does not work well with AA6xxx (Al/Mg/Si) series due to low Z-contrast.

In SANS neutrons bombard the sample material and are scattered by the atom nuclei and magnetic moment. Radiation damage is also minimal for most samples. This makes neutron scattering ideal for the study of magnetic materials and those with significant neutron contrast variation. Radiation sensitive materials also benefit from minimal radiation damage from SANS. Owing to increased penetration for most materials, sample preparation is also significantly easier compared to SAXS.

SANS evaluation does have a few detracting qualities, however. SANS is less accessible as it is available only at large user facilities with a reactor or spallation source. Measurement collection time is relatively slow (minutes) which limits its ability to perform in-situ or time resolved studies and reduces throughput. Finally, beam size is typically larger, limiting resolution.

SANS is most often used for oxide dispersion strengthened steels (ODS), nanostructured ferritic alloys (NFAs), and ferritic steels owing to the magnetic moment associated with these alloys. SANS also sees use for AA6xxx series alloys as it provides sufficient elemental contrast compared to SAXS.

Literature
Small-angle scattering is a powerful technique for the mapping of precipitate properties across welds. SANS was first employed in weld evaluation to study radiation effects on reactor pressure vessel welds around 1985. [76] In application to FSW, Genevois et al. (2005) was among the first demonstrate the use of SAXS in a AA2024 FSW and successfully mapped precipitate evolution across the weld in terms of precipitate thickness and volume fraction. [77] Other SAS studies of FSWs followed. A summary of available literature for SAXS and SANS precipitate characterization is presented in **Table A1-6** and **Table A1-7**, respectively.

1.8 Aluminum 2xxx (SR)FSW Precipitate Review

The following section is devoted to literature review of relevant studies related to precipitate evolution and characterization for AA2219 and AA2195 as well as FSW and SRFSW. A brief summary of information is presented in this introduction with extended summaries of relevant studies to precipitation in AA2219 and AA2195 following.

1.8.1 AA2219

Papazian characterized precipitates in 2219-O, 2219-T31, 2219-T81, 2219-T851, and 2219-T87 using TEM and DSC. [96] Thermograms showed four distinct regions: an "endothermic (dissolution) reaction between 50-200 °C" relating to the dissolution of GP zones, an "exothermic (precipitation) reaction between 200-300 °C" attributed to the precipitation of θ', "multiple endothermic (dissolution) reactions between 300-550 °C"

related to the dissolution of θ’ and θ, and “a superimposed exothermic (precipitation) reaction between 400-475 °C" related to the precipitation of θ. Precipitate sizes were reported as between 85-700 nm diameter and 3.5-17 nm thickness for the platelet-shaped θ’ undergoing ageing for 5 h at 250 °C, θ ranged from 0.1-1.5 μm, and θ” was measured at 2 nm up to 10 nm maximum diameter after 2.2 days of ageing at 250 °C. Papazian also characterized the precipitation and dissolution kinetics of AA2219 via DSC. [97]

FSW

Kang et al. in working with FSW AA2219-T8 employed DSC, XRD, and TEM to analyze precipitates present in the joint. [58] Temperatures achieved in each zone were measured and noted to be 180-380 °C for the HAZ and 380-400 °C in the TMAZ. SZ temperatures were not obtained due to destruction of the embedded thermocouples though temperature was noted to be ~10 °C lower on the retreating side compared to the advancing side. In the HAZ, all θ” and some θ’ precipitates solutionized with the remaining θ’ precipitates coarsened. The TMAZ saw solvation of both θ” and θ’ precipitates while in the SZ all precipitates (θ”, θ’, and θ) redissolved into the matrix.

Based upon TEM and SAD measurement precipitate identity, size, and shape were determined. θ’ phases were disk-shaped with 30-150 nm diameter and less than 5 nm thickness in the base metal and coarsened in the HAZ to 50-230 nm diameter and 10-15 nm thickness with locations closer to the SZ displaying a decrease in size and density. θ phases were rod-shaped and identified in the TMAZ and SZ. Large agglomerations of θ phase were noted ranging in size from 100-1000 μm. DSC data was also conducted and is summarized in **Table A1-8**.

Arora et al. in study of the microstructural evolution of 5 mm thick plate FSW AA2219-T87 used TEM and DSC to evaluate precipitate evolution. [98] It was noted that *θ*” and *θ*’ precipitates ranged in size from 25-200 nm over the weld though did not specify the location or change. TEM images of the SZ noted an absence of disk-shaped precipitates while DSC peaks were used to estimate 40% dissolution of Al_2Cu phases in the SZ. TEM noted that in terms of precipitate presence the TMAZ was similar in appearance to the SZ while the HAZ was similar to the BM.

Chen et al. conducted a study on 5 mm thick plate FSW AA2219-T6 characterizing precipitates via TEM. [57] Plate-shaped θ" and θ' precipitates were observed in the BM and measured 100-340 nm diameter and 15-20 nm in thickness. Precipitate morphology in the SZ was significantly different than the BM and contained primarily θ precipitates with SAD suggesting a high-volume fraction of this phase. A post-weld ageing heat treatment was performed which resulted in a high degree of re-precipitation of plate-shaped precipitates. The TMAZ precipitate morphology was similar to the SZ with SAD indicating the transformation of θ' precipitates to θ. A high volume of θ' platelet-shaped precipitates were present in the HAZ and measured 20-40 nm in thickness showing coarsening compared to the BM but no evidence of dissolution. Peak temperatures were measured using K-type thermocouples and found to achieve the highest temperature (450 °C) in the SZ with temperatures of 200-400 °C in the HAZ and 400-450 °C in the TMAZ.

SRFSW

Li et al. characterized precipitation in 8 mm thick SRFSW of AA2219-T87 with TEM. [99] The BM contained a high density of evenly distributed, plate-shaped θ' precipitates measuring 40-110 nm in length. The HAZ observed larger θ precipitates and greater dissolution of θ' than observed in literature for FSW AA2219-T87 which was attributed to higher achieved temperature in this region. The TMAZ and SZ were similar in appearance with sparse precipitation with few θ precipitates.

1.8.2 AA2195

Khushaim et al. employed APT and TEM to characterize precipitates in AA2195-T8. [100] TEM showed the presence of platelet-shaped $T_1(Al_2CuLi)$, θ'(Al_2Cu), and spherical β'(Al_3Zr) precipitates and their respective orientations but did not provide size measurements. APT confirmed stoichiometry of θ' precipitates but noted portioning of Li atoms within and stoichiometric deviation for T_1 precipitates with Mg enrichment potentially indicating non-equilibrium conditions.

FSW

Oertelet et al. in work on thermal cycling of 5.8 mm thick AA2195-T8 FSW employed TEM micrographs to analyze precipitation. [66] The BM contained a high-volume fraction of T_1 precipitates which had a hexagonal flake or needle-like appearance, 50 nm

in length and 1 nm in thickness along the <011>Al zone axis, θ' (Al_2Cu) as also observed as a tetragonal disc, and finally the intermetallic τ_2 (Al_7Cu_2Fe) was witnessed. In the SZ the T_1 precipitates were no longer present having dissolved, spherical δ' (Al_3Li) measuring 50-100 nm and spherical β' (Al_3Zr) were observed. In the HAZ and TMAZ, the T_1 and θ' precipitates were almost entirely dissolved into the matrix while τ_2, δ', and β' were observed.

Fonda and Bingert studied 25 mm thick AA2195 FSW at an "underaged temper" using TEM. [59] T_1(Al_2CuLi), θ'(Al_2Cu), δ' (Al_3Li), β' (Al_3Zr), and T_B (Al_7Cu_4Li) precipitates were observed, **Table A1-9**, though no comments were made regarding size. Additional studies are referenced but not detailed. [71], [101]–[104]

1.8.3 AA2219/AA2195

The studies on dissimilar AA2219/AA2195 FSW and SRFSW are exceptionally limited and especially in precipitate study.

In studies of dissimilar SRFSWs of AA2219/AA2195 Taylor characterized precipitation via SEM, EDS, TEM, and SAED. [105] A clear weld interface was observed with a higher volume fraction of precipitates observed on the AA2219 side (advancing side). This work identified the intermetallic Al_7Cu_2Fe as well as θ' and θ precipitates with θ measuring 10-20 μm in the near transition region. This study primarily focused on the weld interface and fracture regions and did not provide specifics for precipitate size or orientation measurements.

Appendix

Table A1-1: Composition limits of AA2219 (wt.%) [5]

Element	Limits	Element	Limits
Al	balance	V	0.05-.15
Cu	5.8-6.8	Zn	0.10 max
Mn	0.20-.40	Mg	0.02 max
Fe	0.30 max	Other (each), max	0.05
Zr	0.10–0.25	Other (total), max	0.15
Si	0.20 max		

Table A1-2: Composition limits of AA2195 (wt.%) [13]

Element	Limits	Element	Limits
Al	Bal	Zr	0.08–0.16
Cu	3.7–4.3	Fe	0.15 max
Li	0.8–1.2	Si	0.12 max
Mg	0.25–0.80	Ti	0.10 max
Ag	0.25–0.6	Other (each), max	0.05
Mn	0.25 max	Other (total), max	0.15
Zn	0.25 max		

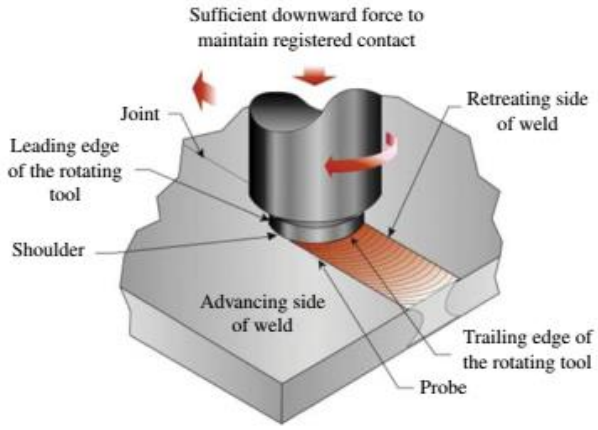

Figure A1-1 Schematic of the FSW process [18]

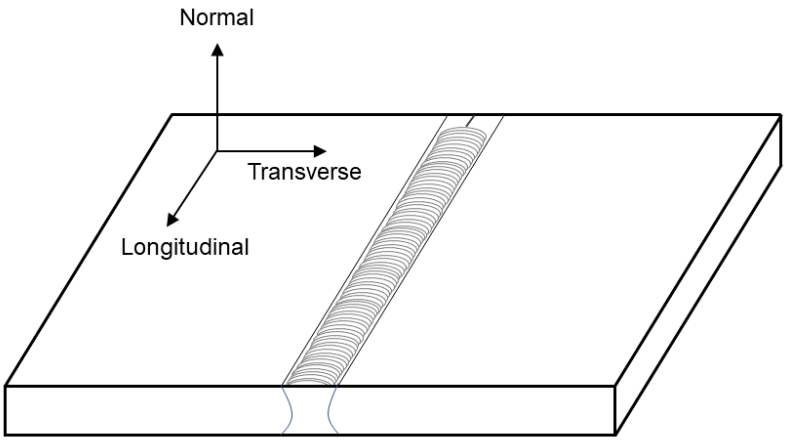

Figure A1-2 Weld plate and weld directions

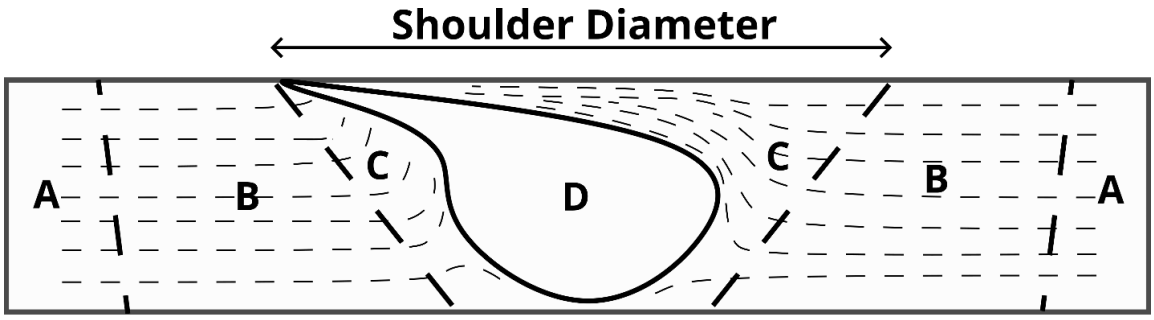

Figure A1-3 Schematic of FSW zones: (a) Base metal, (b) Heat-affected zone, (c) Thermo-mechanically affected zone, (d) Stir zone adapted from [21]

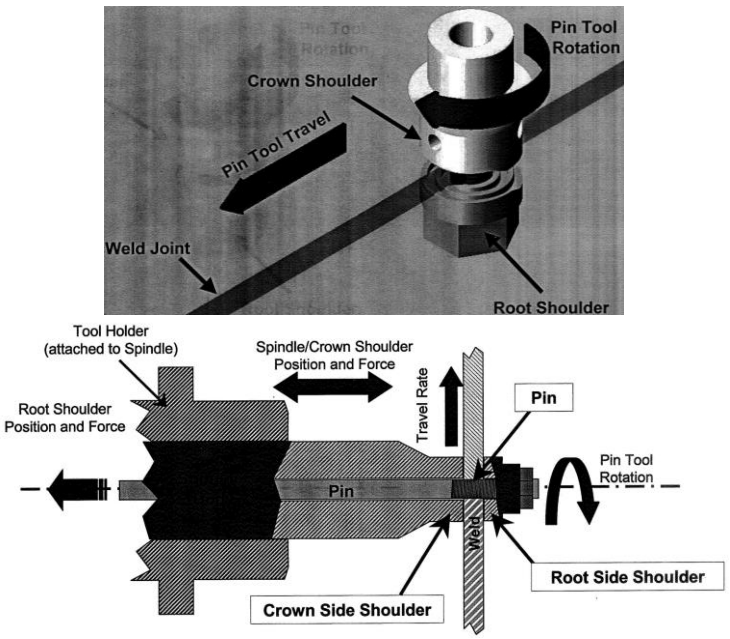

Figure A1-4 SRFSW schematic showing weld process (top) and tool (bottom) [27]

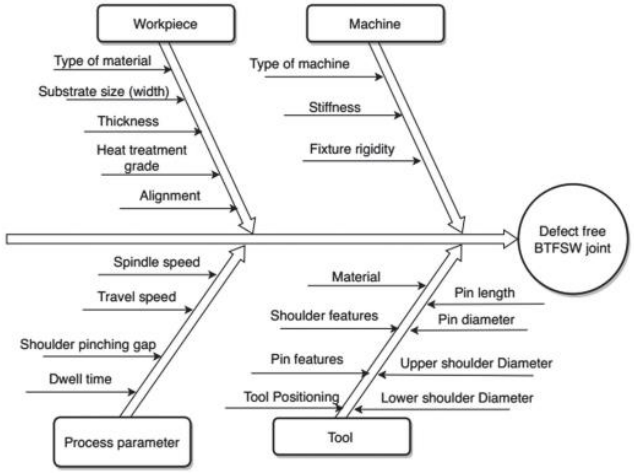

Figure A1-5 Cause and effect diagram for defect-free BTFSW joint [25]

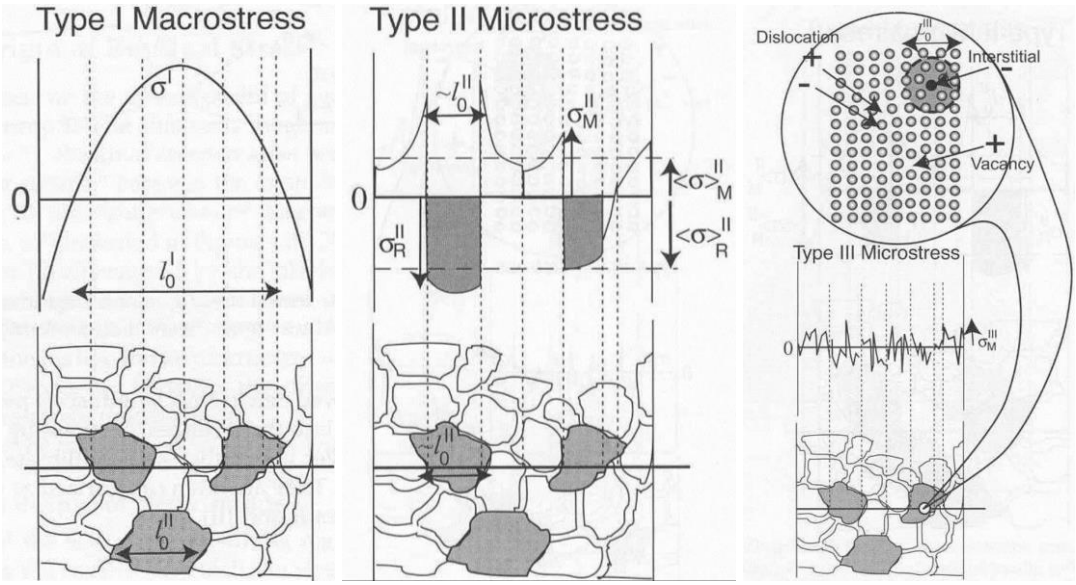

Figure A1-6 Residual stress length scale variation for (left) Type I, (center) Type II, and (right) Type III [32]

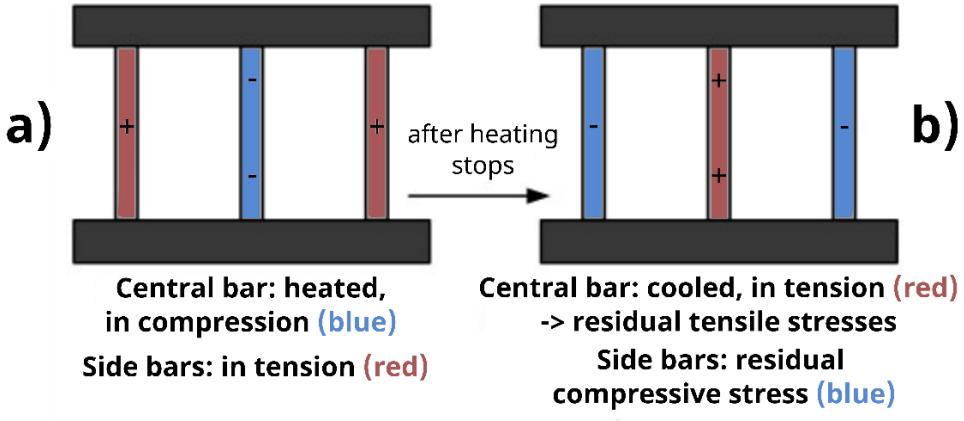

Figure A1-7 Three bar problem stresses during (a) heating and (b) cooling *adapted from* [33]

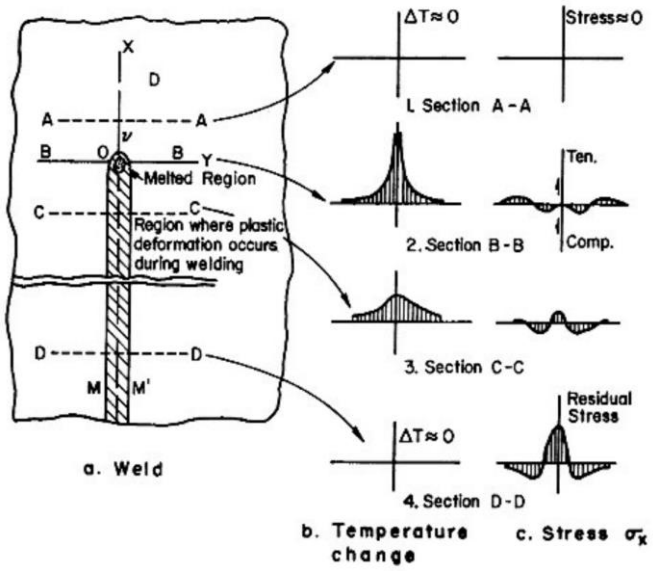

Figure A1-8 Stress and temperature change during welding [34]

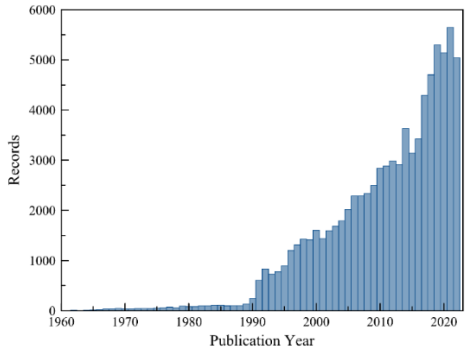

Figure A1-9 Web of Science Literature Search results for the topic “Residual Stress” by year

Table A1-3: Comparison of residual stress measurement techniques adapted from [35]

Technique	Destructive?	Availability	Speed	Equipment Cost	Measurement Cost	Expertise Required	Resolution	Stress state
Layer Removal/ Sectioning	Yes	General	Med	Med	Low	Med	Material and method dependent	Uniaxial Biaxial
Hole Drilling	Semi	Widespread	Fast/ Med	Fast/ Med	Low	Med	50-100 µm depth increment	Uniaxial Biaxial
Synchrotron	No	Specialist	Fast	Facility level	High	High	20 µm lateral, 1 mm parallel to beam	Uniaxial Biaxial Triaxial
Neutron Diffraction	No	Specialist	Med/ Slow	Facility level	High	High	500 µm	Uniaxial Biaxial Triaxial
X-ray Diffraction	No	General	Fast/ Med	Med	Med	Med	20 µm depth, 1 mm laterally	Uniaxial Biaxial
Ultrasonic	No	General	Rapid	Med	Low	Med	5 mm	Uniaxial Biaxial
Raman	No	General	Rapid	Med	Low	Low	0.5 µm	Uniaxial Biaxial

Table A1-4: Advantages and disadvantages of residual stress measurement techniques [29]

Technique	Advantage	Disadvantage
X-ray diffraction	- Ductile - Generally available - Wide range of materials - Hand-held systems - Macro and Micro RS	- Lab-based systems - Small components - Only basic measurements
Hole Drilling	- Fast, - Easy use - Generally available - Hand-held - Wide range of materials	- Interpretation of data - Semi destructive - Limited strain sensitivity and resolution
Neutron Diffraction	- Macro and Micro RS - Optimal penetration & resolution - 3D maps	- Only specialist facility - Lab-based system
Barkhausen Noise	- Very quick - Wide sensitivity to microstructure effects especially in welds - Hand-held	- Only ferromagnetic materials - Need to divide the microstructure signal from that due to stress
Ultrasonic	- Generally available - Very quick - Low cost - Hand-held	- Limited resolution - Bulk measurements over whole volume
Sectioning	- Wide range of material - Economy and speed - Hand-held	- Destructive - Interpretation of data - Limited strain resolution
Contour	- High-resolution maps of the stress normal to the cut surface - Hand-held - Wide range of material - Larger components	- Destructive - Interpretation of data - Impossible to make successive slices close together
Deep hole drilling	- Deep interior stresses measurement - Thick section components - Wide range of material	- Interpretation of data - Semi destructive - Limited strain sensitivity and resolution
Synchrotron	- Improved penetration & resolution of X-rays - Depth profiling - Fast - Macro and micro RS	- Only specialist facility - Lab-based systems

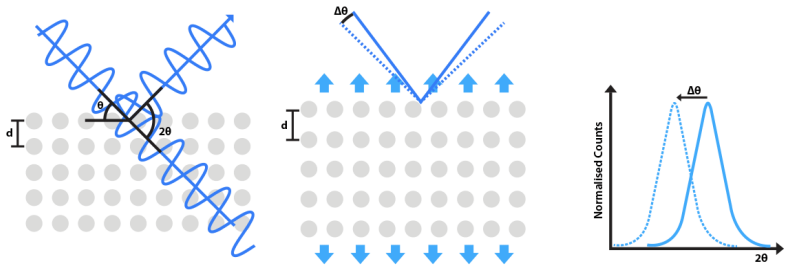

Figure A1-10 Illustration of incident and diffracted beam related to scattering angle change [37]

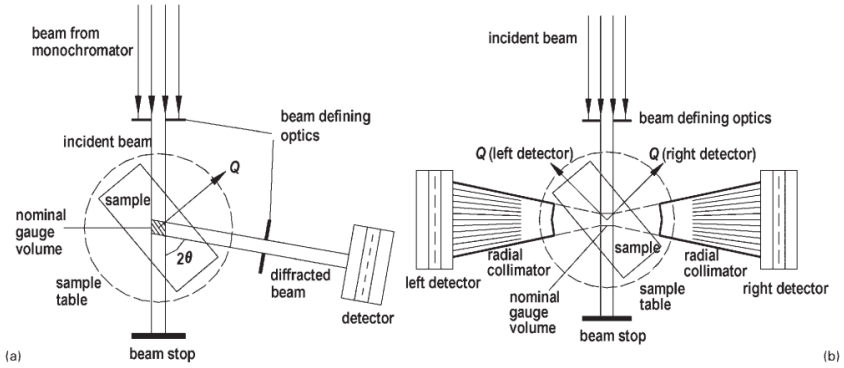

Figure A1-11 Illustration of (a) reactor based diffractometer (b) spallation based diffractometer for residual stress experiment [39]

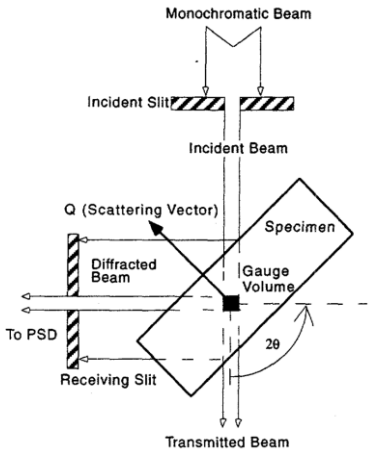

Figure A1-12 Schematic of reactor-based instrument optics (PSD is position-sensitive detector) [41]

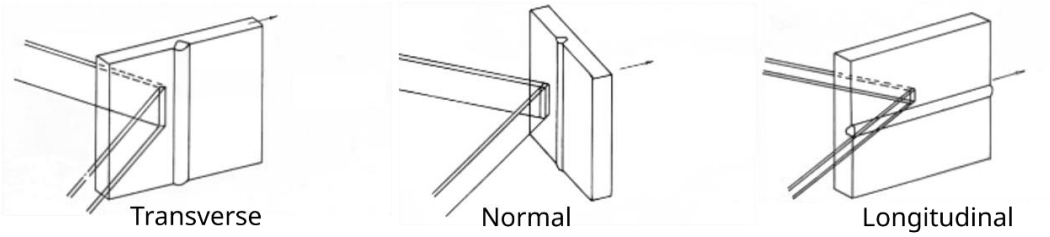

Figure A1-13 Schematic of gauge and scattering volumes for the transverse, normal, and longitudinal directions

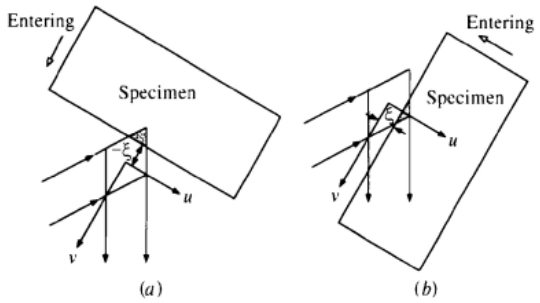

Figure A1-14 (a) reflection geometry and (b) transmission geometry [40]

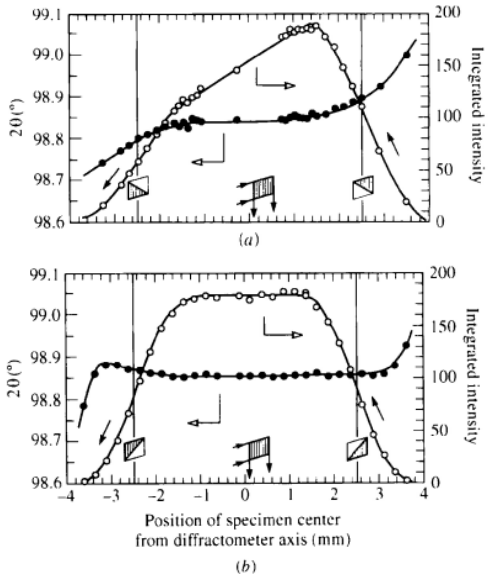

Figure A1-15 *2θ* (311) reflection Ni (a) reflection geometry (b) transmission geometry [40]

Table A1-5: Lattice planes and intergranular strain response *adapted from* [32]

Material	Recommended Planes (Weakly Affected by Intergranular Strains)	Problematic Planes (Strongly Affected by Intergranular Strains)
FCC (Ni, Fe, Cu)	(111), (311), (422)	(200)
FCC (Al)	(311), (422), (220)	(200)
BCC (Fe)	(110), (211)	(200)

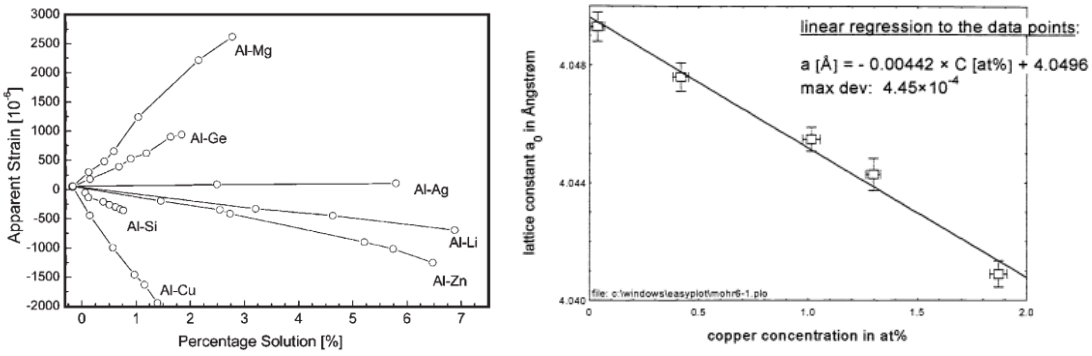

Figure A1-16 Apparent microstrain vs composition [32] (left) lattice constant vs copper concentration in for the $Al_{1-x}Cu_x$ solid solution [43] (right)

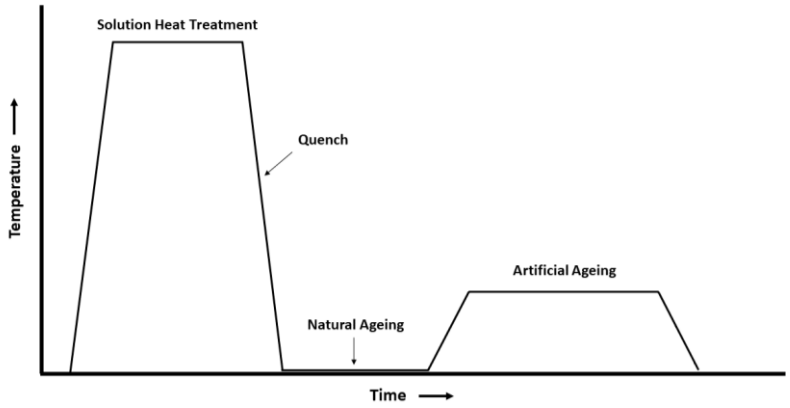

Figure A1-17 Typical heat treatment regime for precipitation hardenable aluminum alloys adapted from [4]

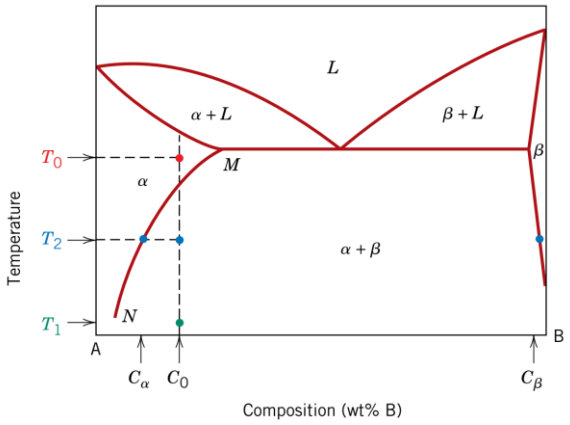

Figure A1-18 Hypothetical binary phase diagram for a precipitation-hardenable alloy of composition C_0 [51]

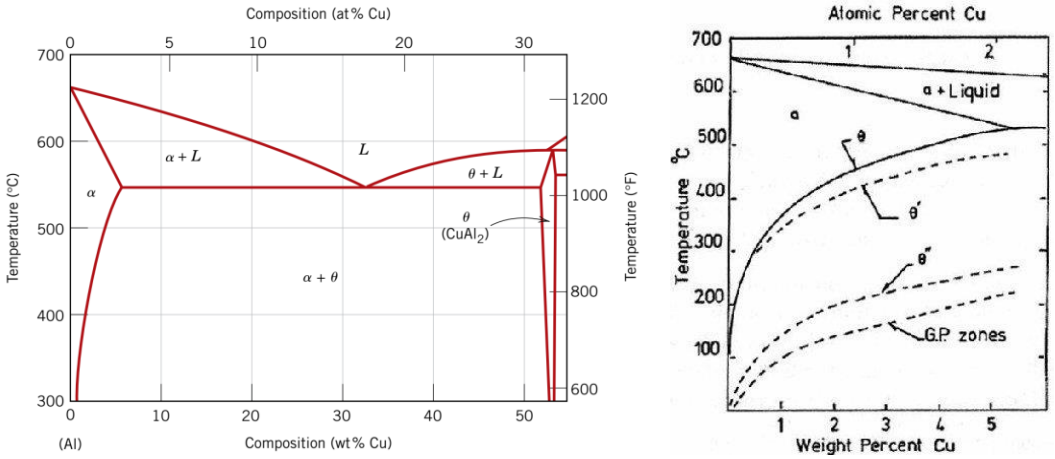

Figure A1-19 Al-Cu binary phase diagram (left) [51] and with approximate metastable precipitate solvus temperature (right) [52]

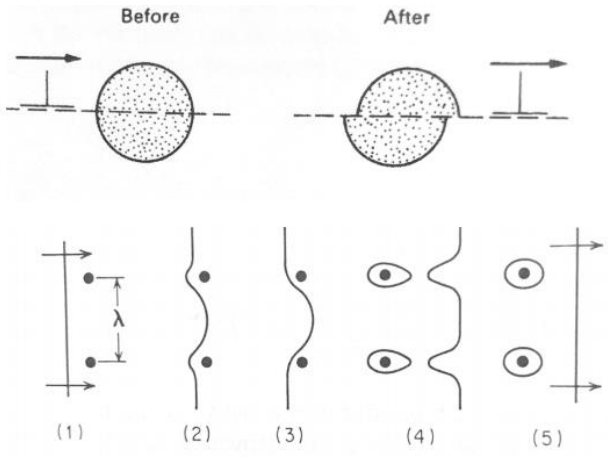

Figure A1-20 Precipitate strengthening mechanisms: dislocations either shear particles (top) or loop around particles (bottom) [53]

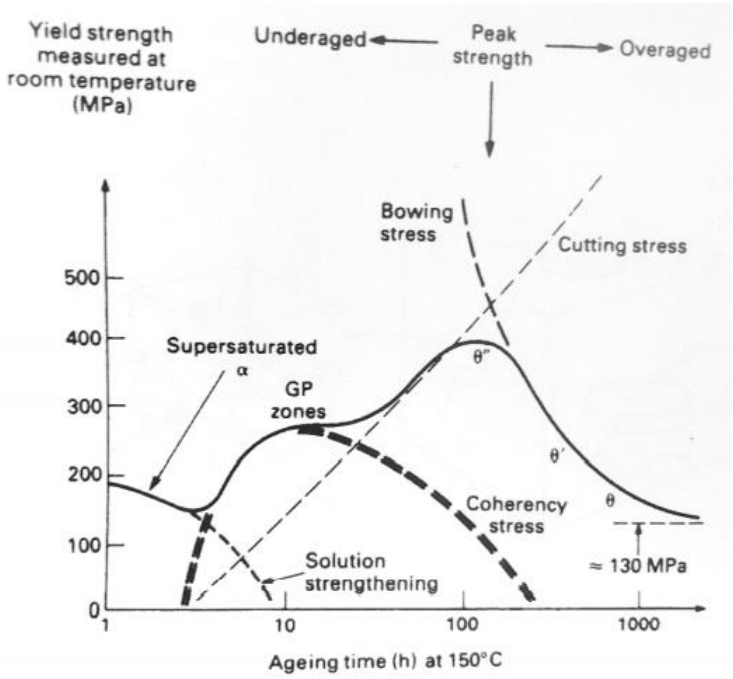

Figure A1-21 Age-hardening behavior of Al-Cu system showing the precipitates formed at 150 °C over time and the preferred dislocation motion mechanism

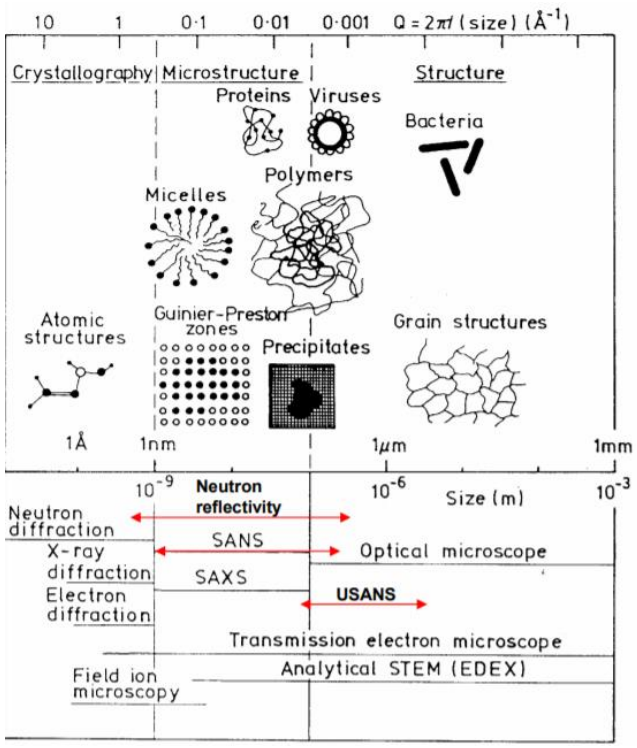

Figure A1-22 Effective size range of microscopy and scattering techniques [73]

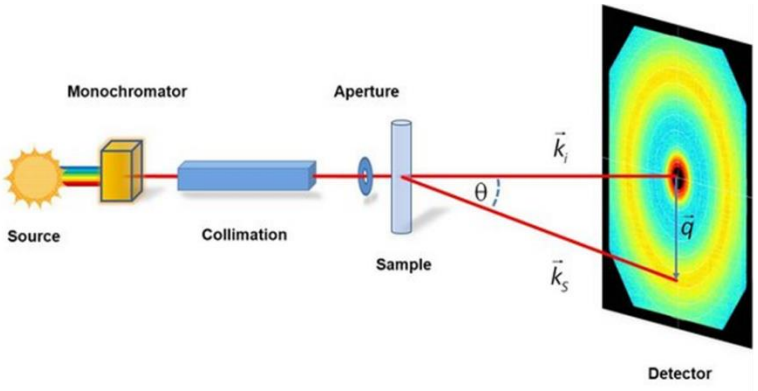

Figure A1-23 Schematic of small-angle scattering [74]

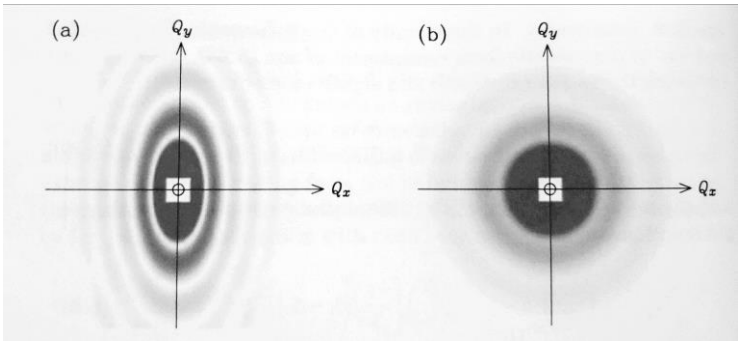

Figure A1-24 2D scattering pattern from a dilute solution of identical ellipsoids of principal axis ratio 2:1:1 with (a) the long axis aligned with the z direction and (b) random orientation [73]

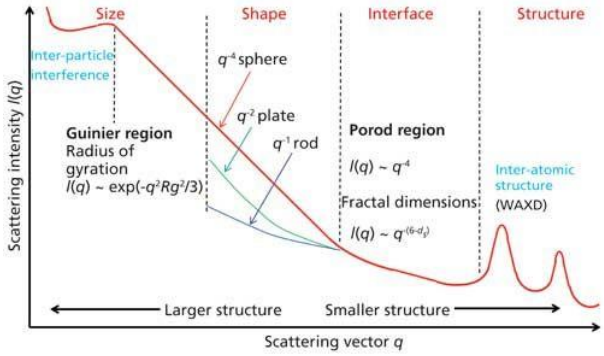

Figure A1-25 1D SAS pattern information [75]

Table A1-6: Literature for SAXS precipitate characterization in aluminum alloys

Author	Title	Date	Alloy	System	Process	Citation
Avettand-Fenoel et al.	Effect of the ageing on precipitation spatial distribution in stationary shoulder friction stir welded AA2050 alloys	2019	AA2050-T8	Al-Li-Cu	Stationary shoulder FSW	[78]
dos Santos et al.	Understanding precipitate evolution during friction stir welding of Al-Zn-Mg-Cu alloy through in-situ measurement coupled with simulation	2018	AA7449-TAF	Al-Zn-Mg-Cu	FSW	[79]
Panagos et al.	Characterising precipitate evolution in multi- component cast aluminium alloys using small-angle X-ray scattering	2017	$Al_3Zr_xV_{1-x}$	Al-Zr-V	Casting	[72]
Zhang et al.	In situ structural characterization of ageing kinetics in aluminum alloy 2024 across angstrom-to-micrometer length scales	2016	AA2024	Al-Cu-Mg	Heat treatments	[80]
Malard et al.	Microstructure distribution in an AA2050 T34 friction stir weld and its evolution during post-welding heat treatment	2015	AA2050 T34	Al-Li-Cu	FSW	[81]
De Geuser et al.	Microstructure mapping of a friction stir welded AA2050 Al–Li–Cu in the T8 state	2014	AA2050-T8	Al-Li-Cu	FSW	[82]
Steuwer et al.	A combined approach to microstructure mapping of an Al–Li AA2199 friction stir weld	2011	AA2199	Al-Li-Cu	FSW	[83]
De Geuser et al.	Mapping the microstructure of a friction-stir welded (FSW) Al-Li-Cu alloy	2010	AA2098/2050	Al-Li-Cu	FSW	[84]
Sullivan and Robson	Microstructural properties of friction stir welded and post-weld heat-treated 7449 aluminium alloy thick plate	2008	AA7449	Al-Zn-Mg-Cu	FSW	[85]
Dumont et al.	Microstructure mapping in friction stir welds of 7449 aluminium alloy using SAXS	2006	AA7449 (T3/T79)	Al-Zn-Mg-Cu	FSW	[86]
Sullivan et al.	Microstructural evolution in AA7449 plate subject to friction stir welding and post weld heat treatment	2006	AA7449	Al-Zn-Mg-Cu	FSW	[87]
Dumont et al.	Characterisation of the composition and volume fraction of η′ and η precipitates in an Al–Zn–Mg alloy by a combination of atom probe, small-angle X-ray scattering and transmission electron microscopy	2005	AA7108.50	Al-Zn-Mg	N/A	[88]
Genevois et al.	Quantitative investigation of precipitation and mechanical behaviour for AA2024 friction stir welds	2005	AA2024 (T351/T6)	Al-Cu-Mg	FSW	[77]

Table A1-7: Literature for SANS precipitate characterization

Author	Title	Date	Alloy	System	Process	Citation
Bokuchava et al.	Characterization of precipitation in 2000 series aluminium alloys using neutron diffraction, SANS and SEM methods	2019	AA2014/2124	Al-Mg	Heat treatments	[89]
Dawson et al.	Impact of friction stir welding on the microstructure of ODS steel	2017	MA956	ODS	FSW	[90]
Bardel et al.	Coupled precipitation and yield strength modelling for non-isothermal treatments of a 6061 aluminium alloy	2014	AA6061	Al-Mg-Si	Heat treatments	[91]
West et al.	Friction stir welding of oxide dispersion strengthened alloy MA956	2011	MA956	ODS	FSW	[92]
Etienne et al.	Effects of friction stir welding and post-weld annealing on nanostructured ferritic alloy	2010	NFA	NFA	FSW	[93]
Mathon et al.	Study of PM2000 microstructure evolution following FSW process	2009	PM2000	ODS	FSW	[94]
Miao et al.	The microstructure and strength properties of MA957 nanostructured ferritic alloy joints produced by friction stir and electro-spark deposition welding	2007	MA957	NFA	FSW/ESDW	[95]

Table A1-8: DSC Analysis results of different samples [58]

	I (Dissolution of GP Zones)		II (Dissolution of θ'' Phase)		III (Formation of θ' Phase)		IV (Formation of θ Phase)	
	Beginning Temperature	Peak area (J/g)	Beginning Temperature	Peak area (J/g)	Beginning Temperature	Peak area (J/g)	Beginning Temperature	Peak area (J/g)
2219-W	359 K (86 °C)	2.61	—	—	501 K (228 °C)	20.21	698 K (425 °C)	1.39
2219-O								
BM	—	—	—	—	—	—	—	—
HAZ	—	—	—	—	—	—	—	—
TMAZ	—	—	—	—	—	—	—	—
WNZ	—	—	—	—	493 K (220 °C)	10.04	—	—
2219-T8								
BM	—	—	453 K (180 °C)	0.76	497 K (224 °C)	2.36	—	—
HAZ-20	—	—	453 K (180 °C)	0.65	497 K (224 °C)	2.41	—	—
HAZ-10	—	—	—	—	478 K (205 °C)	4.40	—	—
TMAZ	355 K (82 °C)	0.66	—	—	493 K (220 °C)	13.68	—	—
WNZ	361 K (88 °C)	1.0	—	—	493 K (220 °C)	17.16	698 K (425 °C)	0.51

Table A1-9: Observed precipitate phases and weld locations *adapted from* [59]

Precipitate	Composition	Location
θ'	Al_2Cu	BM, HAZ, TMAZ
T_1	near Al_2CuLi	BM, HAZ, TMAZ
δ'	Al_3Li	TMAZ, SZ
β'	Al_3Zr	
GP zone	Cu	TMAZ, SZ
T_B	Al_7Cu_4Li	SZ

CHAPTER II
NEUTRON DIFFRACTION RESIDUAL STRESS STUDY OF A AA2219-T87 SELF-REACTING FRICTION STIR WELD – PART I

A version of this chapter is under review for publication by Benjamin Joe Wing, Dov Polsky, Jeffrey R. Bunn, Edward A. Payzant, Fredrick N. Michael, and Claudia J. Rawn: Juanita Q. Vera:

B.J. Wing, D. Polsky, J.R. Bunn, E.A. Payzant, F.N. Michael, C.J. Rawn, "Residual Stress Study of a AA2219-T87 Self-Reacting Friction Stir Weld with Neutron Diffraction – Part I", *Journal of Materials Engineering and Performance*.

The article is presented as it was submitted, without change. Portions of the Chapter I were used in this publication. Benjamin Joe Wing and Dov Polsky completed and analyzed the metallography. Kevin Sisco performed the microhardness testing. Microhardness data was analyzed by Benjamin Joe Wing. Neutron diffraction data was collected and analyzed by Benjamin Joe Wing, Jeffrey Bunn, Edward Payzant. Benjamin Joe Wing and Claudia Rawn wrote the paper.

2.1 Abstract

2219-T87 is a precipitation hardenable aluminum-copper alloy which sees wide use in structural aerospace components. Thick panels of this alloy are joined via self-reacting friction welding (SRFSW); however, this thermomechanical process can result in significant loss of the alloy's strengthening precipitates and large residual stresses which are detrimental to mechanical behavior and performance.

High-resolution maps of the residual strain and stress states along the normal, transverse, and longitudinal directions of 2219-T87 SRFSW were obtained using neutron diffraction measurements. Residual stress had the highest tensile value in the heat affected zone (HAZ) and largest compressive stress in the base metal region of the normal and transverse directions. Residual stress distributions displayed an 'M'-shaped distribution in each direction with the longitudinal direction being the most pronounced. Microhardness testing across the transverse weld section produced a 'V'-shaped curve with slight hardness recovery in the stir zone. Maximal and minimal microhardness values were observed in the base metal and thermomechanically affected zone,

respectively. Microstructural evolution was recorded using optical microscopy and showed decreasing grain size from the HAZ to the stir zone.

2.2 Introduction

Precipitation hardenable 2xxx aluminum alloys possess high strength and ductility, low density, good corrosion resistance, and stable cryogenic performance making them ideal for structural aerospace applications such as liquid propellant rocket fuel tanks. [106] However, joining these alloys via fusion-based processes introduces additional risk for detrimental issues such as porosity, solidification cracking, loss of mechanical properties (i.e., joint softening). [14], [106]

Friction stir welding (FSW) is a solid-state process which solves many of the issues associated with fusion-based processes. [14], [17], [106] In FSW a rotating tool consisting of a shoulder and pin travels along abutting or overlapping plates and mixes the joint edges. Frictional heat produced by the rotating tool softens the material while the shearing action of the tool shoulders and pin provide material mixing and bonding of the plates. Careful selection of processing parameters for FSW improves the stability and repeatability of the weld joint properties when compared to its fusion-based counterparts. [17]

Self-reacting friction stir welding (SRFSW) – sometimes known as bobbin tool friction stir welding or self-support friction stir welding – is a variant of FSW which allows for joining thick and circular plates. SRFSW operates on the same principle as FSW but with an additional shoulder at the root. The root side shoulder eliminates the need for backing plates, increases efficiency, improves heat distribution and resulting microstructure, and creates high strength welds. [25], [26]**.** However, residual stresses remain a concern.

Residual stresses are stresses present in a solid in the absence of external forces and are the result of misalignments between regions in the material. In the case of SRFSW these misalignments are primarily the result of differences in thermomechanical deformation within the joint. Accounting for residual stress in weldments is important as they can negatively impact material performance and accelerate failure. [38] Joint softening, a loss

of mechanical properties along the weld, in aluminum 2xxx alloys is often due to changes in precipitate size and distribution as well as increased residual stresses. Joint softening has been noted in AA6061, AA6056-T78, and AA2024 SRFSWs though the extent of its effects and relation to residual stresses are not well documented. [26], [107]–[111] Unfortunately, while residual stress distribution in traditional FSW is widely researched, there is limited research on residual stress for SRFSW and considerably less for this specific alloy.

Neutron diffraction was selected to comprehensively map the residual strain/stress state. Evaluating residual stress via neutron diffraction offers several key benefits for modeling efforts including high resolution, excellent material penetration allowing for three-dimensional mapping of subsurface residual stresses, bulk measurement, and non-destructive measurement. [32]

In this study neutron diffraction is employed to measure residual strain and stress in a 2219-T87 SRFSW. Strain and stress evolution within the welds is discussed in conjunction with microhardness, elastic modulus, and microstructural changes.

2.3 Experiment/Methods

A thick plate, 2219-T87 SRFSW in butt weld configuration was prepared at NASA Marshall Space Flight Center (MSFC) using proprietary processing parameters and tool design.

2.3.1 Microstructure

To assist in gauge volume selection and ensure that the neutron diffraction measurements were unaffected by variations in grain size, microstructural analysis of the weld was conducted.

Microscopy

Specimens were sectioned from the weld using wire electrical discharge machining (EDM), mounted in epoxy, and successively ground and polished to 0.05 μm colloidal silica. The sample was immersed in Weck's reagent for 10 s then removed and rinsed with cold deionized water.

The etched specimens were imaged using a Nikon Eclipse MA200 at magnifications up to 500x in each weld region. A macrograph of the weld joint was constructed by stitching images taken using a Keyence VHX-1000 in *Fiji* (*ImageJ*). [112] Grain sizes were measured with *ImageJ* using the intercept method according to ASTM E112. [113] Macroprecipitates were manually counted using 50x optical micrographs for the advancing side base metal (BM), HAZ, and SZ and 100x optical micrographs for the TMAZ, each sampled at three random locations in *ImageJ* to obtain number and linear number density.

2.3.2 Microhardness

Microhardness measurements were performed on an epoxy mounted, ground, and polished transverse weld cross-section of 5 mm thickness**.** Measurements were taken using a LECO AMH 55 at intervals of 0.75 mm to the sample edge in the normal (y direction) and transverse (x direction) directions using a load of 500 gf (4.903325 N) and 15 s dwell time.

2.3.3 Neutron Diffraction Measurements

Neutron diffraction measurements were carried out at the High Flux Isotope Reactor (HFIR) of Oak Ridge National Laboratory (ORNL) on the High Intensity Diffractometer for Residual Stress Analysis (HIDRA). [114], [115] The instrument's incident wavelength is defined by a bent Si crystal focusing Popovicci-Stoica monochromator and can be adjusted to suit a variety of materials. [116] The Al (311) reflection was selected for this study as it has a relatively high peak intensity (for more rapid data collection), a high multiplicity (and so less impacted by texture), an elastic modulus very close to the bulk modulus, and is not readily affected by intergranular strains. [32], [39] The Si (331) monochromator setting was used to provide a wavelength of l =1.731 Å and a scattering angle of ~90° for the Al (311).

The plate center was selected as the origin and coarsely aligned via an optical telescope. Prior to measurements "edge scans" were performed to account for geometric deviations of the plate and form a virtual coordinate system related to the sample coordinate system. Measurements in the three orthogonal directions (transverse, normal, and longitudinal –

Figure A2-1) were performed in increments of: 1.066 mm along the plate thickness to +/- 70 mm in the longitudinal direction, +/- 100 mm in the transverse direction, and from -100 to 80 mm in the normal direction as measured from the weld centerline.

Gauge volume
A cubic gauge volume (2 x 2 x 2 mm) was chosen for the longitudinal direction measurement. In the transverse and normal directions, in which weld symmetry can be assumed, a tall, matchstick-like gauge volume (2 x 20 x 2 mm) was chosen to reduce counting and instrument time.

d_0 determination/selection
The thermomechanical nature of the SRFSW process leads to a considerable change in both chemistry and microstructure across the 2219-T87 weld which if unaccounted result in a large difference between apparent and actual strain/stress. [32], [42] Therefore, the determination of a stress-free reference *d*-spacing, d_0, is essential to obtaining an accurate result.

A stress-free reference (d_0) comb was created after the orthogonal measurements to avoid potential stress relaxation along those directions. [14] This stress-free reference comb allows for mechanical relaxation of local macrostresses and accounts for changes in chemical composition, attributed to the Al-Cu solid solution, and microstructure across the weld. The weld plate was sectioned 233.68 mm from the weld terminus using a bandsaw to allow for construction of a stress-free reference comb. In constructing the comb, a portion of the weld was sectioned with EDM using 20 mm longitudinal cuts in 4 mm increments from +/- 60 mm from the weld centerline. Measurements in the transverse direction were taken at 2.133 mm intervals from the mid-thickness at intervals of 4 mm from the weld centerline 135 mm from the orthogonal measurements. The instrument was aligned to a mark on the weld centerline made during the previous measurement to maintain position consistency.

The d_0 data were obtained using a Si (422) monochromator (λ = 1.540 Å) which provides a scattering angle of ~78° for the Al (311). Two rectangular gauge volumes, 2 x 20 x 2 mm and 2 x 10 x 2 mm, were selected for measurement of the transverse direction with

the smaller gauge volume centered 15 mm from the plate end to evaluate the effect of the plate sectioning method, **Figure A2-2**. The *d*-spacing was determined from the measured scattering angle the using a pseudo-Voigt fitting function in PyRS. [117]

Determination of d-spacing, strain, and residual stress

The principle of diffraction/scattering is defined by Bragg's law, equation 2-1, which relates the wavelength (λ), interplanar or *d*-spacing (*d*), and scattering angle (2θ).

$$\lambda = 2dsin\theta \tag{2-1}$$

The wavelength is known and the scattering angle of the measured peak is obtained via peak fitting of the data, rearranging equation 2-1 the lattice *d*-spacing can be calculated from:

$$d = \frac{\lambda}{2\ sin\theta} \tag{2-2}$$

With the d-spacing determined, the residual strain for each principal direction becomes possible by relating the d-spacing difference between the measured point (*d*) and its stress-free reference (d_0) divided by the stress-free reference *d*-spacing (d_0).

$$\varepsilon = \frac{d-d_0}{d_0} \tag{2-3}$$

Using the computed residual strain in each principal direction as in equation 2-3, the calculation of residual stress becomes possible. [32], [38] Hooke's Law, equation 2-4, is applied along with isotropic conditions to provide the following relation, equation 2-5:

$$\sigma = E\varepsilon \tag{2-4}$$

$$\sigma_i = \frac{E}{1+\nu}\left[\varepsilon_{ii} + \left(\frac{\nu}{1-2\nu}\right)\ (\varepsilon_{11} + \varepsilon_{22} + \varepsilon_{33})\right] \tag{2-5}$$

where σ_i is the component of residual stress, E is the elastic (Young's) modulus, ν is Poisson's ratio, and ε_{ii} is the component of residual strain.

Model Selection

Residual stress calculations were completed under the assumptions of the Voigt model – in which all grains experience orientation independent uniform strain and elastic modulus and Poisson's ratio (calculated by averaging the elastic stiffness over all elements of the aggregate) are constant and isotropic (for AA2219-TA7 the average tensile and compressive values are E = 73.1 GPa and ν = 0.33). [32], [118] The Voigt model is selected as the contributions of *hkl* other than the Al (311) cannot be determined and error attributable to use of averaged elastic properties is minimal in a static experiment.

2.3.4 Force Balance

The definition of residual stress as a self-equilibrating stress present in a material in the absence of an external force provides a basis for an alternant d_0 determination and/or correction. Therefore, the sum of all stresses (and moments) must equilibrate across the cross-section provided the plate is static (i.e. absence of movement or active deformation), which is expressed in equation 2-6. The components of stress are defined by the force (F_{ij}) over the area (A) perpendicular to that force, equation 2-7. This area is related to the area between measurements and thus the area between the residual stress curve and zero stress value.

$$\Sigma\sigma_{11} = 0;\ \Sigma\sigma_{22} = 0;\ \Sigma\sigma_{33} = 0 \tag{2-6}$$

$$\sigma_{ij} = F_{ij}/A \tag{2-7}$$

Extrapolation

The force and moment balance approach are only valid over the length of the measured cross-section which is the plate width and thickness for this experiment. As the orthogonal direction measurements do not extend the span of this area, extrapolation of existing data points is required. The *d*-spacing values for d_0 and each orthogonal direction were extrapolated to the plate edges. *d*-spacing plots for each of these directions is presented in **Figure A2-3**. The average *d*-spacing difference (Δd) factoring in d_0 assists in the determination of an appropriate extrapolation method, **Figure A2-4**.

The average Δd compared to d_0 is relatively consistent for the transverse and normal directions but continues to increase in the longitudinal direction. This indicates that

extrapolation is reliable in the transverse and normal directions but not in the longitudinal direction. However, further trend evaluation shows the variation of Δd within each measurement line (thickness) is considerable from point to point and does not follow a discernable trend in any direction, **Figure A2-5**. Error bars are omitted and Bezier lines used to improve trend observation as such, these lines are not indicative of actual or predicted values between these points.

For this reason, the method evaluated was a constant extrapolation in which the last data points for each direction are held constant and extended throughout the desired range without any algorithmic adjustments.

The force balance approach leads to shifts in d_0 *d*-spacing values across the plate. This shift can be weighted to reflect individual changes in *d*-spacing at different locations; however, as the point-to-point correction factor is unknown and significant additional experimentation would be required, only a constant shift -henceforth referred to as a global shift – is considered. The value of this global shift was determined by solving the relation in equation 2-6 using the "Goal seek" function in Microsoft Excel and applied.

2.4 Results

2.4.1 Macro and Microstructure

The macrostructure and microstructure of the 2219-T87 SRFSW is presented by **Figure A2-6** and **Figure A2-7**, respectively. The HAZ was noted by coarsened grains compared to the base metal, the TMAZ by elongated and deformed grains, and the stir zone by fine equiaxed grains.

Grain size increased from the base metal to the HAZ and decreased significantly moving from the TMAZ to the SZ where it reached a minimum, **Figure A2-8**. Macroprecipitate number and linear density steadily decreased from the BM to the SZ, **Table A2-1**.

2.4.2 Microhardness

Mid-thickness microhardness values (+/- 2 mm thickness) were averaged to create a mid-thickness averaged line graph, **Figure A2-9** error bars are 1σ. Microhardness values follow a 'W-shaped' curve as is characteristic of FSWs. Microhardness values steadily decrease from the BM to the TMAZ and slightly recover in the SZ (~97 HV). Highest

values are observed in the BM (154 HV) and lowest in the retreating side TMAZ (82 HV).

2.4.3 Neutron Diffraction

d-spacing

d-spacing data for the normal, transverse, and longitudinal directions and d_0 was produced by peak fitting in PyRS. Outlying data points defined by deviations ≥ 1.5σ were removed and replaced with adjacent values. d_0 values lacked significant outliers and were unchanged. The normal, transverse, longitudinal, and d_0 *d*-spacing are compared in **Figure A2-10**. In general, the advancing side displays a more rapid change in *d*-spacing for each direction compared to the retreating side. The highest *d*-spacing was observed on the advancing side of the longitudinal direction with a slight decrease seen on the retreating side. The lowest *d*-spacings are seen in the SZ of the normal and transverse directions. Contour plots of the normal, transverse, longitudinal, and d_0 *d*-spacing are presented in **Figure A2-11**.

FWHM

Weld microstrain and microstructure variation can be expressed in general terms by plotting the full-width half maximum (FWHM) peak values for the Al (311) as in **Figure A2-12**. A clear decrease in the FWHM is observed from the BM to the SZ for all directions.

Strain

Normal, transverse, and longitudinal residual strains were measured and found to follow the characteristic distribution for friction stir welds. The longitudinal residual strain and stress along the weld is ‘M-shaped’ with the advancing side possessing a somewhat higher value compared to the retreating side and an overall decrease in tensile residual strain/stress in and just outside the SZ. The transverse/normal residual strains are slightly ’U-shaped’ with maxima in the BM and lower in comparison but having the greatest compressive strain/stress values in the SZ **(Figure A-13** and **Figure A-14)**. [38]

The maximal longitudinal residual strain occurred on the advancing side just outside the SZ while the minima was in the BM. The normal direction has a maximum tensile strain

in the BM and a minimum compressive strain in the SZ. The transverse direction has a comparable minimum compressive microstrain just outside the SZ and a maximal tensile microstrain in the HAZ.

Stress

Residual stress was calculated from equation 2-4 using literature values (E = 73.1 GPa and ν = 0.33) and residual strain measurements. **Figure A2-15** shows the 1D residual stress plots for each principal direction while **Figure A2-16** displays the contour plots. Both profiles show an 'M'-shaped distribution with the longitudinal component being approximately three times greater than the tensile and normal directions. The longitudinal residual stress component maximizes on the advancing side HAZ just before reaching the TMAZ and the highest compressive value is in the BM. The normal direction's highest tensile residual stress occurred on the advancing side HAZ and highest compressive residual stress was in the BM. The transverse direction had similar stress magnitudes with the highest tensile stress in the SZ and highest compressive in the BM. The maximal residual stress is 96.7% the reported yield stress of 2219-T87 though the average value at this position ranges from 60.6 - 85.6% of yield.

2.5 Discussion

Residual strain in a 2219-T87 SRFSW was successfully measured via neutron diffraction and used to calculate and map principal residual stresses. Chemical composition and microstructural variation across the SRFSW were accounted for by mechanical relaxation and measurement of a representative weld section.

2.5.1 Macro-Microstructure

Typical SRFSW macrostructure is observed including the hallmark hourglass-shaped SZ and a sharper TMAZ/SZ transition on the advancing side compared to the retreating side (**Figure A2-6**). The transition differences are consistent with increased advancing side deformation rate and orthogonal grain structure of the BM. [25], [26], [119], [120] There was no indication of weld defects such as voids, joint line remnants, etc.

Four distinct microstructural zones were observed: BM, HAZ, TMAZ, and SZ (**Figure A2-7**). The HAZ displayed an increase in horizontal and vertical grain size with a

reduction of macroprecipitate number and line density, consistent with coarsening of precipitates in this region. Grain size as well as macroprecipitate number and line density decreased significantly in the TMAZ and reached a minimum in the SZ. Grain size measurements in each weld zone were reasonably consistent compared with Anderson, **Table A2-2**, for the BM and SZ. However, significant variation between the two studies are observed in the TMAZ and HAZ. [121] This variation is likely due to a difference in sampled locations within each region and/or processing parameters. Grain size variation between the advancing/retreating sides and upper/lower shoulder was not explored in this study but is expected to be minimal.

Large grain size (> 50 μm) and grain asymmetry can lead to inaccuracy in peak positions and thereby residual strain and stress in neutron diffraction measurements. [30] This grain size related error was ruled out by ensuring intensity (counts/s) at several locations was well above background (> 400 counts/s) with well-defined Al (311) peaks for all gauge volumes. Further, normalized peak intensity (I/I_0) change was minimal indicating a lack of "edge effects" associated with abrupt texture change. Peak broadening, as represented by the FWHM, is the result of various contributions such as particle size, dislocations, stacking faults, microstrain, and steep strain gradients. [32] The FWHM shows interesting results that are beyond the scope of this study with decreasing FWHM values from the base metal to the stir zone (**Figure A2-12**). Grain size as a primary contributing factor was ruled out as the FWHM should increase with decreasing crystallite size and the Scherrer equation is not applicable for the relatively large grain sizes observed. Deconvolution is required to distinguish potential contributions such as dislocations and subgrain size and may warrant further exploration.

Macroprecipitates observed are likely θ (Al_2Cu) due to their large relative size whereas the primary strengthening agent (θ') is frequently too small to be detected in optical microscopy. However, observations of the θ precipitate can provide information about the overall precipitation state. As temperature increases the small, fine θ' precipitates transform into the larger θ precipitates which then coarsen until dissolution. Thus, this coarsening can be indicative of the relative dissolution of θ' into θ. [58], [96]

2.5.2 Microhardness

In conjunction with microstructural studies, microhardness profiles can assist in the explanation of physical properties within a weld. The microhardness profile displays the expected “W”-shaped and “hourglass” appearance for the line graph and contour plot, respectively.

Weld features such as the advancing and retreating sides are readily observed in both the mid-thickness averaged line graph and contour plot. The advancing side is noted by sharper transitions for the HAZ/TMAZ and TMAZ/SZ. The lowest microhardness values are observed on the retreating side of the weld. This aligns with higher expected temperatures on the retreating side compared to the advancing side, resulting in greater precipitate dissolution. [4],[5],[22],[23]

2219-T87 FSW microhardness results are highly correlated with macroprecipitate number/density and to a lesser extent grain size which agrees with literature reports on this and similar alloys. [2], [23], [25], [27], [28] In general, higher microhardness values are directly correlated with increased precipitate density and/or decreased grain size. [123] The results above support that the precipitate density appears to be the primary strengthening factor in the BM where microhardness and the average precipitate number and density are the highest. The microhardness decreases steadily across the wide HAZ where a decreased average precipitate number and density was observed relative to the BM. The microhardness values were lowest over the narrow TMAZ with observed lower precipitate number and density compared to both the BM and HAZ. There is a slight recovery of microhardness in the SZ where the precipitate number and density are at their lowest, suggesting that the recovery is at least partially associated with the smaller, equiaxed grain size. Other potential strengthening factors to the slight microhardness recovery are solid-solution strengthening and re-precipitation of fine θ’ and θ’’ particles in the SZ. [14], [57] However, determination of these potential contributions were beyond the scope of this study and therefore not pursued.

2.5.3 Strain

The residual strain was determined and found to have the greatest tensile value in the longitudinal direction and most compressive in the normal and transverse directions in the HAZ-SZ-HAZ region. Strain distribution and magnitude align well with expectations exhibiting a slight ‘W-shape’ with local strain peaks at the TMAZ to stir zone transition with the advancing side peak being larger. Local minima of both longitudinal strain and microhardness also occur in this region.

These positions may indicate increased material flow and local shear in this region leading to increased tensile strain/stress as grains are plastically deformed. The possibility of an erroneous strain due to edge effects or texture was evaluated using normalized peak intensity (I/I_0) analysis. This showed no significant intensity variation, indicating the change is unlikely due to these factors. Another possibility is the offset in d_0 d-spacing measurements lead to a local and erroneous strain/stress in this region; an idea which is discussed in depth in Part II and yielded insignificant difference.

2.5.3 Stress

The residual stress contours appear reasonable and follow expected patterns. The highest compressive stresses lie within the SZ of the normal and transverse directions while the maximum tensile residual stresses occur in the longitudinal direction on the advancing side HAZ. This tensile stress reaches a maximum just below the yield stress for 2219-T87. While limited residual stress data exists for SRFSW, the FSW process typically reports wide range of 20-70% of the yield stress depending on the welding parameters. [38]

The high value may appear somewhat concerning, however, it is not uncommon for solitary points or sections within a weld to approach the yield stress. [14] Within this context, this residual stress study is atypical in the sense that it represents a high-resolution dense mapping scheme thereby presenting enhanced opportunity to detect such values. Further, the average stresses at this location are lower and well in line with the expected maximal residual stress to yield stress ratio and more representative of overall trends.

Comparison of the residual stress distribution to prior studies

Residual stress studies of SRFSWs in literature are limited though do exist for FSW and fusion processes.

In work on similar variable polarity plasma arc (VPPA) welds of 2219-T87 and 2195-T8, Martukanitz et al. employed neutron diffraction on 5 mm weld plates (single pass with 2319 filler) to calculate the residual strain and stress in the longitudinal, normal, and transverse directions. [41] The study observed that peak tensile and compressive residual stresses were related to the position of minimum hardness in the HAZ just outside the fusion zone. The normal and transverse directions were tensile until ~16 mm from the fusion zone where they decreased into the compressive region. Maximal tensile residual stresses for the 2219-T87 plate were 50-, 10-, and 90- MPa for the transverse, normal, and longitudinal directions, respectively. The largest compressive residual stresses were ~-50 MPa for all directions.

In work on a similar 2219-T87 SRFSW plate of 15.875 mm thickness and proprietary tool and processing parameters, Anderson used x-ray diffraction to determine the surface residual stress. [121] Measurements were taken on the weld crown to a penetration depth of 94.16 μm (working volume 0.296 μm^3) along the transverse direction to $\pm$50 mm from the weld center and $\pm$152 mm from the origin along the longitudinal direction. Longitudinal residual stresses values were higher on the advancing side and remained consistent along the weld traverse while those on the retreating side were lower and increased significantly (5.9 to 109.3 MPa) along the weld. The maximal longitudinal residual stress was 117 MPa and occurred in the stir zone. The minimal longitudinal residual stress achieved was -94 MPa at the retreating-side TMAZ. Transverse residual stresses were generally compressive with a minimum of -75.3 MPa.

We have observed higher magnitudes of residual stress compared to the above studies but with a similar residual stress distribution in the longitudinal direction. However, the normal and transverse directions differed from expectations in that both displayed an ‘M’-shaped curve instead of a more compressive ‘U’- or ‘V’- shaped profile. The differences can be attributed to the differences to the welding technique (VPPA vs

SRFSW) and the use of neutron diffraction to determine residual stresses in internal locations compared to surface residual stresses via x-ray diffraction.

2.6 Conclusion

Neutron diffraction was conducted to determine residual strain and stress maps across a 2219-T87 SRFSW. Microhardness varied in proportion to the precipitate density and to a lesser extent grain size and correlated with residual stress. Residual stresses displayed an 'M'-shaped distribution in each direction with the longitudinal direction being approximately 3 times greater than the normal and transverse directions. Maximum longitudinal residual stresses were significant and approached the yield stress of the alloy.

2.7 Acknowledgements

The authors would like to acknowledge partial support though the Manufacturing and Materials Joining Innovation Center (Ma^2JIC) University of Tennessee, Knoxville site. Ma^2JIC is funded by the National Science Foundation (NSF) through the Industry/University Cooperative Research Center (I/UCRC) program award number IIP 1822186. This research used resources at the High Flux Isotope Reactor a DOE Office of Science User Facility operated by the Oak Ridge National Laboratory. The authors would like to thank Kevin Sisco for his contribution and assistance in microhardness testing.

Appendix

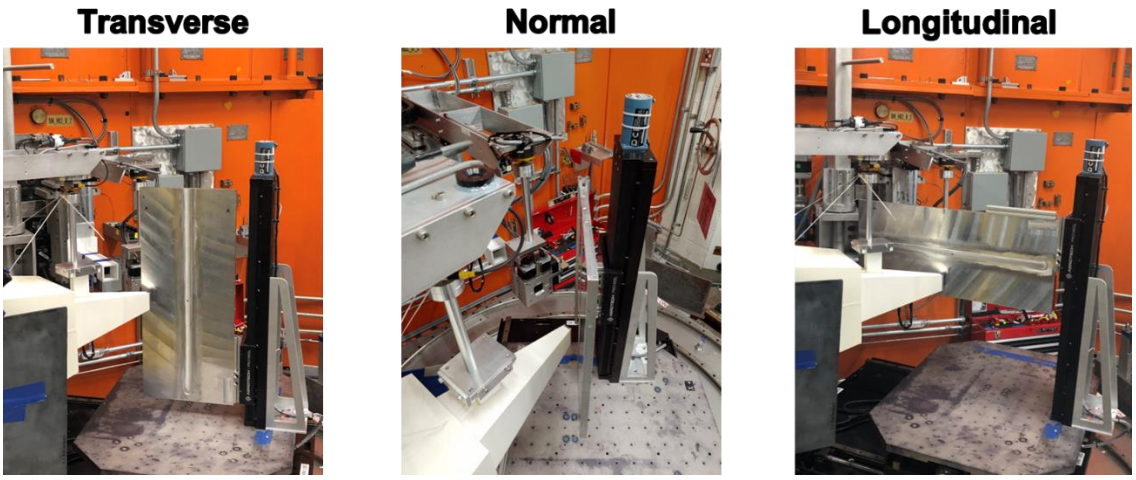

Figure A2-1 Images of the weld plate on the beamline at HIDRA HB2B in each measurement orientation



Figure A2-2 Stress-free reference comb illustrating large (blue) and small (orange) gauge volumes

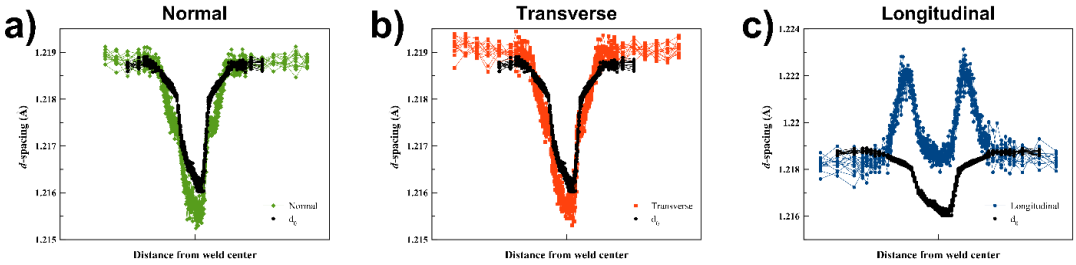

Figure A2-3 d-spacing and d0 comparison in the (a) normal, (b) transverse, and (c) longitudinal direction

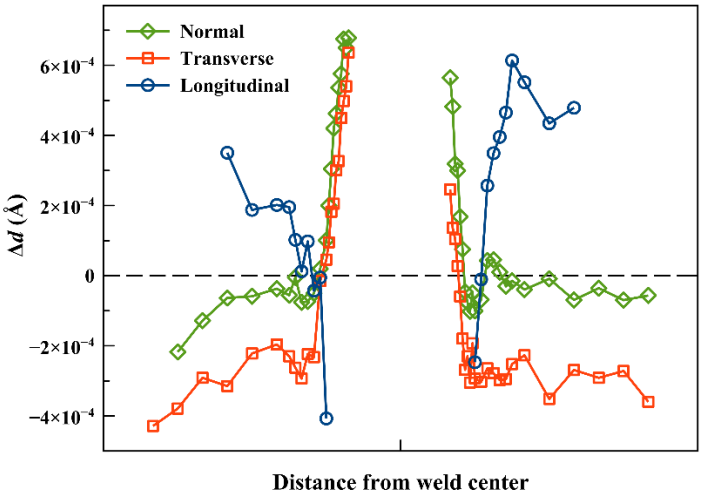

Figure A2-4 Average Δ*d* in each direction

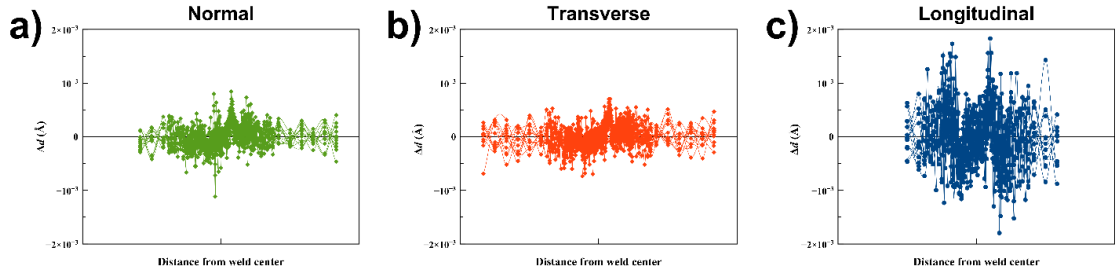

Figure A2-5 Δd in the (a) normal, (b) transverse, and (c) longitudinal direction



Figure A2-6 2219-T87 SRFSW macrograph

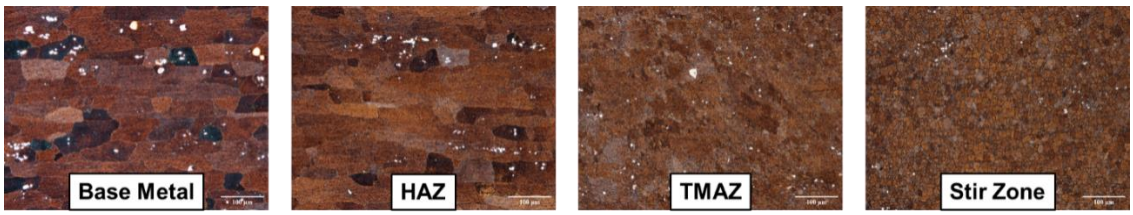

Figure A2-7 Micrographs of each weld zone in 2219-T87 SRFSW

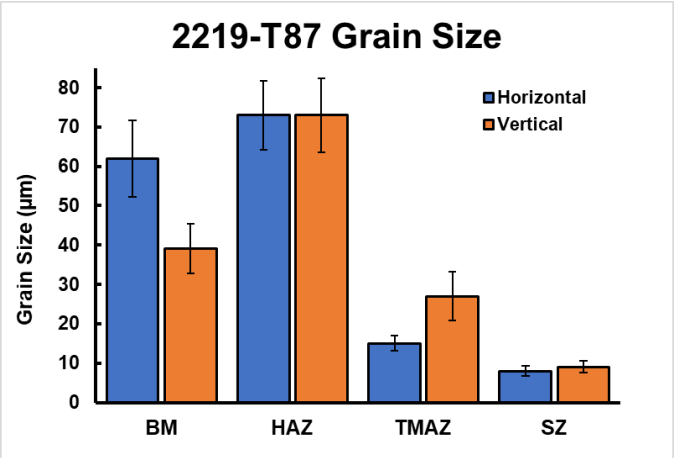

Figure A2-8 Horizontal and vertical grain sizes for each weld zone with standard deviation

Table A2-1: Image analysis of macroprecipitates from optical micrographs - number and linear number density for each weld zone

Weld Zone	Precipitate Number	Average Precipitate Number	Precipitate Density (#/µm)	Average Precipitate Density (#/µm)
Base Metal	115	107.33	.3496	.3263
	104		.31616	
	103		.31312	
HAZ	83	88.67	.25232	.2695
	93		.28272	
	90		.2736	
TMAZ	50	49.33	.152	.1500
	54		.16416	
	44		.13376	
Stir Zone	28	35.67	.08512	.1084
	42		.12768	
	37		.11248	

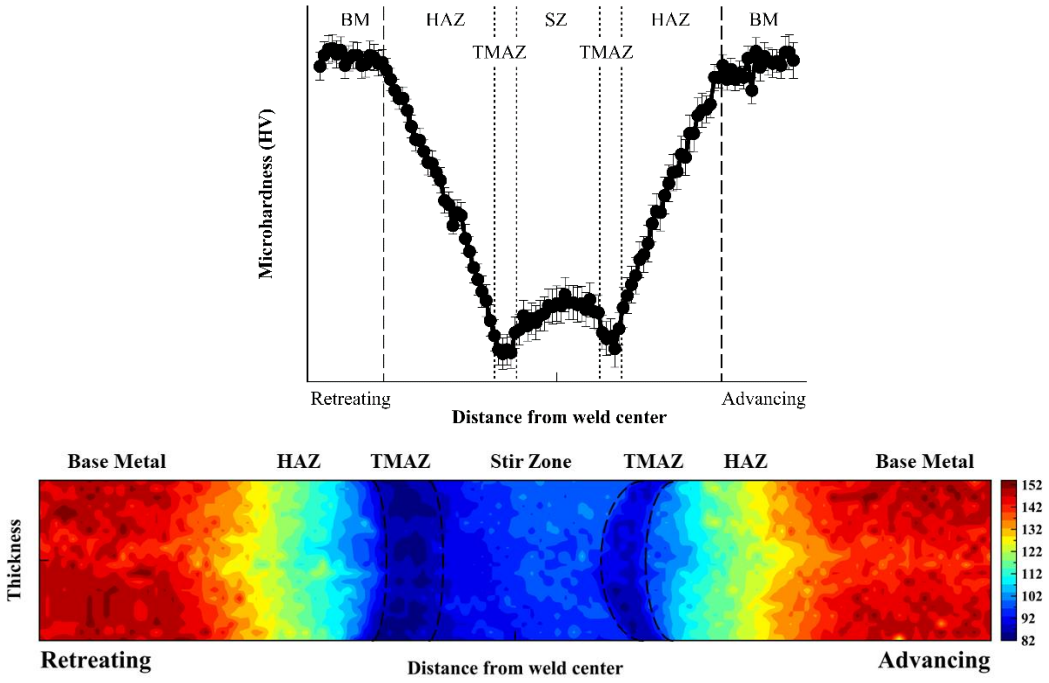

Figure A2-9 Microhardness (top) mid-thickness averaged line graph (1σ) (bottom) contour plot

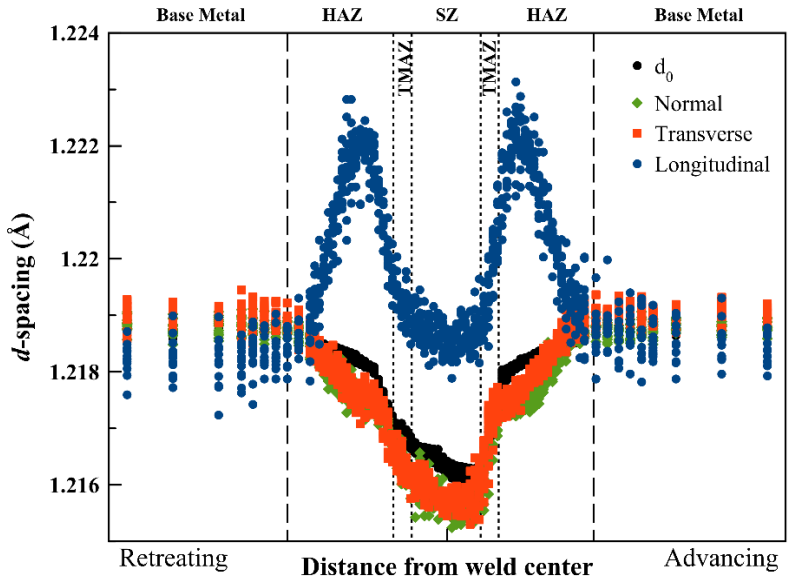

Figure A2-10 Normal, transverse, longitudinal, and d_0 *d*-spacing

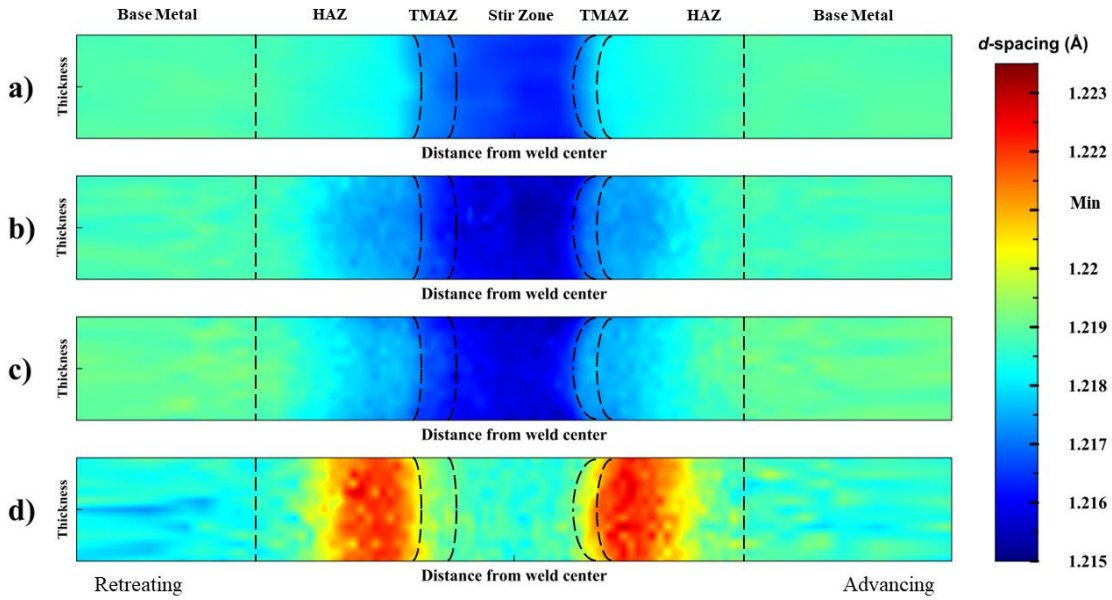

Figure A2-11 *d*-spacing contour plots for (a) d_0, (b) normal, (c) transverse, and (d) longitudinal directions

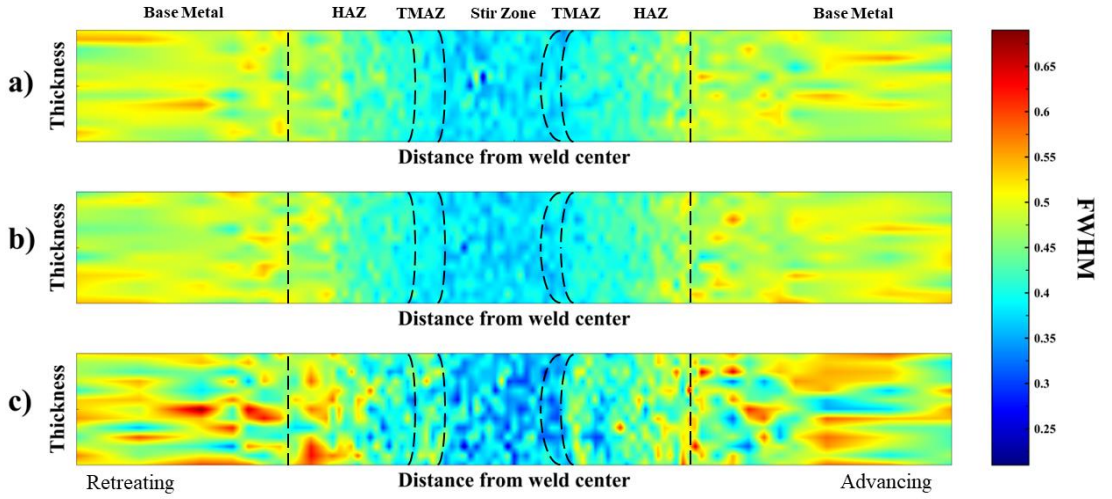

Figure A2-12 FWHM contour plots in the a) normal, b) transverse, and c) longitudinal directions

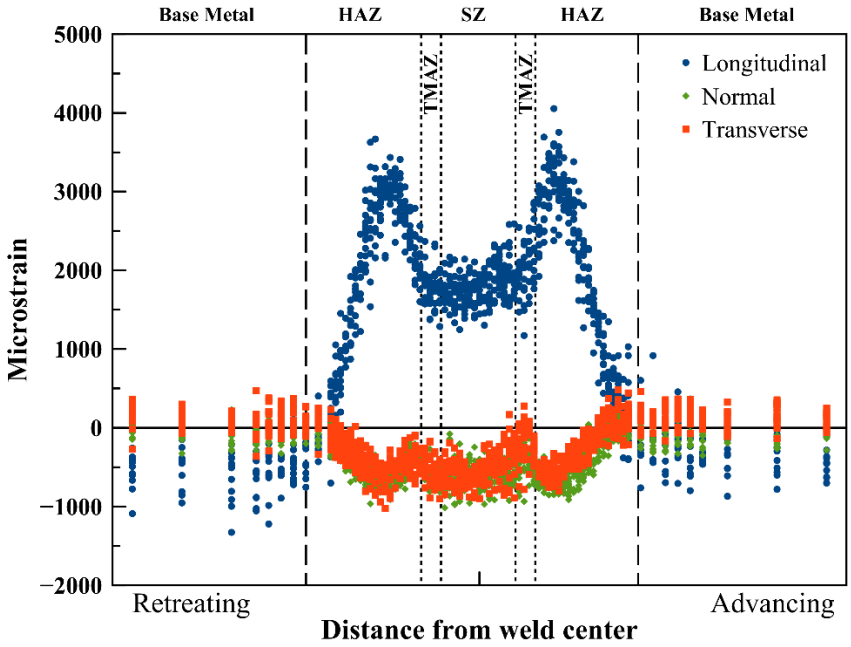

Figure A2-13 Residual strain in the normal, transverse, and longitudinal directions

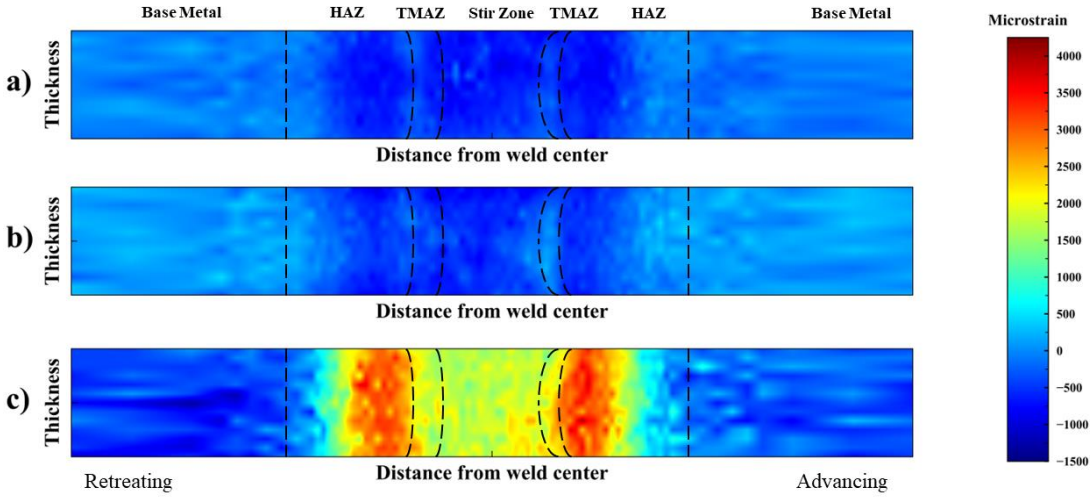

Figure A2-14 Residual strain contour plots in the (a) normal, (b) transverse, and (c) longitudinal directions

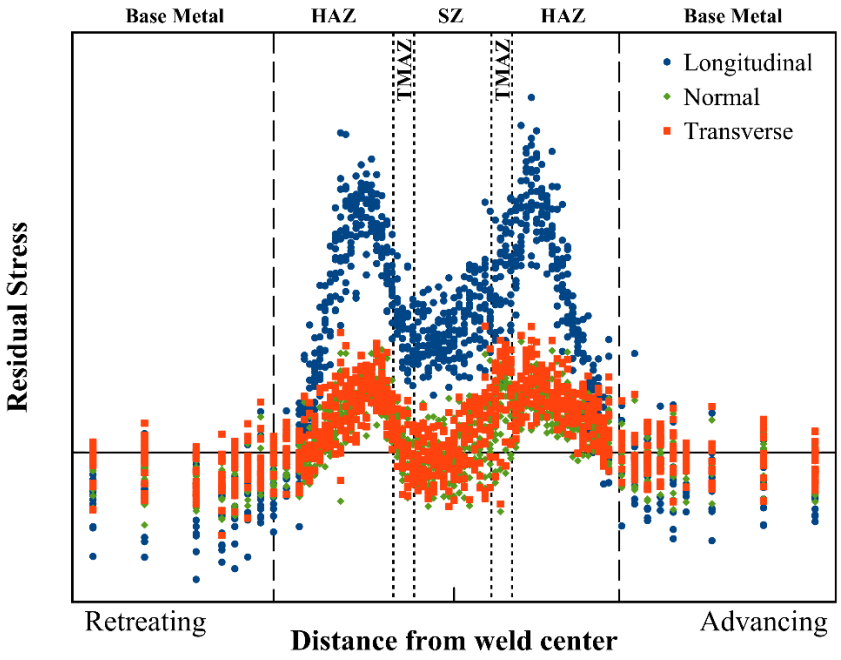

Figure A2-15 Residual stress in the normal, transverse, and longitudinal directions

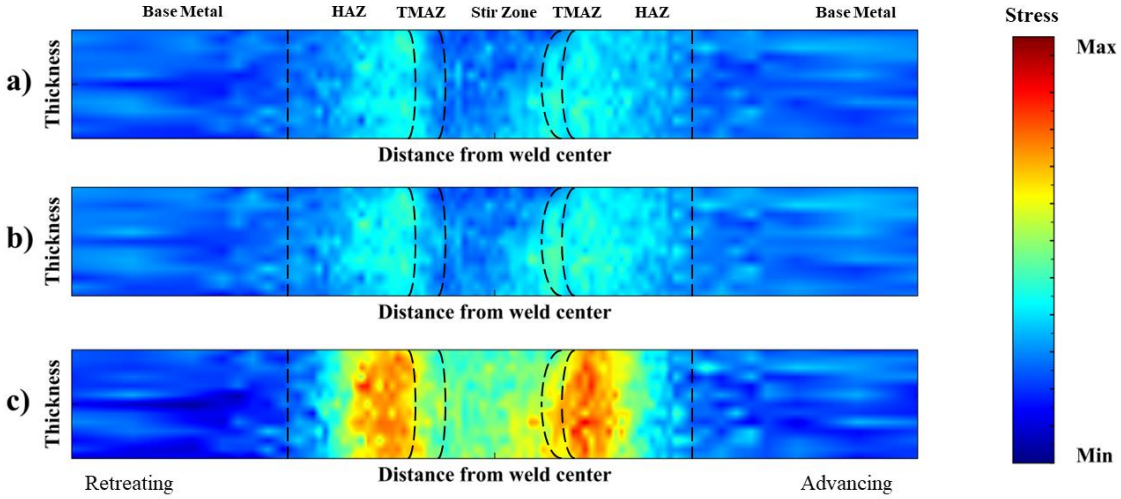

Figure A2-16 Residual stress contour plots in the (a) normal, (b) transverse, and (c) longitudinal directions

Table A2-2: Grain size comparison for 2219-T87 SRFSW

	Horizontal		Vertical	
	Measured	**Anderson**	**Measured**	**Anderson**
Base Metal	62 ± 9.7	49 ± 14.1	39 ± 6.3	26 ± 2.3
HAZ	73 ± 8.8	66 ± 6.9	73 ± 9.4	28 ± 1.6
TMAZ	15 ± 1.9	90 ± 5.6	27 ± 6.2	59 ± 7.9
Stir Zone	8 ± 1.2	8-12 ± 0.3-0.5	9 ± 1.5	8-12 ± 0.3-0.5

CHAPTER III
NEUTRON DIFFRACTION METHODS FOR RESIDUAL STRESS DETERMINATION IN WELDED ALUMINUM ALLOYS – PART II

A version of this chapter is under review for publication by Benjamin Joe Wing, Dov Polsky, Jeffrey R. Bunn, Edward A. Payzant, Fredrick N. Michael, and Claudia J. Rawn:

B.J. Wing, D. Polsky, J.R. Bunn, E.A. Payzant, C.J. Rawn, "Neutron Diffraction Methods for Residual Stress Determination in Welded Aluminum Alloys – Part II", *Journal of Materials Engineering and Performance*.

The article is presented as it was submitted, without change. Portions of the Chapter I were used in this publication. Benjamin Joe Wing and Dov Polsky completed and analyzed the metallography. Kevin Sisco performed the microhardness testing. Microhardness data was analyzed by Benjamin Joe Wing. EDS data was collected by Dov Polsky and analyzed by Benjamin Joe Wing. Neutron diffraction data was collected and analyzed by Benjamin Joe Wing, Jeffrey Bunn, Edward Payzant. Benjamin Joe Wing and Claudia Rawn wrote the paper.

3.1 Abstract

Neutron diffraction is a powerful tool for residual stress quantification of aluminum alloy welds. The superior neutron penetration for most aluminum alloys allows for complete or near-complete subsurface mapping of the residual stress state in the three principal directions (normal, transverse, and longitudinal). Such detail provides a basis for residual stress modeling efforts conducted via finite element analysis and other methods.

This paper seeks to provide a reference for the use of neutron diffraction on aluminum alloy welds for residual stress analysis. Potential sources of error related to experiment, instrument, and sample preparation are highlighted. Additional challenges posed by texture, grain size, and composition variation are discussed. Examples of mitigation and corrective actions are provided for a 2219-T87 self-reacting friction stir weld.

3.2 Introduction and Background

3.2.1 Gauge Volume

Neutron diffraction is unique in that it makes use of a gauge volume which allows, depending on the material, complete sub-surface residual stress evaluation/mapping in three dimensions. The gauge volume is a measurement volume defined by the

intersection of the incident and diffracted beam positions where the scattering vector Q (i.e. direction of measurement) is along the bisector. Gauge volume size and shape can be adjusted with the aid of slits at the incident and diffracted beam positions to those required for the measurement, **Figure A3-1**.

Orienting the sample in relation to the incident and diffracted beam path allows for the measurement of the assumed principal strain directions (transverse, normal, and longitudinal), where the scattering vector, Q, is aligned along measured direction denoted by the bolded black arrow in **Figure A3-1** and **Figure A3-2**.

The incident and diffracted beam paths can be described in terms of beam geometry in relation to a sample, represented in **Figure A3-3** for reflection and transmission geometries. Reflection geometry is typically used for the normal direction measurement while transmission geometry is typically used for the transverse and longitudinal direction measurements.

3.2.2 Determination of d-spacing, strain, and residual stress

As a material undergoes tension or compression, the interplanar or *d*-spacing changes, increasing when in tension and decreasing under compression while the scattering angle (2θ) is inversely related and varies in the opposite manner, **Figure A3-4**.

Neutron diffraction residual stress determination relies upon the principle of scattering as defined by Bragg's Law, equation 3-1, which correlates wavelength (λ), interplanar or *d*-spacing, and scattering angle (2θ).

$$\lambda = 2dsin\theta \tag{3-1}$$

This allows for the calculation of a change in *d*-spacing from change in scattering angle using a known wavelength, equation 3-2.

$$d = \frac{\lambda}{2\ sin\theta} \tag{3-2}$$

A stress-free reference *d*-spacing, known as d_0, can be used to define the measured residual strain (ε) by relating the *d*-spacing difference between the measured point (d) and its stress-free reference (d_0) divided by the stress-free reference as per equation 3-3.

$$\varepsilon = \frac{d-d_0}{d_0} \tag{3-3}$$

Strain can be measured in each direction (nine in total) to provide a comprehensive understanding of the material strain state for the triaxial state. Strain is a symmetric rank 2 tensor consisting of six shear strain components and 3 normal strain components. Rotation of this tensor to a principal strain direction (i.e. one in which all shear strains are zero) yields a simplified relation which aids further calculation, equation 3-4, where ε and γ are the normal and shear strain components, respectively. [3] The strain assumption in welds is that the weld plate's orthogonal directions – normal, transverse, and longitudinal – serve as the principal strain directions. [38]

$$\varepsilon_{ij} = \begin{bmatrix} \varepsilon_{11} & \gamma_{12} & \gamma_{13} \\ \gamma_{21} & \varepsilon_{22} & \gamma_{23} \\ \gamma_{23} & \gamma_{32} & \varepsilon_{33} \end{bmatrix} = \begin{bmatrix} \varepsilon_{11} & 0 & 0 \\ 0 & \varepsilon_{22} & 0 \\ 0 & 0 & \varepsilon_{33} \end{bmatrix} \tag{3-4}$$

Using the computed residual strain in each principal direction as in equation 3-3, the calculation of residual stress becomes possible. [32], [38] Hooke's Law, equation 3-5, is applied along with standard environment and isotropic conditions assumptions to provide the following relation, equation 3-6:

$$\sigma = E\varepsilon \tag{3-5}$$

$$\sigma_i = \frac{E}{1+\nu}\left[\varepsilon_{ii} + \left(\frac{\nu}{1-2\nu}\right)(\varepsilon_{11} + \varepsilon_{22} + \varepsilon_{33})\right] \tag{3-6}$$

where σ_i is the component of residual stress, E is the elastic (Young's) modulus, ν is Poisson's ratio, and ε_{ii} is the component of residual strain.

A thick-plate 2219-T87 self-reacting Friction Stir Weld (SRFSW) in butt weld configuration serves the basis for practical examples of this paper. Microstructure, microhardness, and neutron diffraction experiments and methods are given by Part I.

3.3 Sample Considerations

3.3.1 Composition Variation and Stress-free Reference (d_0)

The stress-free reference (d_0) allows the quantification of residual stress from a sample. Notably, this reference is not necessary for all weld measurements but is critical for

alloys which undergo chemical changes such as precipitation-hardened materials (aluminum 2xxx, 6xxx, and 7xxx). During the welding process many precipitation hardened alloys undergo dissolution due to the elevated temperature. For the case of 2219 as these precipitates solutionize, increasing amounts of copper incorporated into the solid solution ($Al_{1-x}Cu_x$ where $0<x<0.024$) thus linearly decreasing the lattice parameter in accordance with Vegard's Law. [32], [42] This leads to a decrease in *d*-spacing in the weld zones compared to the base metal resulting in a potentially larger calculated apparent tensile strain, **Figure A3-5**. Vegard's law also applies to the opposite scenario, as the precipitates coarsen/grow, the lattice parameter and thus the *d*-spacing increase.

This is illustrated by variation in measured *d*-spacing for the stress-free reference and calculated apparent strain and stress in the following example. The apparent strain and stress were determined by averaging *d*-spacing values from +/- 40-58 mm from the weld center and applying these values to equation 3-3 for strain and Hooke's Law (equation 3-4) for stress. **Figure A3-6** shows this change and how it relates to the apparent strain and stress using this method. In this instance, the maximum apparent strain was determined to be approximately -2242 microstrain with the maximum apparent stress being approximately -164 MPa.

Continued post-weld natural ageing can also impact the chemistry and therefore measurement of residual stress in a similar manner though not as significantly. Aval noted in study of 8 mm thick plate FSW AA6082-T6 and AA7075-T6 that X-ray residual stress measurements at 7 days and 365 days post weld resulted in a residual stress reduction of between 15-20 MPa for the stir zone and TMAZ. [44]

3.3.2 Sampled Location

If the selected location of the coupon or comb, for the d_0 measurement, is not the same as other measurement positions, as is often the case for neutron experiments, the effect of stress relaxation should be considered. Avoiding stress relaxation is accomplished by selecting a region which is offset approximately eight times the weld tool diameter so 90% of residual stresses are maintained. [45], [46] It has been suggested that some experiments fail to meet this guidance and residual stress values are under-reported as a

result. [14] Finally, the selected d_0 location should be at a position representative of the desired weld location (i.e. having achieved steady state conditions) – typically far from the weld onset and terminus.

3.3.3 Texture and Grain Size

In terms of neutron diffraction, large grain size (> 50 μm) and grain asymmetry can lead to inaccuracy in peak positions and thereby residual strain and stress. [30] Grain size attributable error occurs via two methods – insufficient counting statistics and asymmetric diffraction with the risk/likelihood of these errors being directly proportional to increasing grain size. Diffraction conditions are limited by the incident beam's angular divergence which results in a small angular range over which grains can diffract. Further, in a reactor-based experimental setup, only grains oriented in the chosen plane(s) will diffract when interacting with the gauge volume. In the first case, large grain size reduces the number of diffracting grains within the gauge volume which increases uncertainty in peak position for a given location. Additionally, even when large grains are oriented to diffract they may do so in an asymmetric manner (i.e. large changes in peak position with small orientation change).

Ensuring grain size related error is avoided can be accomplished in several ways. In preparation for the experiment, intensity (counts/s) should be measured at several locations and determined to be well above background (> 400 counts above) with well-defined peaks for all gauge volumes. Second, microstructural studies and grain size measurements should assist in the appropriate selection of gauge volume dimensions. For measurements of a welded structure in which texture and grain size invariably change, the gauge volume must contain enough diffracting grains for statistical significance. Typically, at least 10,000 grains are required to meet this condition so a calculation should be used to determine the expected number of grains contained within the smallest gauge volume to be used.

Additional verification can be accomplished at the instrument by performing a rocking curve measurement on the sample. In a rocking curve measurement, the detector is placed at the peak diffraction angle while the sample stage moves over θ and/or ω over a small

angular range (± 5°). Variation in the measured intensity below the square root of intensity is considered sufficient for the measurement condition. In this case either increasing the gauge volume size and/or including rotational/translational sample oscillations during measurement should mitigate the effect of large grain size.

Large grain size and significant textural evolution which can also produce an "edge effect" within the specimen. Large grain sizes result in fewer grains which meet the diffraction conditions (i.e. poor counting statistics) and increased possibility of erroneous peak-shift leading to an erroneously high compressive or tensile strain at that location. [30] One method of evaluating the presence of potential edge effects within a specimen is to interrogate normalized intensity plots (I/I_0) for each direction for large deviations from the baseline.

3.3.4 Sample Preparation

Sample preparation is crucial in residual stress measurements and in particular with sectioning/creation of the $d_{0.}$ During the 2219-T87 SRFSW experiment, it was discovered that a bandsaw was used to section the plate end instead of EDM. 2219-T87 is a heat sensitive alloy with precipitate changes occurring at temperatures as low as 50 °C for the smaller Guinier-Preston (GP) zones. [96] Within 2219-T8 FSW, the dissolution of GP zones in the thermo-mechanically affected zone (TMAZ) and stir zone (SZ) has been observed at 82 °C and 88 °C, respectively. [58] Therefore, if active cooling isn't implemented, saw cut sectioning generates significant heat which can alter the ageing state of the local material as well as surface residual stress. The effects of the bandsaw sectioning were explored in the following manner.

3.3.5 Gauge volume selection

Two separate gauge volumes were evaluated; 2 x 20 x 2 mm (80 mm^3) set at the comb center and 2 x 10 x 2 mm (40 mm^3) centered 15 mm from the plate end to provide maximal offset from the rough-cut plate terminus while remaining fully buried within the d_0 comb (**Figure A3-7**). The Si (422) monochromator (λ = 1.540 Å) setting was used to provide a scattering angle of ~78° for the Al (311). The measurement time for the smaller gauge volume was doubled to account for the decrease in measurement volume and

validated. Measurements were collected in the transverse direction on 4 mm intervals at weld mid-thickness.

The d_0 measurement was compared for the 80 mm^3 gauge volume and 40 mm^3 gauge volume measured farther from the weld plate end (**Figure A3-8**). The base metal displays roughly equivalent behavior between the two cases with the primary difference lying in the thermally affected zones: HAZ, TMAZ, and stir zone (-26 to -2 mm and 14 to 26 mm being the most notable). Within these zones the 80 mm^3 gauge volume resulted in overall higher *d*-spacing values than the 40 mm^3 gauge volume.

3.3.6 Chemical Composition

If precipitate evolution is the primary driver of *d*-spacing differences between the sampled gauge volumes, it is expected that the HAZ, TMAZ, and portions of the stir zone will display a decrease of Cu in the $Al_{1-x}Cu_x$ solid solution and an increase in *d*-spacing. If the measured composition of the aluminum matrix differs significantly from the saw cut plate end and the interior of the plate where the smaller gauge volume was placed, the validity of the correction can be established.

Sample sections were extracted by extending the d_0 comb to 80 mm from the plate end. From this section, the retreating side samples 19-22 (four 4 mm sections) were selected for interrogation due to the large difference in *d*-spacing between the small and large gauge volume, **Figure A3-s 9-10**. From this subset, three transverse sections representing conditions of interest were epoxy mounted, ground, and polished: saw cut plate end (0 mm), 40 mm^3 gauge volume midpoint (15 mm from the saw-cut end), and far interior of the plate (80 mm from plate end), **Figure A3-11**. Three energy dispersive spectroscopy (EDS) point measurements were via collected using a ThermoFisher Scientific Phenom XL Pro SEM/EDS at 15 kV accelerating voltage and 90 s collection time on the matrix at the midpoint of each of the 4 mm intervals to determine the composition difference between these conditions. **Figure A3-12** presents the atom % Cu changes for the matrix in this region for the three conditions.

For this measurement span (retreating side, samples 19-22), the matrix composition of the saw-cut condition (0 mm) displays a noticeable decrease in matrix copper concentration compared to those of the 15 mm and 80 mm positions. The decrease in matrix copper concentration for this position suggests an increase in the precipitation state of the material (i.e. precipitate nucleation and/or growth) and likely a commensurate peak shift. The matrix composition of the 80 mm and 15 mm conditions are relatively consistent, indicating little difference in matrix composition and a strong likelihood that these conditions are either marginally affected or unaffected by the heat generated from the saw-cut sectioning.

The peak shift can be estimated from experimental data on measured lattice parameter changes in the $Al_{1-x}Cu_x$ solid solution as a function of Cu concentration, equation 3-9, where $a_0(Al)$ is the aluminum lattice parameter and X_{Cu} the copper concentration (at%). [30]

$$a_0(Al) = -4.796\ x\ 10^{-3} X_{Cu} + 4.04945\ (\text{Å}) \tag{3-9}$$

The lattice parameter can then be converted to *d*-spacing for the desired *hkl*-reflection using the following relation, equation 3-10:

$$\frac{1}{{d_{hkl}}^2} = \frac{(h^2+k^2+l^2)}{a^2} \tag{3-10}$$

where *d* is *d*-spacing (Å), *hkl* are the Miller indices, and *a* is the lattice parameter (Å). [124] The calculated lattice parameter and *d*-spacing is plotted against the matrix composition and sample number, **Figure A3-13**.

The calculated *d*-spacing values can then be used to calculate strain, equation 3-3, and stress difference, equation 3-4, where the calculated *d*-spacing at 80 mm is taken as the d_0; E = 73.1 GPa and n = 0.33. Calculated microstrain and stress difference are plotted against matrix composition and sample number, **Figure A3-14**, using the various strain calculations which are denoted as $\varepsilon_{x\text{-}y}$ where x is the interrogated position and y is the referenced (i.e. d_0) composition.

Microstrain and stress difference plots demonstrate the relatively small difference between the 80 mm and 15 mm positions (~200 microstrain and 20 MPa at most) across the measurement span. The change in chemistry from 15 mm to 80 mm from the plate end is considered minimal and a good mitigating effort.

Small/Large Gauge volume

Similarly, microstrain and stress differences between the 40 mm^3 gauge volume and 80 mm^3 gauge volume measurement conditions are made using the same conditions but with d_0 assigned as the measured *d*-spacing of the 40 mm^3 gauge volume. **Figure A3-15** provides these plots over the weld space where the dashed line region is the EDS measurement space (sample number 19-22).

Microstrain and stress difference plots between the 80 mm^3 and 40 mm^3 gauge volume measurement conditions show differences of between -139.8 to 474.6 microstrain equating to stress differences ranging from -10.2 to 34.69 MPa. These differences are greatest near the crown and root of the weld and minimize toward the midline. Evaluation of *d*-spacing difference between the gauge volumes was completed via comparing values across the midline from the HAZ to SZ of the retreating and advancing sides. However, seemingly increasing microstrain and stress differences toward the weld center, near the crown and root of the plate, suggest this span may not be sufficient to account for all differences between these gauge volumes.

Force Balance

The effect the global shift has upon residual stress is presented in **Figure A3-16** and summarized in **Table A3-1**.

The constant global *d*-spacing shift produced from the force balance was 1.332 $x10^{-4}$ Å which aligns with the 1 $x10^{-4}$ Å average *d*-spacing difference (Δd) between the 80 and 15 mm positions, **Figure A3-17**, and equates to an average residual stress decrease of ~23.5 MPa.

The force balance approach was employed in such a way as to overestimate the correction factor (or error) due to assumptions and simplifications related to residual stress dynamics and extrapolation methods. As distance from the weld increases, residual

stresses for all orthogonal directions trend toward zero. [14], [32], [33], [38] However, in setting up the force balance a constant extrapolation method was used to forecast the *d*-spacing to the plate edge in the x-direction direction. This extrapolation does not allow for transient spikes in residual stress within the base metal section nor for residual stress to approach zero (*d*-spacing convergence) in any of the orthogonal directions as the position approaches the plate edge. This leads to an overestimation of area of tensile and compressive residual stresses beyond the measured region(s) and a larger *d*-spacing shift.

Figure A3-18 illustrates the difference between a typical longitudinal residual stress distribution where stress approaches zero and the constant extrapolation method implemented. Only the longitudinal residual stress is displayed here to display the concept.

Discussion and Conclusion

The saw-cut sectioning method has a substantial effect upon measured residual strain and stress. The 0 mm position showed a stress difference of -44.5 MPa to -20 MPa and 16.5 to 30 MPa compared to the 15 mm and 80 mm positions, respectively. Failure to account for this chemistry change results in greater apparent tensile residual stresses in the heat affected zones (HAZ, TMAZ, and presumably SZ). The need to use the 40 mm^3 gauge volume is thereby validated as is the need to employ a force/moment balance approach to further account for these deviations. More generally, this difference also highlights the need to use a heat-free sectioning method when cutting Al 2xxx series alloys.

The effect of the saw-cut is inconsistent across the weld and supports the conclusion that different regions are more/less susceptible to chemistry changes due to added heat. Supporting this are findings that the base metal condition shows a minimal variation in both matrix composition at various depths and the measured *d*-spacing for 80 mm^3 and 40 mm^3 gauge volumes compared the HAZ section. As the samples examined with EDS are from within the most affected region, where the Cu matrix composition is lower, the *d*-spacing shift required will be overestimated if applied as a constant value across the weld instead of by examining and interrogating each measurement position across the weld.

These calculations hinge on the assumption of a pure Al-Cu binary solution which is in truth somewhat simplified. This method is likely insufficient for precision determination of the lattice parameter and subsequent *d*-spacing shifts owing to the contribution of other alloying elements (e.g. Fe, Mn, Si, Zr, etc.) in 2219 and differences in local stress and texture. [32] However, these contributions are considered minimal as minor alloying elements were not detected during the EDS analysis and comprise only a small portion of the alloy and the EDS error far outweighs this factor. Other potential factors such as sample anisotropy, texture evolution, and intergranular residual stress may contribute to differences in determined *d*-spacing. These calculations can thus be considered sufficient only for the purposes of obtaining qualitative and semi-quantitative results which can be employed toward establishment of a non-definitive correction factor. The results of these measurements and proceeding calculations are summarized in **Table A3-2**.

3.4 Measurement Considerations

3.4.1 Characteristic Peak

A characteristic peak is defined as not readily affected by intergranular strain and shows strain linearity under at least uniaxial loading conditions. This is essential as certain planes can be significantly affected by texture (as well as loading and plastic deformation) leading to inaccurate strain and stress determinations. For aluminum alloys, the (311), (422), and (220) planes are recommended for residual stress experiments while the (200) plane is strong affected by intergranular strains and avoided. A summary of the Versailles Project on Advanced Materials and Standards (VAMAS) standard for characteristic peak selection is provided in **Table A3-3**. [39]

3.4.2 Partially Buried Gauge Volume

Beam geometry can have importance consequences for neutron diffraction experiments particularly when a portion of the gauge volume lies outside the sample - a condition known as a partially buried gauge volume. In an experiment quantifying the effects of partially buried gauge volumes on the Ni (311) reflection of a stress-free nickel specimen, Wang et al. noted that while the transmission geometry displayed little to no peak shift "until the specimen was almost completely out of the sampling volume". However, the

reflection geometry was affected by even a slight partial burial of the gauge volume, **Figure A3-19**. [40] This peak shift leads to a skewed *d*-spacing, correspondingly incorrect strain/stress, and erroneous results.

Another ramification of the study by Wang et al. was tested. It was hypothesized that small but relatively insignificant changes would result from the gauge volume placement on the EDM cuts in the transmission geometry. Testing of the significance of a partially buried gauge volume in the measurement of the d_0 *d*-spacing was conducted in the transverse direction with 1 mm intervals from +/- 30 mm, 5 mm intervals from +/- 30-50 mm, and 10 mm intervals from +/- 50-70 mm measured at weld mid-thickness with a gauge volume of 40 mm^3. This was compared to fully buried gauge volume measurements taken at 4 mm intervals (**Figure A3-20**).

Observations from **Figure A3-20** support the hypothesis and aligned with Wang et al's findings. [40] Although a higher degree of error was noted (in part due to decreased sampling time of the "dense" measurement) along with an erroneous point at -21 mm, the assumption appears to hold. This conclusion offers several advantages to the experiment such as reasonably accurate determination of the *d*-spacing at positions in which the gauge volume is partially buried, a reference for interpolation of *d*-spacing measurements, and potentially complete mapping of the d_0 *d*-spacing at all measured positions. Such sampling would only be possible for directions using the transmission geometry (transverse and longitudinal).

3.4.3 Location Selection

The selection of a measurement location and d_0 offset is an important factor for consideration in an experiment. The measurement location should be at a representative position at the desired location (often steady state conditions) – typically far from the weld onset and terminus. If the selected location of the coupon or comb, for the d_0 measurement, is not the same as other measurement positions, as is the case for most neutron experiments, the effect of stress relaxation should be considered. Avoiding stress relaxation is accomplished by selecting a region which is offset approximately eight times the weld tool diameter so 90% of residual stresses are maintained. [45], [46] It has

been suggested that some experiments fail to meet this guidance and residual stress values are under-reported. [14]

In addition, the d_0 measurement offset should be considered as the stress state can vary significantly along the traverse direction even with consistent welds. This is demonstrated by the following example for 2219-T87 SRFSW.

Transverse direction data were collected at +75, +150, and +243 mm (~65 mm from weld start) from the original measurement position while normal direction data was taken at +243 mm (65 mm from weld start) (**Figure A3-21**). For these measurements, a Si (422) monochromator (λ = 1.540 Å) was selected, providing a scattering angle of ~78° for the Al (311) and a rectangular gauge volume, 2 x 20 x 2 mm, was used.

Figure A3-22 compares the original transverse measurement with others along the weld line while **Figure A3-23** compares the original normal measurement with one taken at the weld start (+243 mm). Error bars are omitted for visualization purposes as they obscure trends.

The +75 mm transverse direction *d*-spacing measurement aligns well with the selected measurement plane for this experiment. Strain profiles for measurements at +150 mm and +243 mm show small but increasing deviations from the selected measurement plane, most apparent from the advancing to retreating side HAZ. The small plateaus/shoulders of the original measurement positions gradually decay and take on a smoothed and more prominent ‘V-shape’.

While estimation of residual stress using a simplified Hooke’s law ($\sigma=E\varepsilon$) is possible, the resultant values must be carefully considered. The values taken away from the original measurement position do not have the context (i.e. other orthogonal direction and d_0 values) necessary to make this determination. In this setting residual stress estimates (based on *d*-spacing differences) are most appropriate for evaluation of potential errors due to location offset between the measurement and d_0 planes. Contour plots showing the approximate microstrain and stress difference between the original measurement position and the additional transverse direction measurements are presented in **Figure A3-24**.

Stress differences in the transverse direction range from -37.3 to 94.2 (Δ 131.5) MPa and from -69.8 to 59.8 MPa (Δ 129.6) in the normal direction compared to the original measurement position. For the transverse direction the minimal values are relatively stable with an 8.57 MPa standard deviation and with maximal values showing more variability (18.12 MPa standard deviation). For the transverse direction, the stress difference range between the +75 mm and original measurement positions was between -37.3 and 57.9 MPa but only -14.1 and 28.3 MPa (±6.97 MPa) when comparing the +75 and +150 mm measurement positions. The latter indicating good consistency between measurements.

Of the potential conclusions that arise from this data the most basic interpretation indicates a higher tensile residual stress compared to the original measurement position. This could be at least partially valid as studies have shown a general increase in residual stress along the weld traverse. [14], [121] Although, if these values were simply added to existing residual stress determinations the maximal values would far exceed the yield stress. A more nuanced alternative is a combination of increasing stress values and acknowledgement that the d_0 values likely differ from the original measurement position. Although, without location specific d_0 measurements this cannot be definitively stated and an estimate or expected range cannot be identified.

These differences may indicate additional uncertainty in residual stress determination due to the d_0 selection position being 135 mm from those of the orthogonal measurement planes. The +75 and +150 mm positions are similar and suggest variation in the d_0 would be low for a similar offset distance, potentially leading to improved accuracy of residual stress measurements. Ideally, the d_0 measurement would take place at the same location as the orthogonal measurements, however, due to requirements of other experiments a -135 mm offset was chosen.

3.4.4 d_0 Interpolation

Sectioning disallows d_0 value determination at each measured point and due to chemical change being present, direct correlation will lead to an apparent strain/stress especially in regions of transition or rapid change. Therefore, adequate representation of variation in

the reference *d*-spacing at all measured positions often requires interpolation between d_0 values.

The selected interpolation scheme should most accurately reflect or approximate the trend in d_0 and consider both axes of the two-dimensional data. Manual calculation of the interpolated values in two-dimensions may prove tedious so functions such as SciPy's *interpolate.griddata* can be used to interpolate the non-uniform rectangular d_0 data grid for the piecewise linear and cubic spline cases. [125] **Figure A3-25** compares d_0 values and linear and cubic interpolation results for a 2219-T87 SRFSW.

Overall, there is little difference between these methods for most locations. As expected, notable exceptions to this are observed in transition regions and the stir zone. Cubic interpolation provides a polynomial fit and transitions zones are smoother than the linear interpolation though this leads to lower *d*-spacing from on the advancing side SZ and higher *d*-spacing on the retreating side SZ. The transition region near the TMAZ also has a higher *d*-spacing for the cubic interpolation.

These schemes were compared to the variable interval midthickness d_0 measurements (measured across the sections), **Figure A3-26**. From this, it was determined the linear interpolation more accurately represents *d*-spacing changes than the cubic scheme.

3.5 Conclusion

Neutron diffraction is a powerful tool for the subsurface evaluation of residual strain and stress in aluminum alloy welds. However, careful consideration should be made when conducting residual stress experiments on precipitation hardenable aluminum alloys. Considerations for neutron diffraction residual stress experiments were discussed notably making use of transmission geometry to measure transverse direction d_0 in a dense scheme and a method for correction of a bandsaw altered chemistry. General recommendations for residual stress neutron experiments in precipitation hardened aluminum alloys are provided.

Gauge volume selection should account for grain size and microstructure variation and be validated via peak intensity above background and/or use of a rocking curve. For many aluminum alloys 2-3 mm cubic gauge volumes have been deemed appropriate.

Accounting for compositional and texture changes requires careful selection of a stress-free reference (d_0) in terms of both location and sectioning method. For optimal accuracy the d_0 location will be the same as the measurement plane, however, in most cases this is not possible, and an offset must be used. In the case of FSW avoiding stress relaxation related to d_0 construction is accomplished by selecting a region which is offset approximately eight times the weld tool diameter so 90% of residual stresses are maintained. [45], [46] As demonstrated in this work, the sectioning method can also impose an effect upon apparent residual strain/stress. In sectioning EDM is preferred as saw cut sectioning can introduce both surface residual stress and, for highly heat sensitive materials, a composition change.

Finally, transmission geometry measurements can be leveraged to measure across the d_0 cuts/sections and avoid interpolation. If interpolation is necessary for evaluation as may be the case for the reflection geometry a simple linear interpolation is suggested.

3.6 Acknowledgements

The authors would like to acknowledge partial support though the Manufacturing and Materials Joining Innovation Center (Ma^2JIC) University of Tennessee, Knoxville site. Ma^2JIC is funded by the National Science Foundation (NSF) through the Industry/University Cooperative Research Center (I/UCRC) program award number IIP 1822186. This research used resources at the High Flux Isotope Reactor a DOE Office of Science User Facility operated by the Oak Ridge National Laboratory.

Appendix

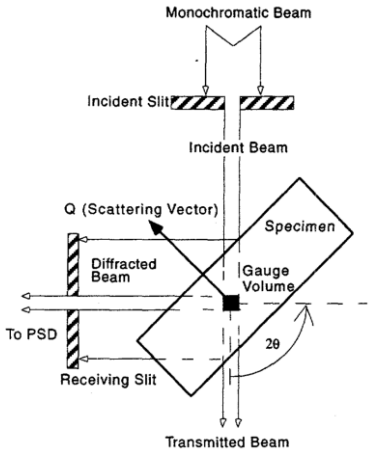

Figure A3-1 Schematic of reactor-based instrument optics (PSD is position-sensitive detector) [41]

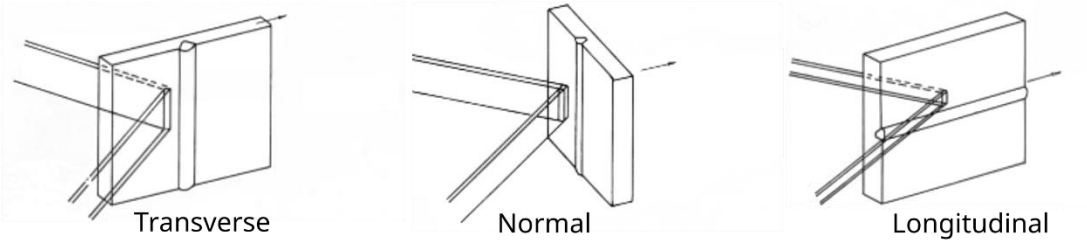

Figure A3-2 Schematic of gauge and scattering volumes for the transverse, normal, and longitudinal directions

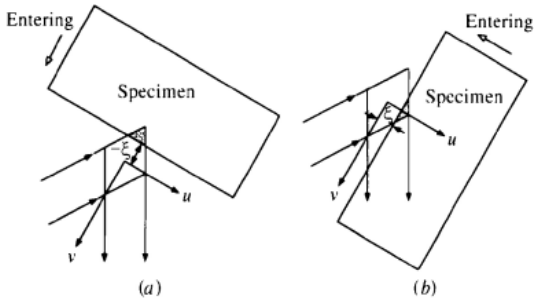

Figure A3-3 (a) reflection geometry and (b) transmission geometry [40]

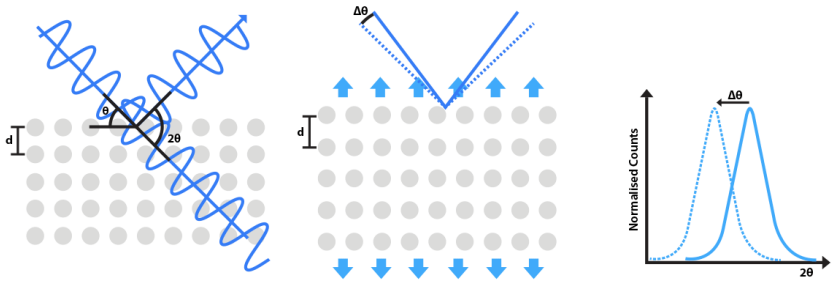

Figure A3-4 Illustration of incident and diffracted beam related to scattering angle change [37]

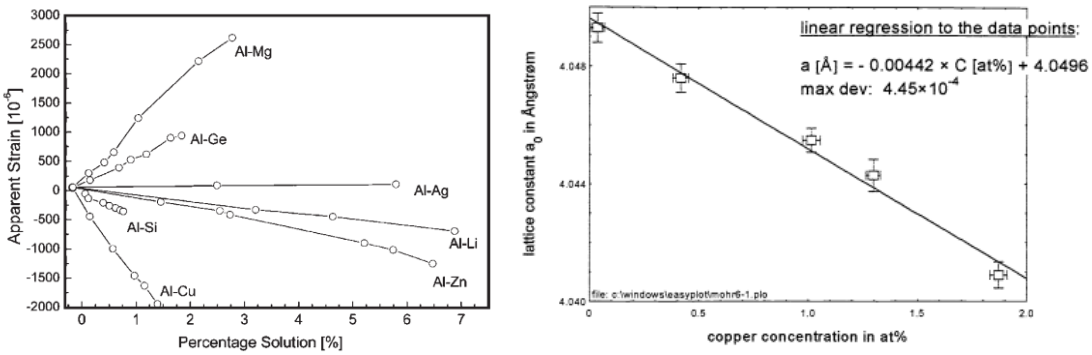

Figure A3-5 Apparent microstrain vs composition [32] (left) lattice constant vs copper concentration in for the $Al_{1-x}Cu_x$ solid solution [43] (right)

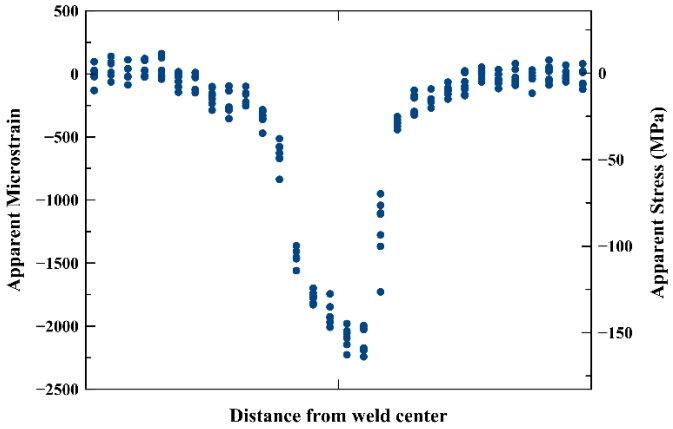

Figure A3-6 Apparent microstrain and stress due to chemical and microstructural changes



Figure A3-7: Positioning of original 2 x 20 x 2 mm (blue) and 2 x 10 x 2 mm (orange) gauge volumes

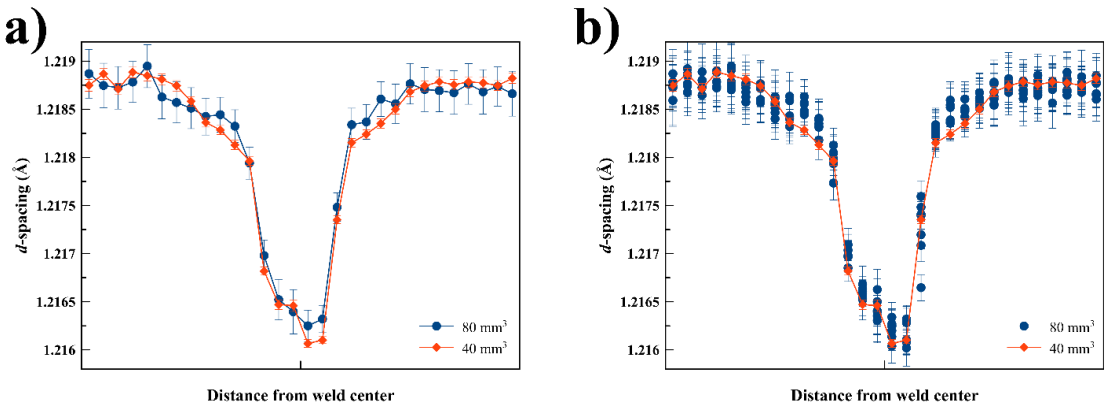

Figure A3-8: Transverse direction *d*-spacing measurement for the 80 mm^3 (2 x 20 x 2 mm) and the 40 mm^3 (2 x 10 x 2 mm) gauge volumes at (a) mid-thickness and (b) all thicknesses

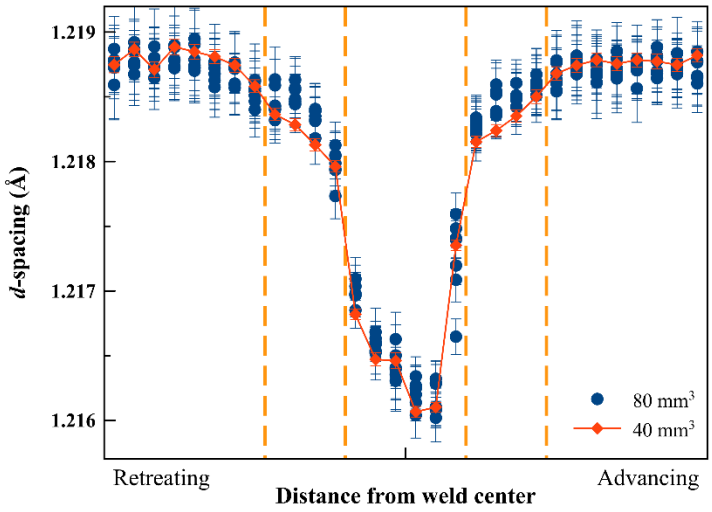

Figure A3-9: 80 mm^3 and 40 mm^3 gauge volume *d*-spacing highlighting regions of difference (orange dashed lines) on the advancing and retreating sides

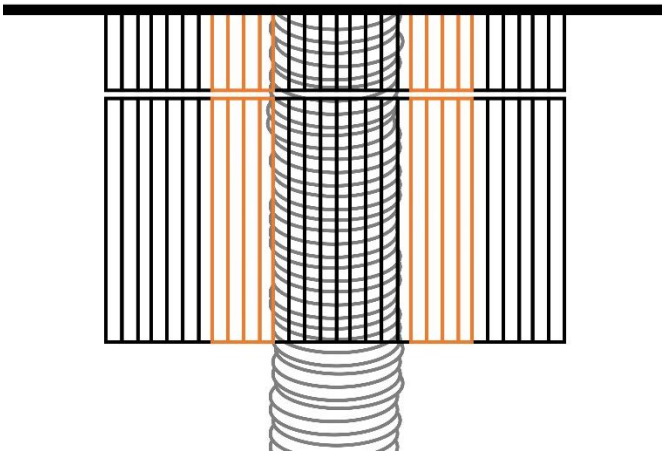

Figure A3-10: Regions of interest for EDS measurement highlighted in orange

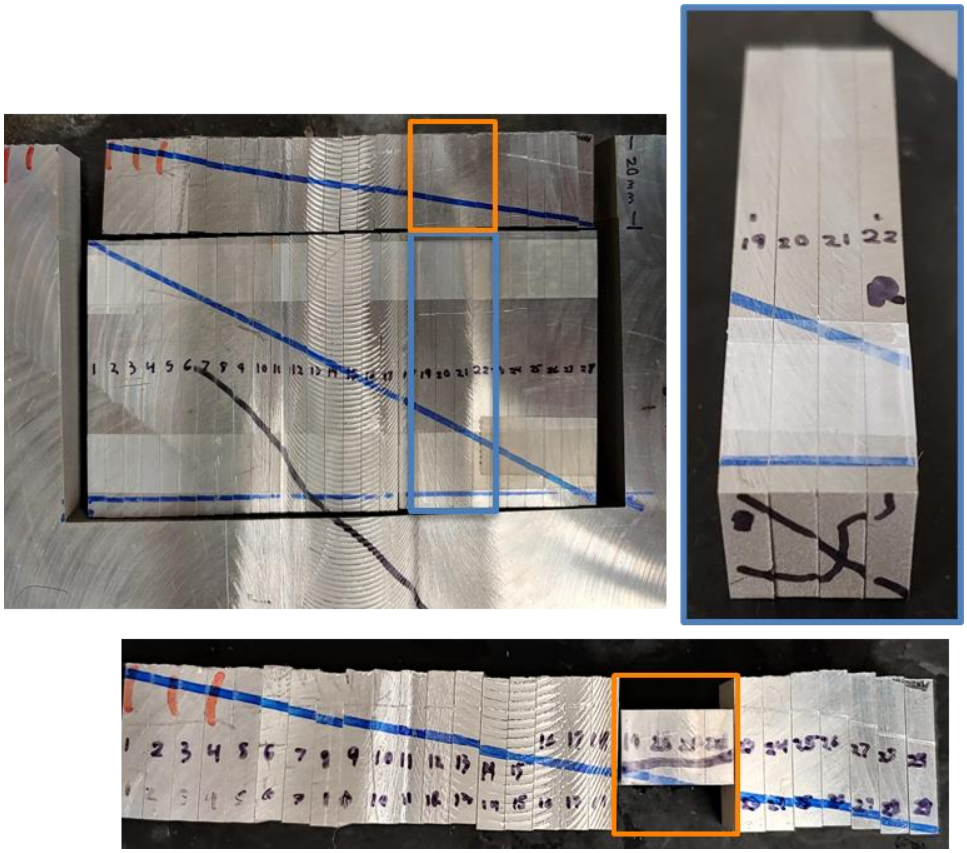

Figure A3-11: Selected sample locations for EDS measurement highlighted in orange and blue

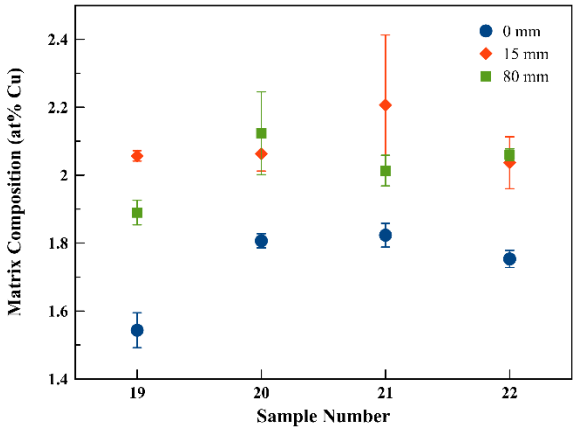

Figure A3-12: Composition (at% Cu) of the matrix for 0 mm (saw cut), 15 mm, and 80 mm locations from plate end (error bars are 1σ)

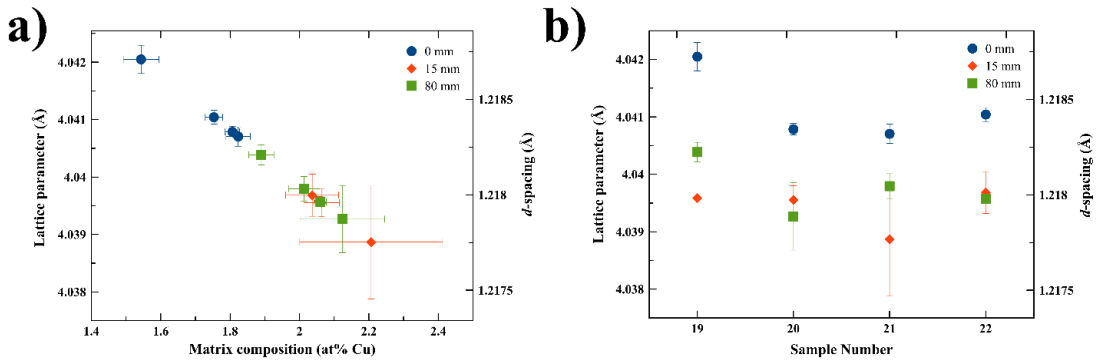

Figure A3-13: Calculated lattice parameter (left y-axis) and *d*-spacing (right y-axis) vs (a) Composition (at% Cu) and (b) sample number

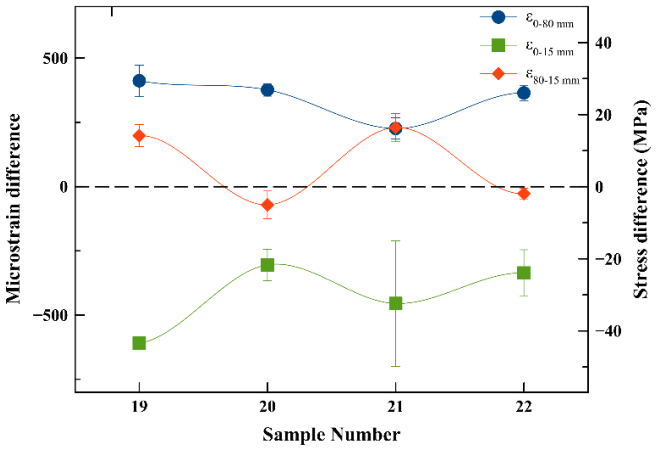

Figure A3-14: Calculated microstrain (left axis) and stress difference (right axis) vs sample number

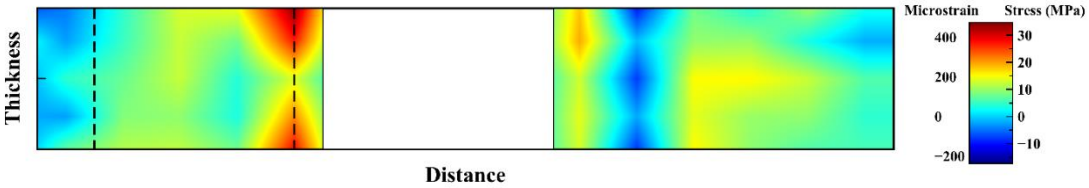

Figure A3-15: Calculated microstrain and stress difference (MPa) contour plots for the 80 mm^3 and 40 mm^3 gauge volume measurement conditions across the weld. EDS measurement region is denoted by the dashed lines

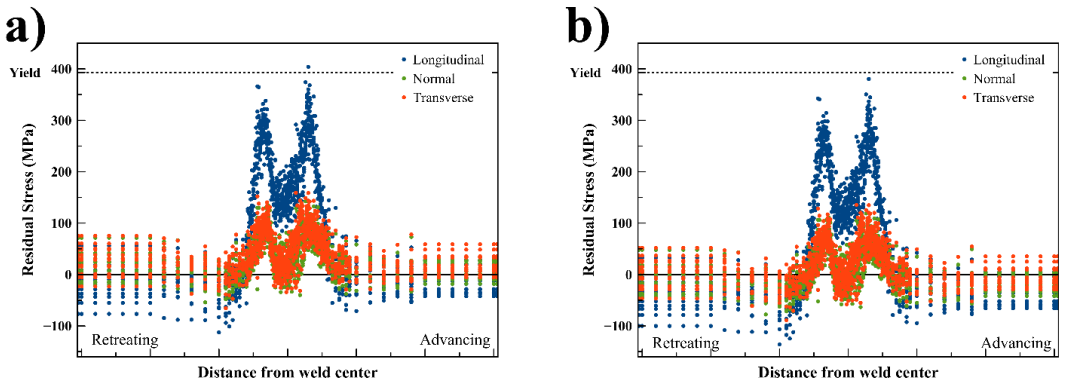

Figure A3-16: Residual stress comparison (a) with and (b) without application of force balance

Table A3-1: Residual stress difference (maximum and minimum values) after force balance application

	Maximum (MPa)	Minimum (MPa)
Longitudinal	23.55	-23.48
Normal	23.52	-23.48
Transverse	23.56	-23.48

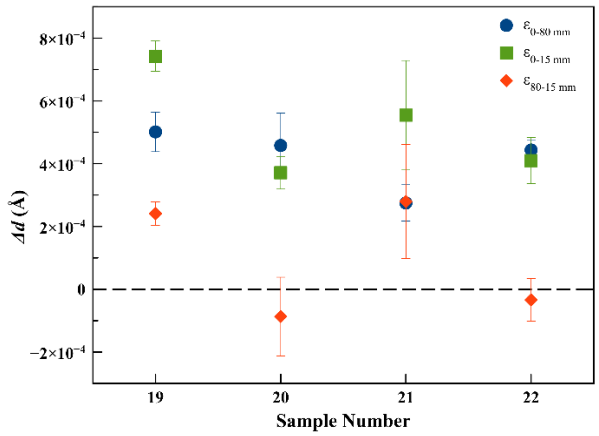

Figure A3-17 Δ*d* between EDS measurement locations

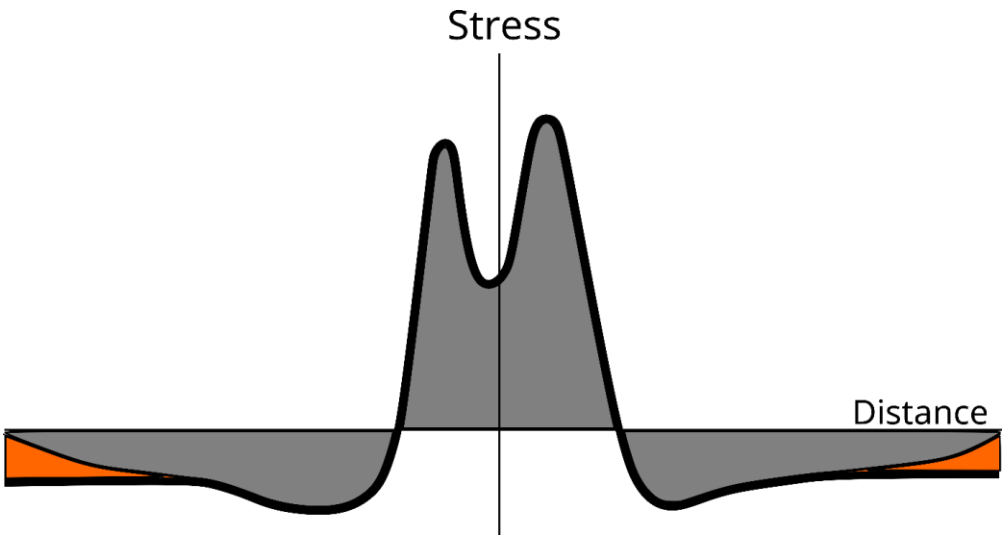

Figure A3-18 Difference between a typical longitudinal residual stress trend (grey) and constant extrapolation (orange)

Table A3-2: Copper concentration (at%), a_0 (Å), *d*-spacing (Å), microstrain difference, and stress difference (MPa)

	Sample #	19	20	21	22
Average Cu (at%)	**0 mm**	1.54	1.81	1.82	1.75
	15 mm	2.06	2.06	2.21	2.04
	80 mm	1.89	2.12	2.01	2.06
a_0 (Å)	**0 mm**	4.04205	4.04079	4.04071	4.04104
	15 mm	4.03959	4.03955	4.03887	4.03968
	80 mm	4.04039	4.03927	4.03979	4.03957
***d*-spacing (Å)**	**0 mm**	1.21872	1.21834	1.21832	1.21842
	15 mm	1.21798	1.21797	1.21776	1.21801
	80 mm	1.21822	1.21788	1.21804	1.21798
Microstrain difference	**0 mm - 80 mm**	411.50	375.99	225.57	364.09
	0 mm - 15 mm	-609.46	-304.73	-455.19	-336.38
	15 mm - 80 mm	197.84	-71.24	229.52	-27.70
Stress difference (MPa)	**0 mm - 80 mm**	30.08	27.49	16.49	26.62
	0 mm - 15 mm	-44.55	-22.28	-33.27	-24.59
	15 mm - 80 mm	14.46	-5.21	16.78	-2.03

Table A3-3: Lattice planes and intergranular strain response *adapted from* [32]

Material	Recommended Planes (Weakly Affected by Intergranular Strains)	Problematic Planes (Strongly Affected by Intergranular Strains)
FCC (Ni, Fe, Cu)	(111), (311), (422)	(200)
FCC (Al)	(311), (422), (220)	(200)
BCC (Fe)	(110), (211)	(200)

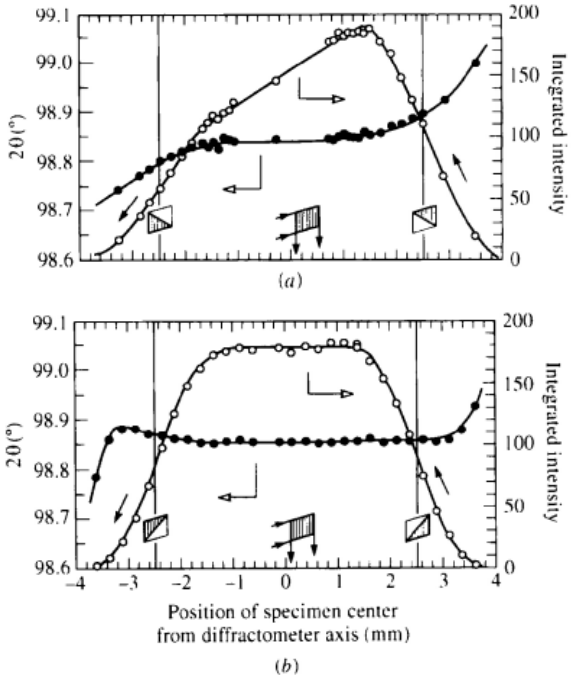

Figure A3-19 *2θ* (311) reflection Ni (a) reflection geometry (b) transmission geometry [40]

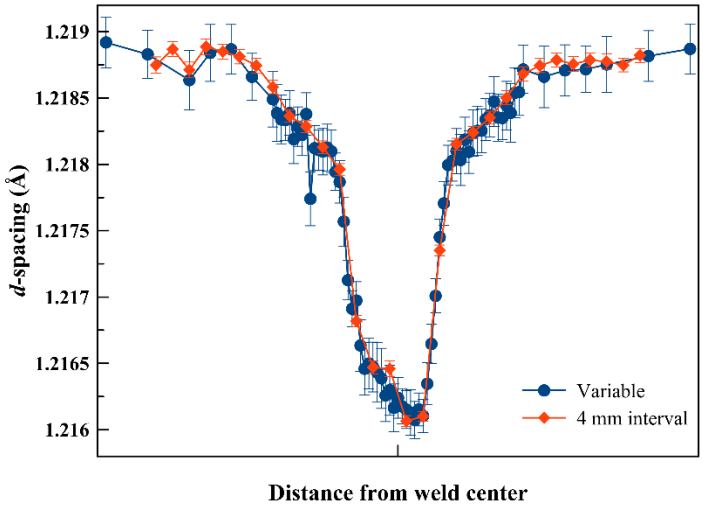

Figure A3-20 Transverse direction *d*-spacing measurements for 4mm interval and variable measurement schemes

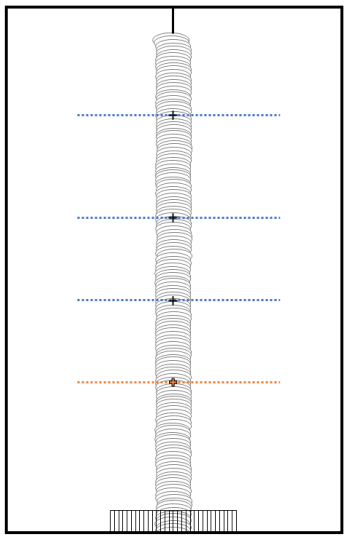

Figure A3-21 Approximate location of measurement planes; initial measurement (orange), repeatability measurements (blue)

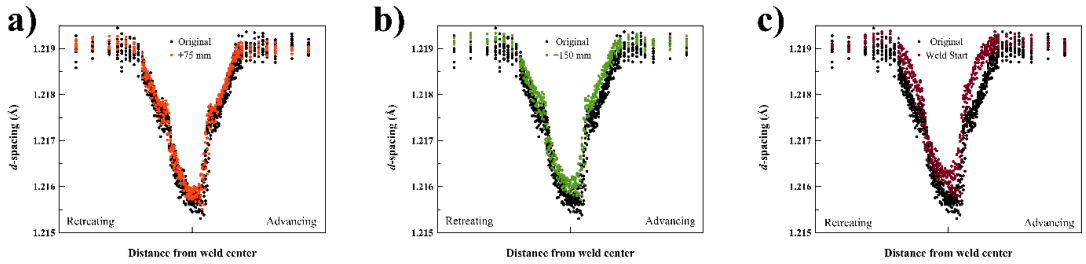

Figure A3-22 *d*-spacing of transverse direction measurements at (a) +75 mm, (b) +150 mm, (c) +243 mm compared to original measurement position

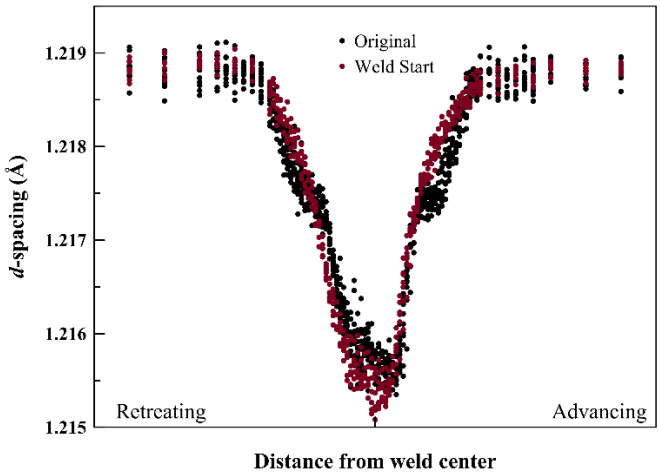

Figure A3-23 *d*-spacing of normal direction measurements at +243 mm compared to original measurement position

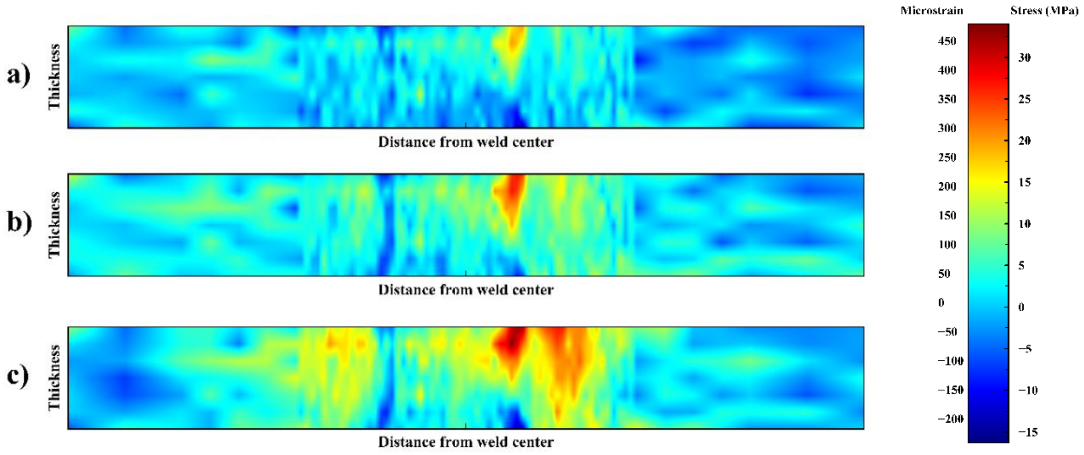

Figure A3-24 Microstrain and stress difference between transverse direction measurements at (a) +75 mm, (b) +150 mm, (c) +243 mm and the original measurement position

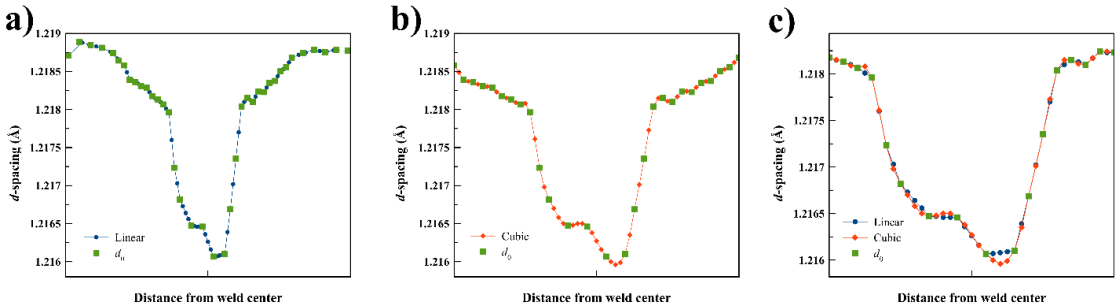

Figure A3-25 Mid-thickness d_0 measurements with (a) linear, (b) cubic interpolation, (c) both – enlarged to display trends

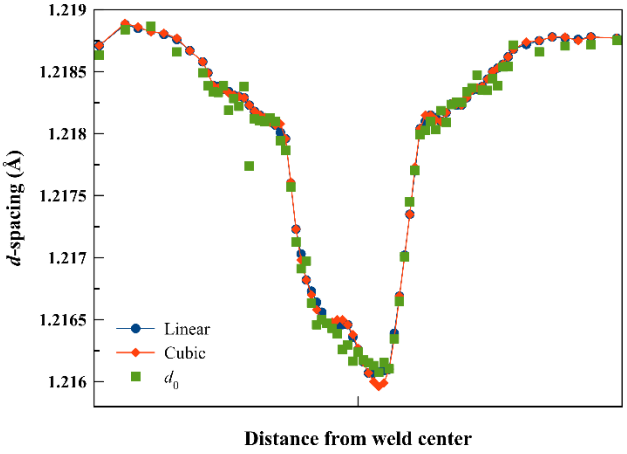

Figure A3-26 Mid-thickness variable d_0 measurements with linear and cubic interpolation

CHAPTER IV
RESIDUAL STRESS STUDY OF DISSIMILAR AA2219/AA2195 SELF-REACTING FRICTION STIR WELDS WITH NEUTRON DIFFRACTION

A version of this chapter was submitted to The Welding Journal for publication by Benjamin Joe Wing, Dov Polsky, Edward A. Payzant, Jeffrey R. Bunn, Fredrick N. Michael, and Claudia J. Rawn:

B.J. Wing, D. Polsky, E.A. Payzant, J.R. Bunn, C.J. Rawn, "Residual Stress Study of a Dissimilar AA2195-T88/AA2219-T87 Self-Reacting Friction Stir Weld with Neutron Diffraction", *The Welding Journal*.

The article is presented with the addition of residual stress analysis of another dissimilar SRFSW (AA2195-T8M4/AA2219-T851). Portions of the Chapter I were used in this publication. Benjamin Joe Wing and Dov Polsky completed and analyzed the metallography. Kevin Sisco performed the microhardness testing. Microhardness data was analyzed by Benjamin Joe Wing. Neutron diffraction data was collected and analyzed by Benjamin Joe Wing, Jeffrey Bunn, Edward Payzant. Benjamin Joe Wing and Claudia Rawn wrote the paper.

4.1 Abstract

Self-reacting Friction Stir Welding (SRFSW) is primarily employed for components too thick for conventional FSW or components that cannot be joined with use of a backing plate, e.g. those with cylindrical geometries. In construction of complex structures it is sometimes necessary to join dissimilar alloys at transition regions such as in NASA's external tank. [126] The joining of dissimilar materials is more complex than for similar-similar metal welds and requires careful control of processing parameters to achieve a strong, stable weld. This is especially true for precipitation hardenable alloys such as aluminum 2219 (Al-Cu) and 2195 (Al-Cu-Li) which despite the lower heat input of SRFSW compared to its fusion counterparts, still leads to coarsening, loss of strengthening precipitates, and large residual stresses.

Neutron diffraction was used to determine residual strain and stress in the normal, transverse, and longitudinal directions for two dissimilar SRFSWs: 2195-T88/2219-T87 and 2195-T8M4/2219-T851. Prior to these measurements metallography and microhardness testing was carried out. Weck's color etchant was used to discriminate

macrostructure and microstructure. Macrostructurally, an ‘hourglass’ pattern was observed without weld deformity or defects. The alloy transition was abrupt with little apparent interdiffusion. Grains coarsened in the heat-affected zone (HAZ), elongated in the thermo-mechanically affected zone (TMAZ), and became fine and equiaxed in the stir zone (SZ). Microhardness of the transverse weld cross-section allowed for identification of key weld zones/features and aligned well with observed microstructural zones. Microhardness profiles followed a ‘W-shaped’ pattern with maximal microhardness in the base metal (BM) and minimum microhardness in the TMAZ with slight recovery in the SZ.

Longitudinal residual stress took on an ‘M-shaped’ profile with highest tensile values on the retreating side (2195) just outside the TMAZ with greatest compressive stresses being present in the BM. The normal and transverse residual stress profiles took on a similar shape but at lower magnitude in the case of 2195-T88/2219-T87 and a hump shaped appearance for 2195-T8M4/2219-T851. Potential issues were observed in both welds with the 2195-T88/2219-T87 SRFSW displaying characteristic signs of an “edge effect” at strong texture transitions and 2195-T8M4/2219-T851 suffering from post-weld sectioning resulting in possible stress relaxation. Ultimately, these results (magnitude and profile) are reasonable and can assist in qualitative evaluation of the weld.

4.2 Introduction

2xxx series aluminums are age hardenable alloys which possess high strength and ductility, low density, good corrosion resistance, and stable cryogenic performance. [1] Their high strength-to-weight ratio and cryogenic stability make them ideal candidates in many structural aerospace applications such as the liquid propellant rocket fuel tanks on NASA’s Space Launch System (SLS). However, joining these materials poses additional engineering challenges. First, several alloys in the 2xxx series (such as 2195) have poor weldability with traditional fusion based weld processes – producing compromising defects such as solidification cracks and voids. [14], [106] Second, the circumferential nature necessitates an opposing or stabilizing/reactionary force to avoid warpage and maintain weld consistency. Finally, the joining of dissimilar alloys is often required at

transition regions and these materials can have significantly different properties which make joining difficult. [126] Each issue is mitigated with the use of a solid-state welding processes known as self-reacting friction stir welding (SRFSW). In SRFSW, a rotary tool consisting of two shoulders connected via a through thickness pin travels along adjacent or overlapping plates and mixes the material. The frictional heat generated by the rotary tool softens the material which is then stirred via the shear action of the pin. With careful selection of processing parameters, this results in exceptionally repeatable, defect free bonds as required for such critical applications.

This process greatly improves upon traditional fusion based processes and may reduce the effects of residual stress and joint softening (i.e. loss of mechanical properties). [14], [17] However, the frictional heat as well as the high shear and restraint conditions of SRFSW still result in a significant residual stress as well as coarsening and solvation of strengthening precipitates, each to the detriment of the mechanical properties of the assembly. [2], [3]

Residual stress, or stress present in a material without an acting external force, is due to misfits between regions within a material - primarily differences in the thermomechanical deformation for SRFSW. Residual stresses can be large (approaching the material's yield stress) and lead to premature failure and lower material performance. [38] As such, understanding of the residual stress state in critical components is of high importance. These stresses have been evaluated for dissimilar joining of thick-plate aluminum 7050/2024 FSW, 7181-T7651/7475-T7351 SRFSW, and 6082-T6/7075-T6 FSW among others each observing an 'M-shaped' longitudinal residual stress profile. [46], [127], [128] Unfortunately, while residual stress distribution in traditional FSW is widely researched, there is limited research on residual stress for SRFSW and considerably less for dissimilar alloys of interest – aluminum 2195/2219.

High-resolution maps of the residual strain/stress state in the normal, transverse, and longitudinal directions were created using neutron diffraction for two dissimilar SRFSWs of aluminum 2195-T88/2219-T87 and 2195-T8M4/2219-T851. Due to high neutron penetration of aluminum near complete subsurface evaluation of the weldment is

possible. [32] In this study, scattering angle changes are measured and used to determine *d*-spacing and, with the aid of a stress-free reference, residual strain and stress distribution. Supporting microstructural and microhardness studies are described.

4.3 Experiment/Methods

Two dissimilar SRFSW plates (2195-T88/2219-T87 and 2195-T8M4/2219-T851) were prepared at NASA Marshall Space Flight Center (MSFC) in butt weld configuration using proprietary processing parameters and tool design. The 2195-T8M4/2219-T851 plate was sectioned in the longitudinal and transverse directions to give a 'T-shaped' geometry while the rectangular 2195-T88/2195-T87 was left unaltered. Plate geometries are given in **Figure A4-1**.

4.3.1 Microstructure

To assist in gauge volume selection and ensure that the neutron diffraction measurements were unaffected by variations in grain size, microstructural analysis of the weld was conducted. Transverse cross-sections were taken from the weld using wire electrical discharge machining (EDM) and mounted in epoxy. The specimens successively ground and polished to 0.5 μm colloidal silica. The sample was immersed in Weck's, a color etchant (1g sodium hydroxide, 4g potassium permanganate, and 100 mL water), for 10 s then removed and rinsed with cold deionized water. A Nikon Eclipse MA200 was used to image the etched specimens at magnifications of 50x, 100x, 200x, and 500x in the BM, HAZ, TMAZ, and SZ. A macrograph of the weld joint was constructed by stitching images taken with a Keyence VHX-1000 in *Fiji* (*ImageJ*).

4.3.2 Microhardness

Microhardness measurements were performed on 5 mm thick, transverse weld cross-sections that were been epoxy mounted, ground, and polished**.** Measurements were taken at 0.50 mm intervals in the normal and transverse directions using a LECO AMH 55 with load of 500 gf (4.903325 N) and 15 s dwell time.

4.3.3 Neutron Diffraction Measurements

Neutron diffraction measurements were conducted at the High Flux Isotope Reactor (HFIR) at Oak Ridge National Laboratory (ORNL) on the High Intensity Diffractometer for Residual Stress Analysis (HIDRA). [114], [115] The wavelength was adjusted via a bent Si crystal focusing Popovicci-Stoica monochromator using the Si (331) monochromator setting (λ = 1.731 Å) to provide a scattering angle of ~90° for the Al (311). Al (311) was chosen for this study as it is not readily affected by intergranular strains, provides relatively high peak intensity, possesses high multiplicity (decreasing textural impact) and an elastic modulus approximating that of the bulk. [32], [39] Though not explored in this study, limited texture analysis could be possible as the measured 2θ range includes the Al (222).

The instrument was aligned with the approximate weld center via an optical telescope ($\pm$0.3 mm estimated accuracy). Plate edges and geometry variation was determined by scanning along the measurement space, allowing formation of a virtual coordinate system related to the sample coordinate system. Measurements in the three orthogonal directions (transverse, normal, and longitudinal) were performed at positions +/- 2.1 mm along the plate thickness and to +/- 60 mm as measured from the weld centerline using the intersection of the half thickness and weld centerline as the origin. Peak fitting was performed in PyRS via a pseudo-Voigt fitting function to determine *d*-spacing from the measured scattering angle. [117]

Gauge volume

A tall, matchstick-like gauge volume (2 x 20 x 2 mm) was chosen for the normal and transverse directions to reduce counting and instrument time. Owing to the large texture variation and contrast difference between the Al-Cu (2219) and Al-Cu-Li (2195) plates, several gauge volumes were evaluated for the longitudinal selection. Ultimately, a 2 x 2 x 2 mm gauge volume was chosen for this direction as it achieved adequate statistical separation between the Al (311) peak and background intensity at all points. This gauge volume and measurement position selection results in almost complete sample coverage.

d_0 determination/selection

SRFSW causes significant changes to the microstructure and chemical composition of the joint. In 2219 and 2195 this is primarily due to the coarsening and solvation of precipitates in the matrix leading to changes in *d*-spacing and a false apparent strain. [32], [42] Therefore, a stress-free reference comb was created to allow mechanical relaxation of local macrostresses and account for changes in chemical composition and microstructure across the weld.

The stress-free reference (d_0) was created at the weld terminus plate end for both dissimilar SRFSWs. A bandsaw was used to section the plate approximately 8 cm from the plate end and EDM was used to create 20 mm longitudinal cuts at 4 mm intervals to +/- 60 mm from the weld centerline, **Figure A4-2**.

Measurements were taken approximately 330 mm and 120 mm from the orthogonal measurement position for the 2195-T88/2219-T87 and 2195-T8M4/2219-T851 welds, respectively. For the 2195-T88/2219-T87 SRFSW, normal d_0 measurements were taken at +/- 2 mm from the midthickness at intervals of 4 mm from the weld centerline to +/- 60 mm. After evaluation of the d_0 measurements, a simplified scheme was chosen for the 2195-T8M4/2219-T851 SRFSW in which normal and transverse direction d_0 were measured at the weld midthickness to +/- 60 mm at 4 mm intervals.

Determination of d-spacing, strain, and residual stress

The principle of diffraction/scattering is defined by Bragg's law, equation 4-1, which relates the wavelength (λ), interplanar or *d*-spacing (d), and scattering angle (2θ).

$$\lambda = 2d\sin\theta \tag{4-1}$$

The wavelength is known and the scattering angle of the measured peak is obtained via peak fitting of the data, rearranging equation 4-1 the lattice *d*-spacing can be calculated from:

$$d = \frac{\lambda}{2\sin\theta} \tag{4-2}$$

With the d-spacing determined, the residual strain for each principal direction becomes possible by relating the d-spacing difference between the measured point (d) and its stress-free reference (d_0) divided by the stress-free reference d-spacing (d_0).

$$\varepsilon = \frac{d-d_0}{d_0} \tag{4-3}$$

Using the computed residual strain in each principal direction as in equation 4-3, the calculation of residual stress becomes possible. [32], [38] Hooke's Law, equation 4-4, is applied along with isotropic conditions to provide the following relation, equation 4-5:

$$\sigma = E\varepsilon \tag{4-4}$$

$$\sigma_i = \frac{E}{1+\nu}\left[\varepsilon_{ii} + \left(\frac{\nu}{1-2\nu}\right)(\varepsilon_{11} + \varepsilon_{22} + \varepsilon_{33})\right] \tag{4-5}$$

where σ_i is the component of residual stress, E is the elastic (Young's) modulus, ν is Poisson's ratio, and ε_{ii} is the component of residual strain.

Model Selection

The Voigt model was selected for residual stress calculation as the *hkl* contributions, aside from Al (311), cannot be determined and minimal error is expected using this method in a static experiment. Assumptions of this model are uniform strain as well as constant and isotropic elastic modulus and Poisson's ratio. Elastic modulus and Poisson's ratio were determined by averaging the values for 2219-T8 (E = 73.1 GPa, and n = 0.33) and 2195-T8 (E = 69 GPa, and n = 0.33), resulting in E = 71.05 GPa, and n = 0.33.

An abrupt transition between the alloys occurs in the SZ and pin-pointing that transition to the specific measurement location and properties was not attempted. The average value approach is considered reasonable as minimal difference in resultant residual stress (<10 MPa) was observed between use of 2219, 2195, and a 2219/2195 averaged elastic modulus.

4.3.4 Force Balance

Residual stress is self-equilibrating meaning the sum of forces must balance (i.e. equal zero) over the plate under static conditions, equation 4-6. Stress components relate to the

force over the area perpendicular to the force, equation 4-7. In this case, the area is defined as the area between measurements.

$$\Sigma\sigma_{11} = 0;\ \Sigma\sigma_{22} = 0;\ \Sigma\sigma_{33} = 0 \quad (4\text{-}6)$$

$$\sigma_{ij} = F_{ij}/A \quad (4\text{-}7)$$

Extrapolation
The force balance approach can only be conducted over the measured cross-section length and thickness. As the measurements do not extend the full length of this span (+/- 60 mm in each direction and for the d_0 *d*-spacing data) extrapolation is necessary. A constant extrapolation method was selected in which the last data points of each measurement direction are held constant and extended over the range without adjustment. The force balance (equation 4-6) was solved using the "Goal seek" function in Microsoft Excel and then applied.

4.4 Results

4.4.1 Macro and Microstructure

A macrograph and micrographs of 2195-T88/2219-T87 SRFSW are presented in **Figure A4-3** and **Figure A4-4**, respectively. **Figure A4-5** and **Figure A4-6** display the macrograph and micrographs of 2195-T8M4/2219-T851, respectively.

4.4.2 Microhardness

Microhardness values were averaged at the midthickness (+/-1.5 mm thickness) to produce a line graph, **Figure A4-7**. Microhardness values display the general 'W-shaped' trend characteristic of dissimilar FSWs. The transition from 2219 to 2195 is demarcated by a sharp increase in stir zone microhardness and aligns with the joint line. Microhardness values for both metals decrease from the base metal to the TMAZ and increase slightly in the stir zone. Minimal microhardness values are ~96 HV for 2219 and ~119 HV for 2195. The highest values are observed in the BM, 151 HV for 2219 and ~181 HV for 2195. The 2219 and 2195 SZ have local maxima of 109 HV and 130 HV, respectively. Microhardness contour plots, **Figure A4-8**, clearly illustrate the dissimilar

joint transitions and weld zones for each dissimilar SRFSW (a and b) as well as differences between the dissimilar SRFSWs (c) and similar 2219-T87 SRFSW (d).

4.4.3 Neutron Diffraction

d-spacing

Peak fitting in PyRS produced *d*-spacing data for the transverse, normal, and longitudinal directions and d_0 as shown in **Figure A4-9**. In general, the *d*-spacing of the advancing side is slightly lower than that of the retreating side. The highest *d*-spacing was observed on the retreating side (2195) of the longitudinal direction with a slight decrease seen on the advancing side. The lowest *d*-spacings are seen in the stir zone of the normal and transverse directions of the advancing side (2219). A "U" or "V" shaped profile is apparent for the normal and transverse directions while an M-shaped pattern is observed in the longitudinal direction. The normal and transverse profiles of the dissimilar joints differ from similar joints in that a small decrease or plateau is present on the retreating side. Contour plots of the normal, transverse, longitudinal, and d_0 *d*-spacing are presented in **Figure A4-10** and **Figure4-11** for 2195-T88/2219-T87 and 2195-T8M4/2219-T851, respectively.

FWHM

The full-width half maximum for the Al (311) was utilized to evaluate transitional regions and general grain size and microstrain evolution as in **Figure A4-12** and **Figure A4-13**. The FWHM was noted to decrease from the base metal to the stir zone for each weld and all directions.

Strain

Residual strains were measured in the normal, transverse, and longitudinal directions and are presented in 1D plots in **Figure A4-14** and contour plots in **Figure A4-15** and **Figure A4-16** for 2195-T88/2219-T87 and 2195-T8M4/2219-T851, respectively. Longitudinal residual strain follows an asymmetric 'M-shaped' distribution where the highest value occurs on the retreating side just outside the TMAZ. The SZ in both dissimilar welds show a sharp increase at the transition region between 2219 and 2195 though is more prominent for the 2195-T88/2219-T87 SRFSW. Transverse and normal residual strains

are ‘W-shaped’ and of significantly lower magnitude with maxima in the base metal and minima in the HAZ. The transverse and normal residual strain of the 2195-T88/2219-T87 SRFSW also shows a marked increase in strain near the alloy transition where it reaches a local SZ maximum.

The maximum longitudinal residual microstrain was at or just outside the TMAZ of both dissimilar welds while the minimum was on the retreating side BM. Transverse microstrain reached a minimum in the retreating side HAZ near the TMAZ and a maximum on the retreating side BM. Normal microstrain was highest on the advancing side BM and lowest on the retreating side HAZ near the TMAZ.

Stress

Residual stress was calculated via equation 4-4 using the averaged values for modulus and Poisson’s ratio between 2219-T8 and 2195-T8 (E = 71.05 GPa and ν = 0.33) and a force balance subsequently applied. The resultant 1D stress profiles are given in **Figure A4-17** and contour plots in **Figure A4-18** and **Figure A4-19** for 2195-T88/2219-T87 and 2195-T8M4/2219-T851, respectively.

The longitudinal residual stress follows an asymmetric ‘M-shaped’ pattern with a higher retreating side. The normal and transverse directions follow a ‘W-shaped’ profile for 2195-T88/2219-T87 SRFSW and a broad hump for the 2195-T8M4/2219-T851 SRFSW. In general, the highest longitudinal residual stress occurred at or just outside the TMAZ of the retreating side and at the weld transition between the alloys. Normal and transverse residual stress profiles were similar to the longitudinal residual stress profile but with significantly lower magnitude.

4.5 Discussion

Neutron diffraction allowed for the measurement of scattering angle and the calculation and mapping of residual strain and stress for two dissimilar SRFSWs. Chemical and microstructural variation were accounted with use of a stress-free reference comb and force balance.

4.5.1 Macro-Microstructure

The SRFSW hallmark ‘hourglass-shaped’ SZ macrostructure was noted, however, it was more prominent on the advancing side (2219). The alloy transition in the SZ was visible and marked by a color difference. Gross weld defects were not visible.

The BM, HAZ, TMAZ, and SZ were apparent. Grain size was not determined due to high irregularity and poor grain boundary contrast of the 2195 grains. Therefore, only qualitative observations are provided. The HAZ possessed coarsened grains compared to the BM which became elongated and irregular in the TMAZ while the SZ possessed fine, equiaxed grains. Texture variation appeared more severe on the retreating side (2195) compared to the advancing side (2219). Macroprecipitate counting was possible for the 2219 (advancing side) but not for the 2195 (retreating side) owing to the exceeding small precipitate size for this alloy. Ultimately, macroprecipitate counting was not pursued due to inconsistency and limited usefulness in comparing local weld properties.

4.5.2 Microhardness

Microhardness profiles can provide additional insight into the physical properties of a weld when paired with metallography. Weld zones and transitions are readily identifiable with the lowest local microhardness for each alloy occurring in the TMAZ and the highest in the BM. The profiles are grossly ‘W-shaped’ with decreasing microhardness values from the BM to the TMAZ and slight recovery in the SZ. An abrupt transition occurs near the weld center which aligns with the joint transition. Contour plots show little thickness-related variation in the BM, HAZ, and TMAZ with a clear alloy transition in the SZ which closely aligns with macro-microstructure. The HAZ of the retreating and advancing sides are approximately equal in size. While direct literature comparison to an analogous dissimilar SRFSW was not possible, the ‘W-shaped’ profile agrees with other studies on SRFSW and FSW. [128]–[130] Comparable microhardness values were reported for each weld zone in studies of similar aluminum 2219 and 2195 SRFSWs. Schneider et al’s work on FSW AA2195-T81 gave average hardness values of 90 $\pm$0.5 HB (~180 HV) and 67 $\pm$2 HB (~130 HV) for the BM and SZ, respectively. [103] Study of 2219-T87 SRFSW by Wen et al. gave hardness values of 140-150 HV for the BM and

a minimal value of ~108 HV on the retreating side HAZ adjacent to the TMAZ. [122] Finally, similar and dissimilar FSWs of 2195/2219 were evaluated by Agilan et al. The lowest microhardness values occurred in the TMAZ (~84 HV) while the highest microhardness was observed in the BM (178 HV for 2195-T87 and 146 HV for 2219-T87). These results show excellent agreement between this study and available literature.

In precipitation hardenable aluminum alloys, precipitate evolution is a primary strengthening agent with grain size providing a significantly lesser impact. [14] Microhardness is thereby expected to reflect changes to the precipitation state where coarsening, overageing, and dissolution during welding leads to decreases of microhardness from the BM to the TMAZ. Microhardness recovery in the SZ may be due to solid-solution strengthening and re-precipitation/natural ageing or a combination. These factors were not evaluated in this study.

4.5.3 Strain

Residual strain was successfully calculated from measured *d*-spacing. The strain profiles were within expectations with 'M-shaped' longitudinal strain and 'W-shaped' normal/transverse strain profiles. The width of these profiles extended to just beyond the TMAZ and approximates the tool size.

A small local peak is present in the central stir zone of the 2195-T88/2219-T87 SRFSW. The inclusion of this region in the alloy transition region may indicate the possibility of an erroneous strain due to edge effects/texture or unaccounted chemical variation. These factors are discussed in more detail in the Stress section.

4.5.4 Stress

Residual stress profiles for both welds followed the expected 'M-shaped' pattern though differed in local magnitude and central morphology. The maximum longitudinal residual stress occurred on the retreating side for both SRFSWs well below yield stress for 2195-T8 (560 MPa).

The two profiles differed the most in the region between the respective TMAZs. 2195-T88/2219-T87 possesses a sharp increase in residual stress approaching the alloy

transition and a significantly more variable normal and transverse residual stress. This abrupt transition could be attributed to a number of factors such as not adequately accounting for abrupt changes in microstructure or chemical composition leading to an "edge effect". Normalized intensity (I/I_0) was plotted for each direction with minimal variation in the normal and longitudinal directions but significant decrease in intensity in the central SZ in the transverse direction. This indicates the potential for an "edge effect" skewing the stress/strain values in these transition regions though the magnitude of this effect cannot be determined. As such, the central peak should be discounted as erroneous. Discounting the central peak, the maximum longitudinal residual stress of the retreating side was less than half the yield stress of both alloys.

The 2195-T8M4/2219-T851 SRFSW follows a more general hump profile for the normal and transverse directions with a slight local maximum near the alloy transition. Here, however, the normalized intensity difference is insignificant. The primary concern in this instance is accounting for potential stress relaxation from post-weld sectioning (longitudinal and transverse). Altenkirch et al. in a study on sectioning related residual stress relaxation, determined that sectioning along the transverse and longitudinal planes produced decreases in longitudinal residual stress while transverse residual stress was largely unaffected. [131] 90% of longitudinal residual stresses were maintained when sectioning along the transverse plane at a distance 12 times the FSW pin diameter. Longitudinal plane sectioning also produced a decreased longitudinal residual stress at plate widths of less than 300 mm. Here the sectioning that produced the T-shaped plate was a combination of these directional sectioning and an accurate correction is unlikely.

4.6 Conclusion

Residual stress and strain in the normal, transverse, and longitudinal directions were obtained from a measured *d*-spacing for two dissimilar SRFSWs – 2195-T88/2219-T87 and 2195-T8M4/2219-T851. Microstructure and microhardness were evaluated showing an hourglass-appearance and correlation between weld properties and zones. Residual stress profiles followed a largely 'M-shaped' distribution in each case. The magnitude of the greatest tensile longitudinal stress occurred on the retreating side of the weld and was

less than half the alloy's yield stress. Local maxima were observed in the alloy transition zone near the weld center and may indicate erroneous strain/stress due to the significant difference in texture at this position. Stress relaxation is also a concern for the 2195-T8M4/2219-T851 SRFSW due to the post-weld sectioning. Correction of the longitudinal stress relaxation is hampered by unknown initial tensile peak half-width. However, sectioning effects on transverse residual strain/stress are expected to be negligible. [131]

4.7 Acknowledgements

The authors would like to acknowledge partial support though the Manufacturing and Materials Joining Innovation Center (Ma^2JIC) University of Tennessee, Knoxville site. Ma^2JIC is funded by the National Science Foundation (NSF) through the Industry/University Cooperative Research Center (I/UCRC) program award number IIP 1822186. This research used resources at the High Flux Isotope Reactor a DOE Office of Science User Facility operated by the Oak Ridge National Laboratory. The authors would like to thank Kevin Sisco for his contribution and assistance in microhardness testing.

Appendix

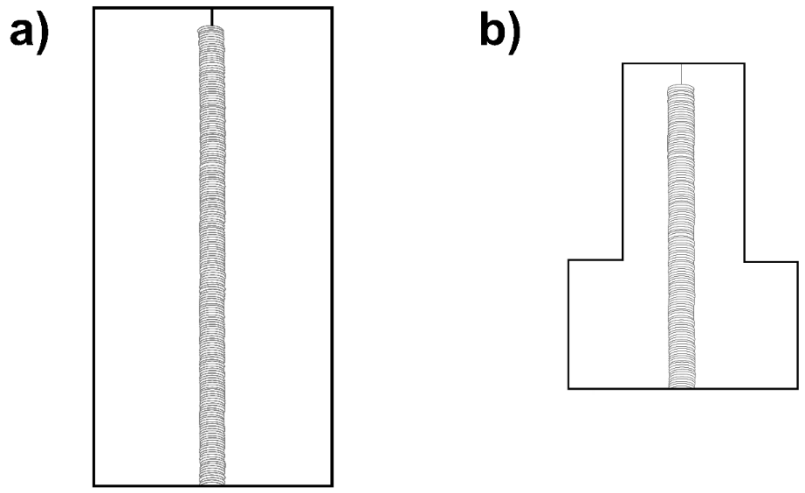

Figure A4-1 Plate geometry for 2195-T88/2219-T87 and (b) 2195-T8M4/2219-T851

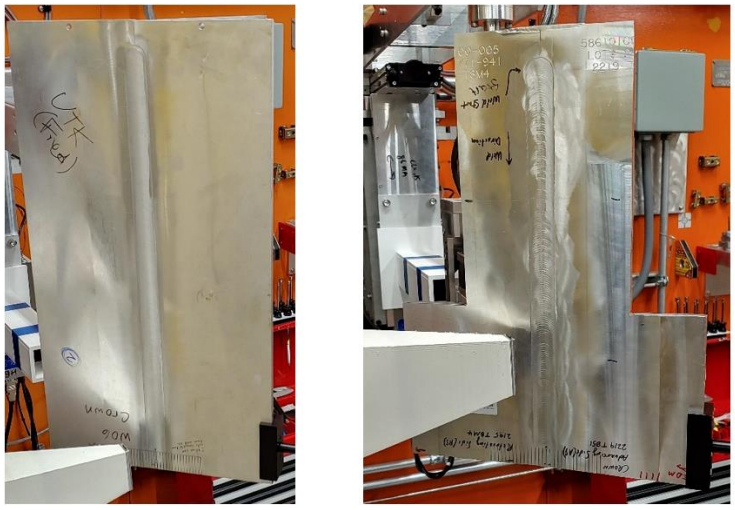

Figure A4-2 Weld plates with stress-free reference comb (left) 2195-T88/2219-T87 (right) 2195-T8M4/2219-T851



Figure A4-3 2195-T88/2219-T87 SRFSW macrograph

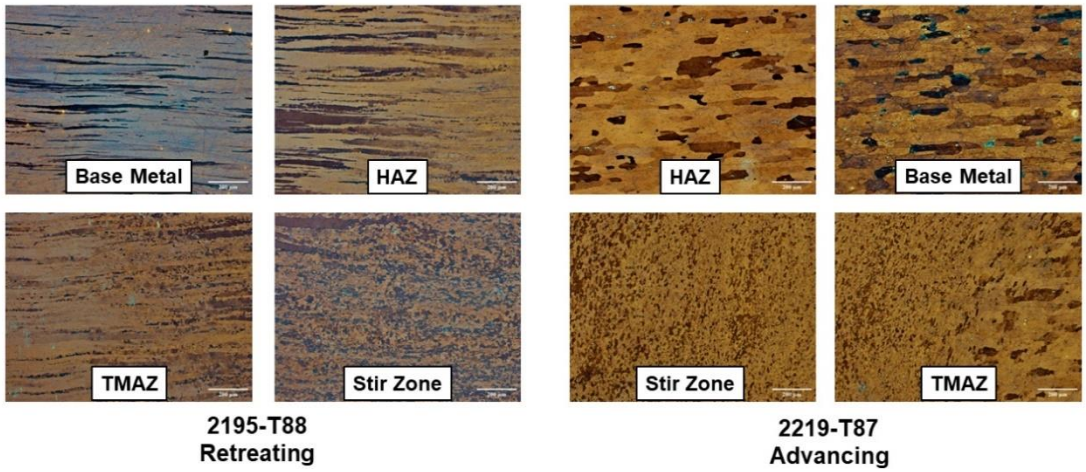

Figure A4-4 Micrographs of each weld zone in 2195-T88/2219-T87 SRFSW



Figure A4-5 2195-T8M4/2219-T851 SRFSW macrograph

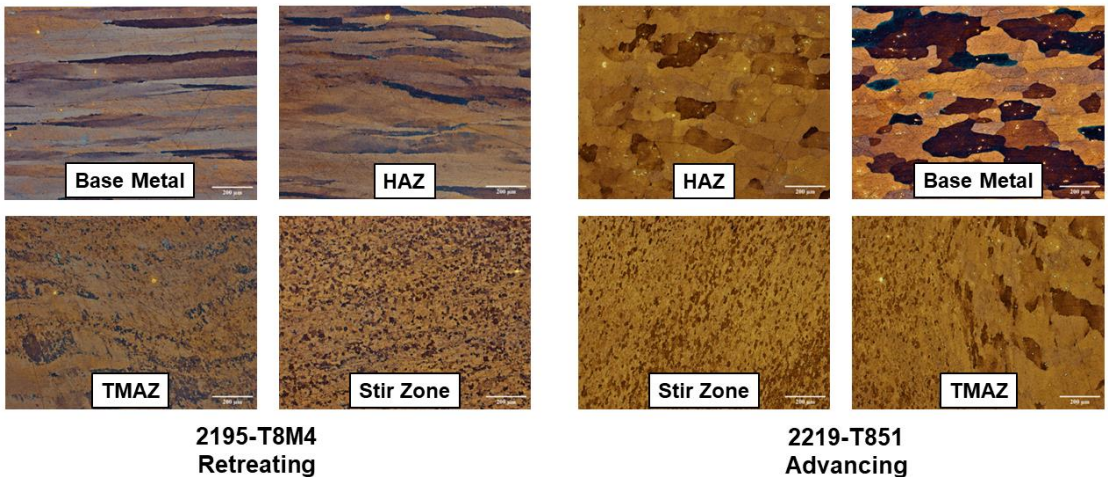

Figure A4-6 Micrographs of each weld zone in 2195-T8M4/2219-T851 SRFSW

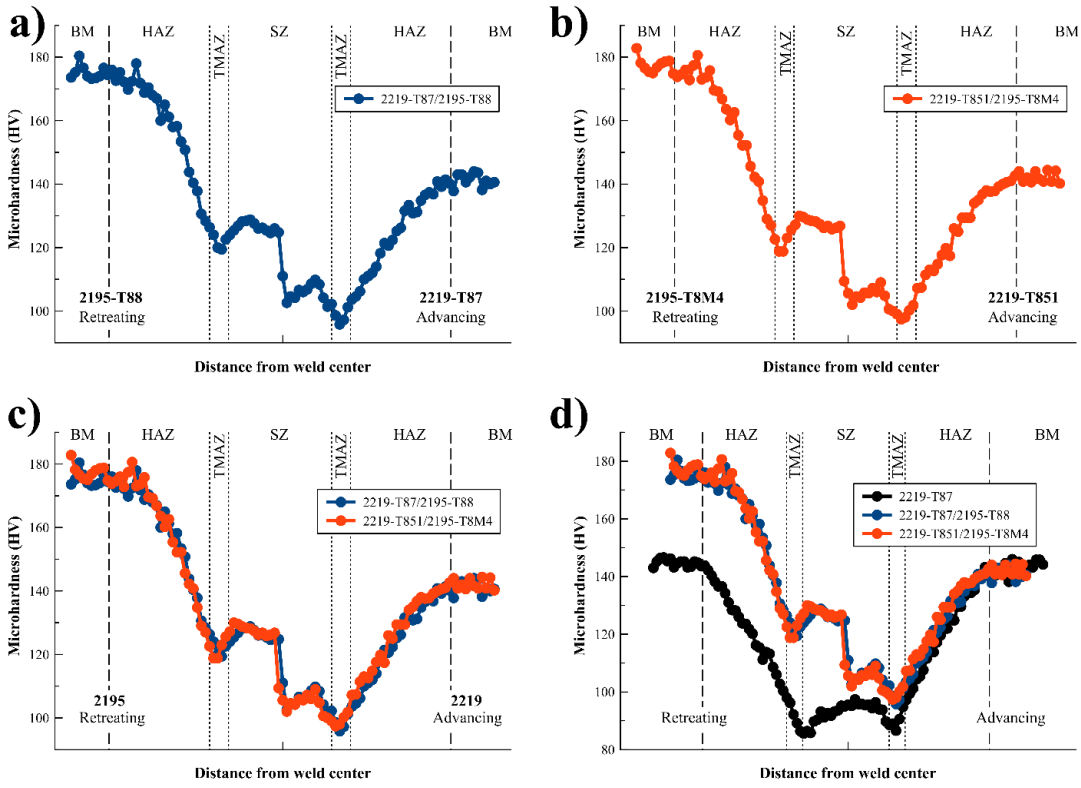

Figure A4-7 Midthickness averaged microhardness plot (a) 2195-T88/2219-T87, (b) 2195-T8M4/2219-T851, (c) dissimilar SRFSWs, and (d) dissimilar and similar SRFSWs

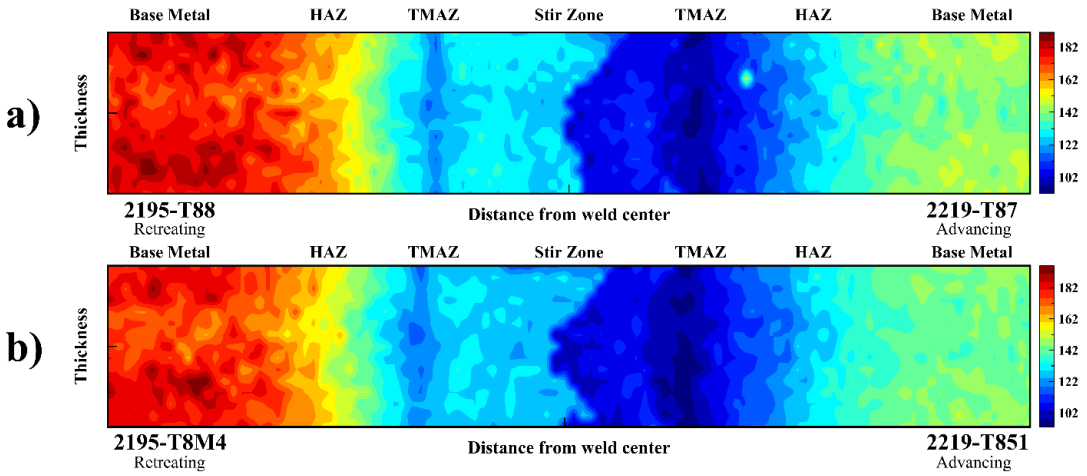

Figure A4-8 Microhardness contour plot (a) 2195-T88/2219-T87, (b) 2195-T8M4/2219-T851

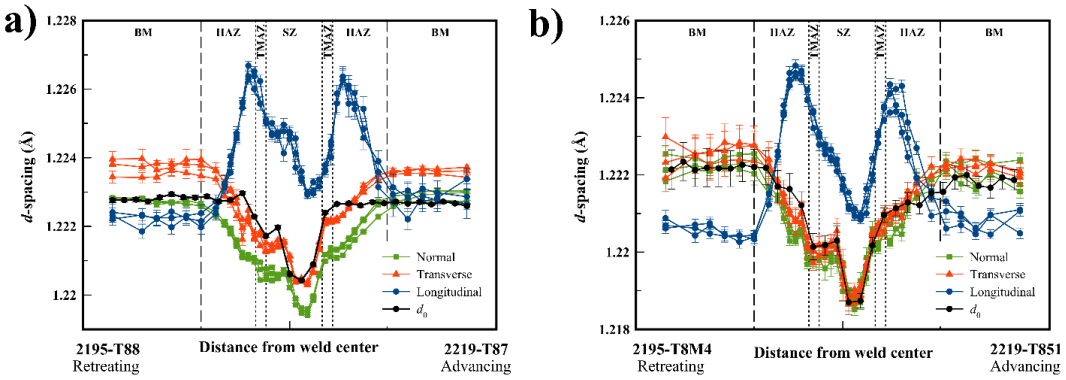

Figure A4-9 Normal, transverse, longitudinal, and d_0 *d*-spacing (a) 2195-T88/2219-T87 and (b) 2195-T8M4/2219-T851

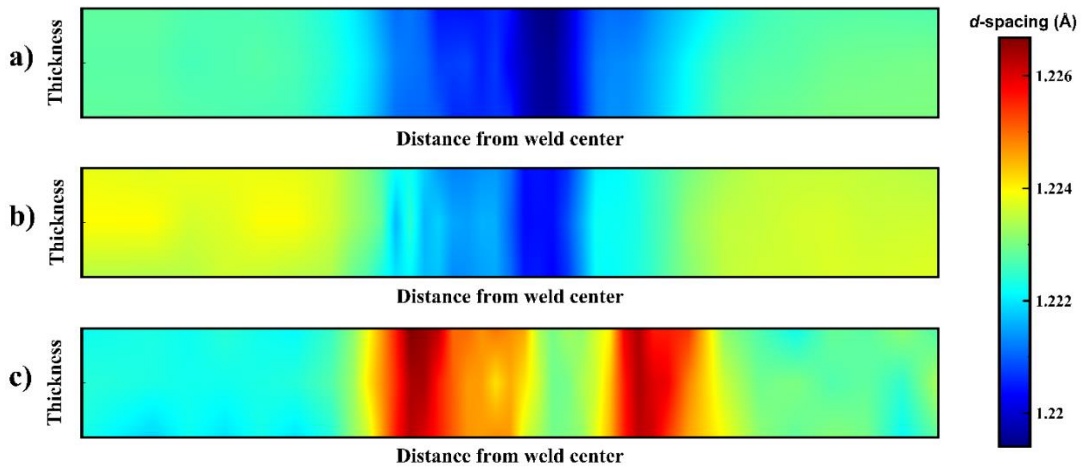

Figure A4-10 2195-T88/2219-T87 *d*-spacing contour plots for (a) normal, (b) transverse, and (c) longitudinal directions

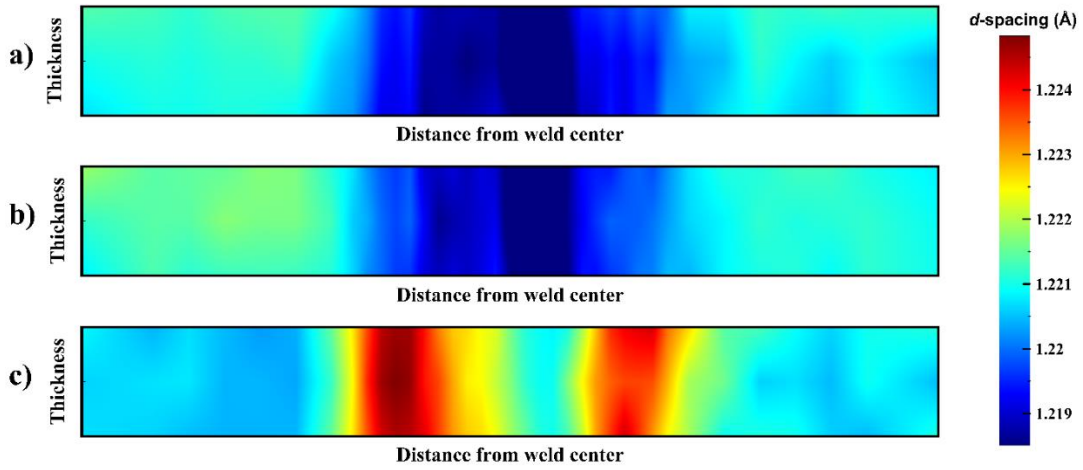

Figure A4-11 2195-T8M4/2219-T851 *d*-spacing contour plots for (a) normal, (b) transverse, and (c) longitudinal directions

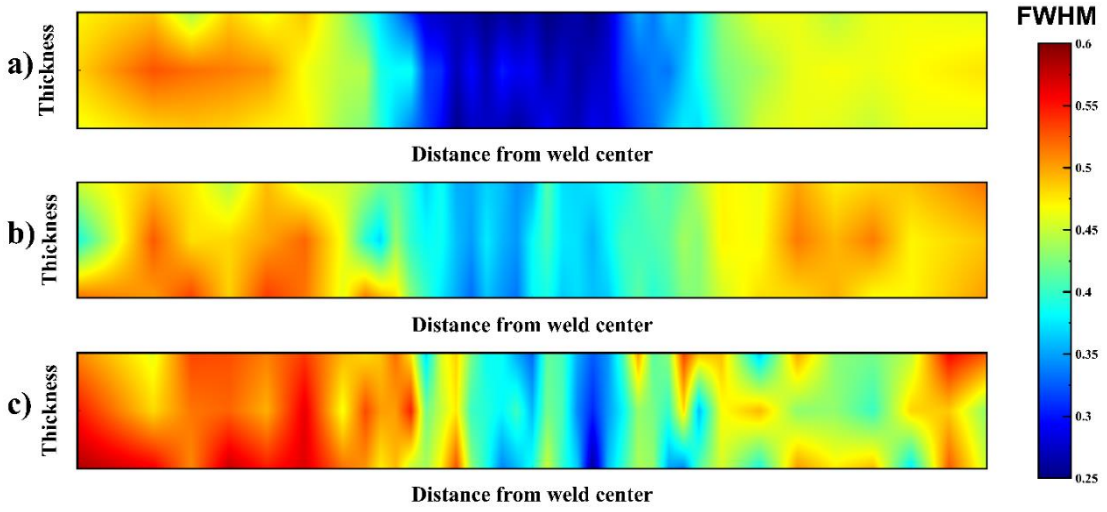

Figure A4-12 2195-T88/2219-T87 FWHM contour plots in the a) normal, b) transverse, and c) longitudinal directions

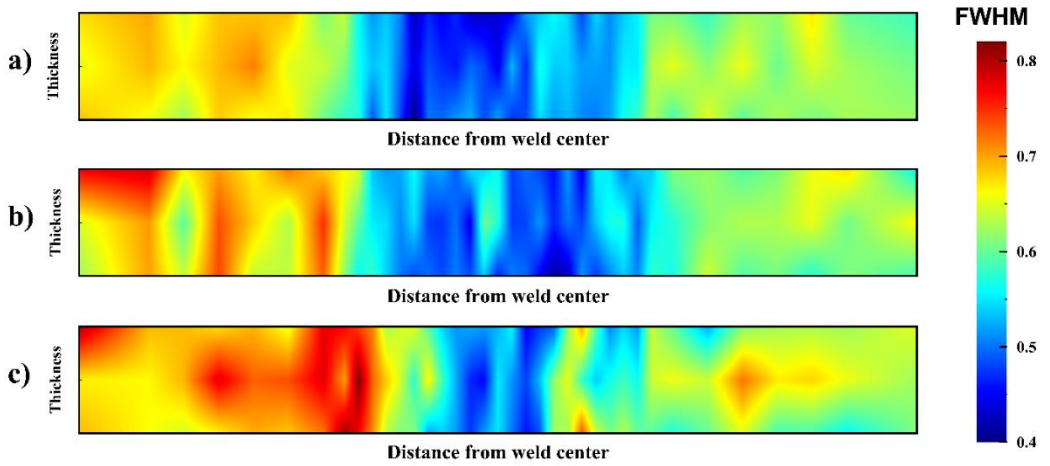

Figure A4-13 2195-T8M4/2219-T851 FWHM contour plots in the a) normal, b) transverse, and c) longitudinal directions

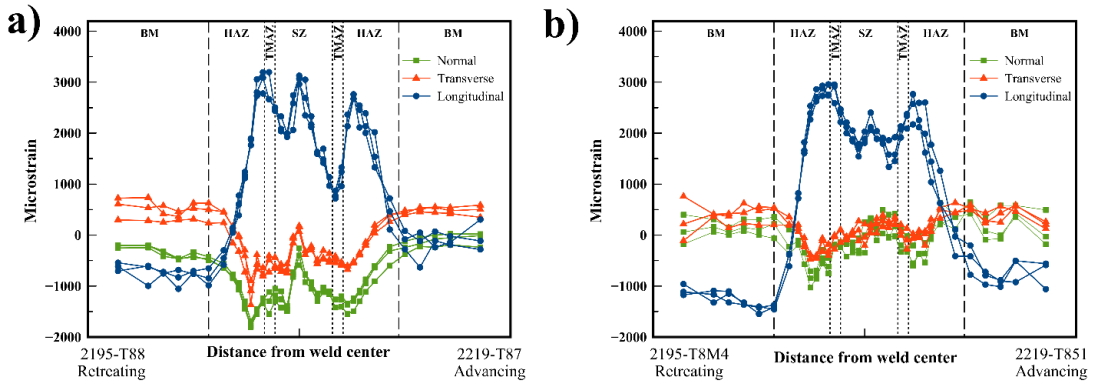

Figure A4-14 Residual strain in the normal, transverse, and longitudinal directions for (a) 2195-T88/2219-T87 and (b) 2195-T8M4/2219-T851

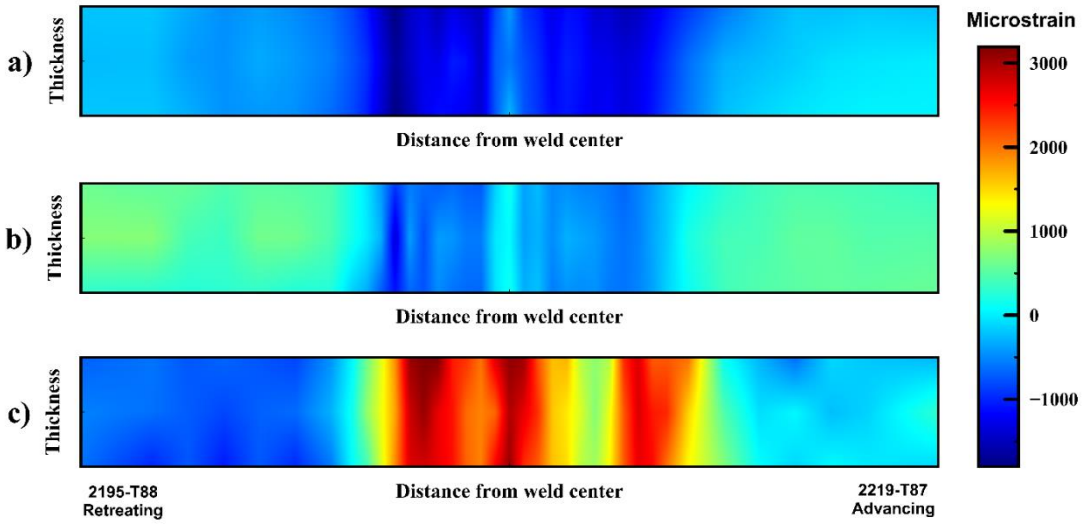

Figure A4-15 2195-T88/2219-T87 residual strain contour plots in the (a) normal, (b) transverse, and (c) longitudinal directions

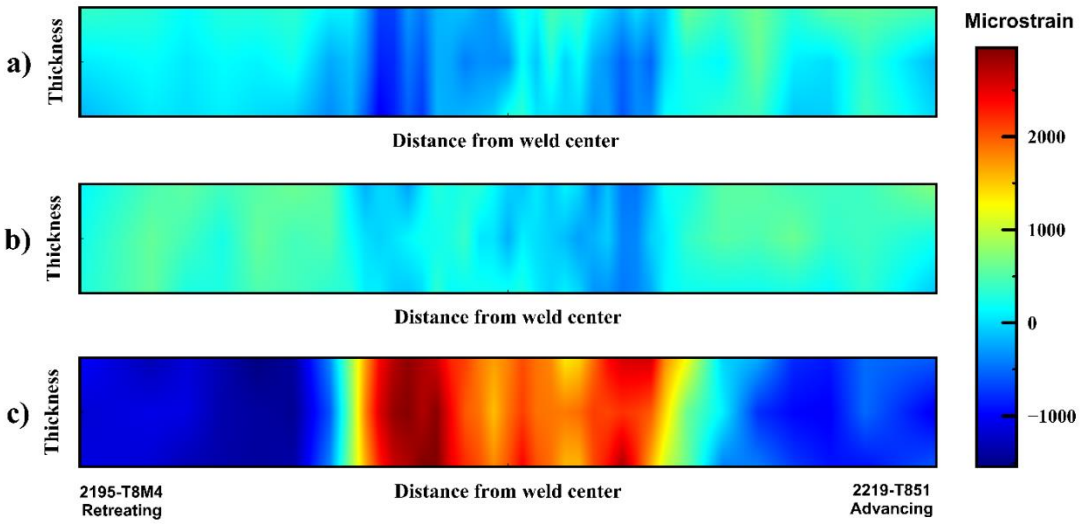

Figure A4-16 2195-T8M4/2219-T851 residual strain contour plots in the (a) normal, (b) transverse, and (c) longitudinal directions

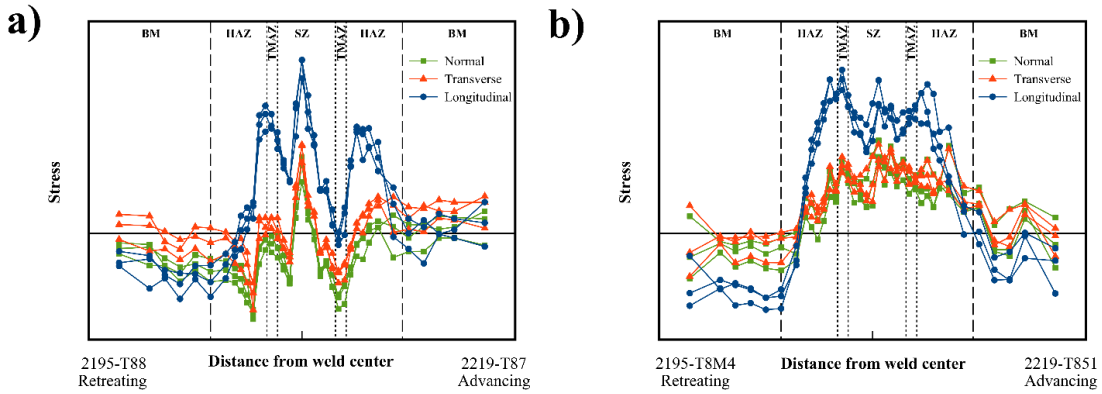

Figure A4-17 Residual stress in the normal, transverse, and longitudinal directions for (a) 2195-T88/2219-T87 and (b) 2195-T8M4/2219-T851

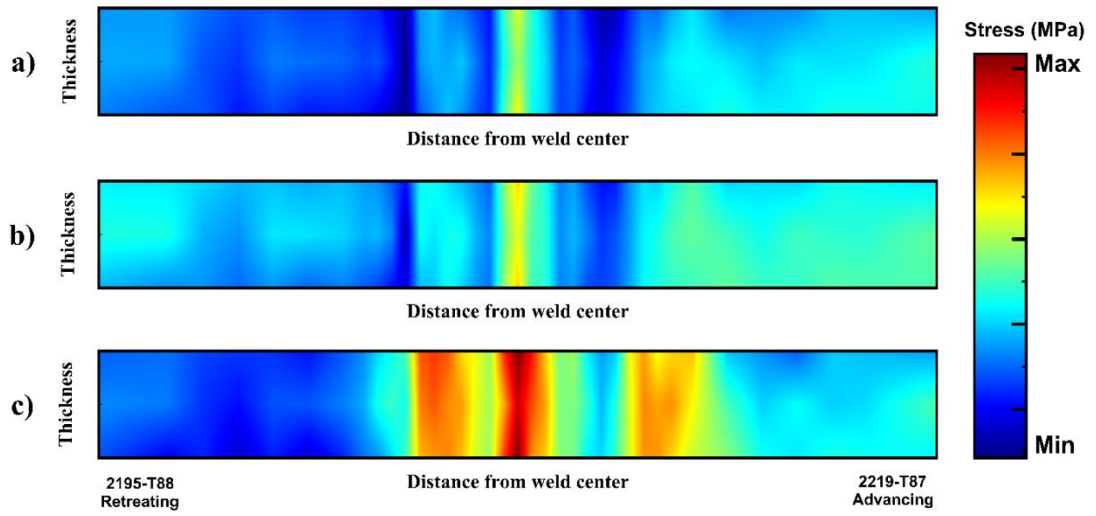

Figure A4-18 2195-T88/2219-T87 residual stress contour plots in the (a) normal, (b) transverse, and (c) longitudinal directions

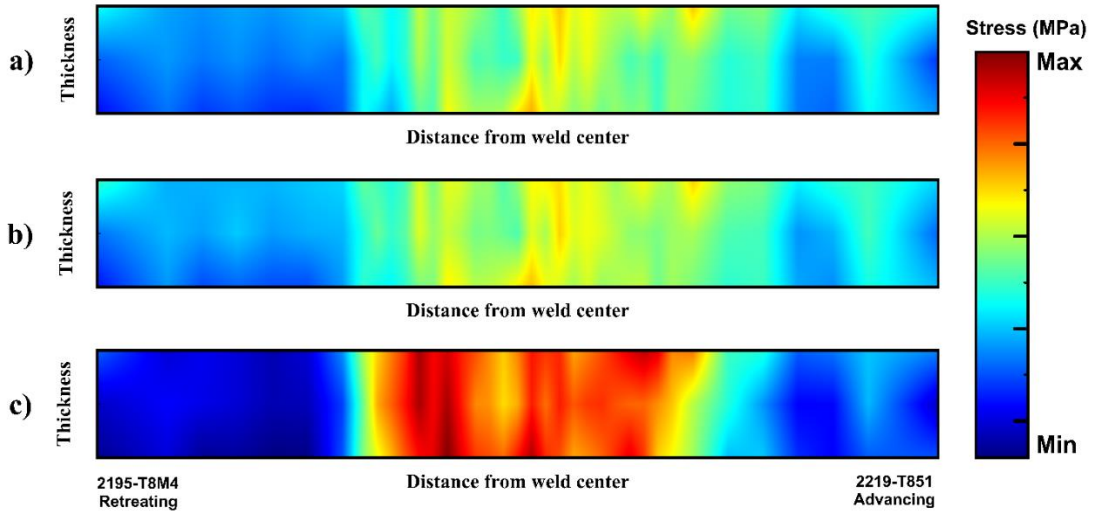

Figure A4-19 2195-T8M4/2219-T851 residual stress contour plots in the (a) normal, (b) transverse, and (c) longitudinal directions

CHAPTER V
PRECIPITATE EVOLUTION IN A 2219-T87 SELF-REACTING FRICTION STIR WELD

This chapter is in preparation for submission to Acta Materialia for publication by Benjamin Joe Wing, Dov Polsky, Lisa Debeer-Schmitt, Ken Littrell, Fredrick N. Michael, and Claudia J. Rawn:

B.J. Wing, D. Polsky, LM. Debeer-Schmitt, K.C. Littrell, C.J. Rawn, "Precipitate Evolution in a 2219-T87 Self-reacting Friction Stir Weld", *Acta Materialia*.

The article is presented as it was submitted, without change. Portions of the Chapter I were used in this publication. Benjamin Joe Wing and Dov Polsky completed and analyzed the metallography. Kevin Sisco performed the microhardness testing. Microhardness data was analyzed by Benjamin Joe Wing. X-ray fluorescence data were collected and analyzed by Benjamin Joe Wing and Michael Koehler. High temperature x-ray diffraction data were collected by Benjamin Joe Wing and Michael Koehler and analyzed by Benjamin Joe Wing. Small-angle neutron scattering data were collected by Ken Littrell and analyzed by Benjamin Joe Wing, Ken Littrell, and Lisa Debeer-Schmitt. Ultra-small, small-angle, and wide-angle x-ray scattering data were collected by Jan Ilavsky and analyzed by Benjamin Joe Wing. Benjamin Joe Wing and Claudia Rawn wrote the paper.

5.1 Abstract

The precipitation and microstructural evolution in an aluminum 2219-T87 self-reacting friction stir weld (SRFSW) was analyzed via complementary techniques of small-angle scattering (SAS) - ultra small-angle x-ray scattering (USAXS), small-angle x-ray scattering (SAXS), wide-angle x-ray scattering (WAXS), and small-angle neutron scattering (SANS)-, high-temperature x-ray diffraction (HTXRD), x-ray fluorescence (XRF), metallography (optical and scanning electron microscopy), and microhardness. The precipitates θ' and θ (Al_2Cu) as well as intermetallic ω (Al_7Cu_2Fe) were identified in each weld zone via WAXS and HTXRD. HTXRD shows θ' presence in the temperature range of 175-325 °C with dissolution around 275- 300 °C and θ present between 225-475 °C with dissolution starting around 400 °C. WAXS shows the highest concentration of θ' and θ lie in the heat affected zone (HAZ) and thermo-mechanically affected zone (TMAZ), respectively, with both reaching a minimum in the stir zone. SAS data suggests

the scatterer morphology is a plate/disc shape which aligns with literature reports. In both SANS fitting levels thickness increased to the HAZ/TMAZ before dissolution in the stir zone (SZ) - measuring 2-9 nm and 20-60 nm. The volume fraction of θ' was observed to decrease from the base metal to the HAZ while θ volume fraction increased from the BM to the HAZ. Calculated relative volume fraction based on the invariant of both SANS fitting levels suggests decreasing precipitate volume fraction toward the SZ. This study corroborates similar SAS FSW studies in precipitation hardenable aluminum alloys.

5.2 Introduction

Aluminum alloys of the 2xxx series possess a high strength to weight ratio, good corrosion resistance, and stability at cryogenic temperatures as well as the ability to age harden making them particularly attractive for structural aerospace applications such as the development of liquid propellant rocket fuel tanks. [106] Owing to the size of these tanks, circumferential design, and poor weldability with fusion based processes, they are often constructed using self-reacting friction stir welding (SRFSW). In SRFSW, a rotating tool travels along abutting or overlapping plates and mixes the joint edges. The frictional heat produced by the rotating tool softens but avoids melting the material while the shearing action of the tool shoulders and pin provides mixing and bonding of the plates. SRFSW, with appropriate operating parameters, creates high-strength welds, however, joint softening remains a notable challenge for 2xxx alloys. [14], [25], [57], [106]

Joint softening, or the loss of mechanical properties, is primarily associated with the structural distribution and size of precipitates which govern the properties of the alloy and weldment in age-hardenable alloys such as the AA2xxx series. In FSW, precipitates are typically coarsened in the heat affected zone (HAZ) and undergo partial or full dissolution in the thermomechanically affected zone (TMAZ) and stir zone due to the frictional heat, resulting in lower mechanical properties compared to the base metal and fusion based welds. [57], [106] Unfortunately, though a large amount of information is available for other welding processes/variants and precipitate behavior there is a lack of research on precipitate evolution for SRFSW and many alloys.

However, quantification of SRFSW induced precipitate evolution is time consuming and difficult for techniques such as transmission electron microscopy (TEM) and atom probe tomography (APT) owing to limited sample area. [72] Small-angle scattering (SAS) either small-angle neutron scattering (SANS) or small-angle X-ray scattering (SAXS) is an excellent method for the study of such nanoprecipitates which allows for complete bulk characterization, mapping, and quantification of each of the weld zones of the SRFSW which is not afforded by other means. This technique has been successfully applied to the determination of precipitate evolution and spatial distribution in friction stir welds of the AA2xxx series (AA2014, AA2024, AA2050, AA2199, and AA7449). [89], [77], [132], [78], [83], [85] Limited work has been conducted on precipitation evolution for SRFSW of the alloy of interest to this study.

This work focuses on characterizing precipitate morphology and evolution in a thick plate AA2219-T87 SRFSW butt weld of a thick plate AA2219-T87 using complementary techniques of SAS (SANS/SAXS), x-ray diffraction (XRD) and wide-angle x-ray scattering (WAXS), as well as TEM and APT.

5.3 Experiment/Methods

A thick plate, 2219-T87 SRFSW in butt weld configuration was prepared at NASA Marshall Space Flight Center (MSFC) using proprietary processing parameters and tool design.

5.3.1 Microstructure

Transverse cross-sectional specimens were sectioned from the weld using wire electrical discharge machining (EDM), mounted in epoxy, and successively ground and polished to .05 μm colloidal silica. The sample was immersed in Weck's reagent for 10 s then removed and rinsed with cold deionized water. The etched specimens were imaged using a Nikon Eclipse MA200 at magnifications up to 500x in each weld region. A macrograph of the weld joint was constructed by stitching images taken using a Keyence VHX-1000 in *Fiji* (*ImageJ*). [112] Grain sizes were measured with *ImageJ* using the intercept method according to ASTM E112. [113] Macroprecipitates were manually counted using 50x optical micrographs for the advancing side base metal (BM), heat affected zone

(HAZ), and stir zone (SZ) and 100x optical micrographs for the thermo-mechanically affected zone (TMAZ), each sampled at three random locations in *ImageJ* to obtain number and linear number density.

5.3.2 Microhardness

Microhardness measurements were performed on an epoxy mounted, ground, and polished transverse weld cross-section of 5 mm thickness**.** Measurements were taken using a LECO AMH 55 at intervals of 0.75 mm to the sample edge in the normal (y direction) and transverse (x direction) directions using a load of 500 gf (4.903325 N) and 15 s dwell time.

5.3.3 X-ray Fluorescence (XRF)

Chemical composition of the 2219-T87 base metal was measured via X-ray Fluorescence (XRF) at the IAAM Diffraction Facility. A circular sample (16 mm diameter and 1 mm thickness) was extracted from the 2219-T87 base metal using EDM and ground successively to 1200 grit to ensure a level surface and remove surface contamination. Measurements were taken with a Malvern Panalytical Epsilon 1 on the Omnian Fast setting and the spectra fit and composition quantified using the onboard software (Epsilon 3).

5.3.4 X-ray Diffraction (XRD)

High-temperature X-ray diffraction (HTXRD) was used to qualitatively identify precipitate evolution in 2219-T87 BM at temperatures approximating the SRFSW process. In preparation for the experiment, a 3 mm thick and 16 mm diameter 2219-T87 base metal sample was fabricated using EDM and successively ground to 1200 grit finish. The IAMM Diffraction Facility's Malvern Panalytical Empyrean was selected to conduct HTXRD measurements at 25 ℃ and from 150 ℃ to 450 ℃ in 25 ℃ increments over a 10-68° 2θ range using Cu radiation. Collection time for each pattern was 15 minutes.

5.3.5 Small-angle Neutron Scattering (SANS)

Small-angle neutron scattering (SANS) was performed on the General Purpose SANS (GP-SANS) beamline at Oak Ridge National Laboratory's (ORNL) High Flux Isotope Reactor (HFIR). [133] Three configurations were used and stitched to extend the

measured q range. A transverse cross-section (110 mm length and 1 mm thickness) was prepared using EDM and mounted. 22 measurements were taken along the weld midthickness using a 4mm diameter beam, **Figure A5-1**, using the measurement scheme illustrated in **Figure A5-2**. The 2D data was processed using beamline provided Jupyter notebooks and analyzed using the Unified Fit module of the IRENA package in Igor Pro 8. [134]

5.3.6 USAXS/SAXS/WAXS

USAXS/SAXS/WAXS were carried on the 9-ID-C beamline at the Advanced Photon Source (APS) at Argonne National Laboratory's (ANL). [135] The combined q range is between 1×10^{-4} $Å^{-1}$ and 6 $Å^{-1}$; here $q = 4\pi/\lambda \sin(\theta)$, λ is the wavelength and θ is ½ of the scattering angle. The X-ray energy was 21 keV ($\lambda = 0.5895$ Å). X-ray photon flux was ≈ 5×10^{12} $mm^{-2}s^{-1}$. USAXS data collection time was 90 seconds, SAXS/WAXS 20 seconds each. Beam size was 0.8 x 0.8 mm for USAXS and 0.8 x 0.2 mm for SAXS/WAXS.

SRFSW cross-sectional samples of 100 mm length were extracted using EDM then ground and polished to the 6 µm diamond stage on both faces (to avoid undesirable surface scattering) to a thickness of ~850 µm (± 50 µm). The sample was mounted using Scotch Magic Tape (3M) on the instrument provided sample holder, **Figure A5-3**. Measurements were conducted in the base metal regions of the advancing and retreating sides, in 1 mm increments to ±30 mm from weld center at weld midthickness, and in 2 mm increments to ±30 mm from weld center at ±¼ thickness from weld midthickness, **Figure A5-4**.

USAXS data were reduced using INDRA and SAXS/WAXS data were reduced using NIKA with Igor Pro 8. [136] Data were corrected for instrumental background using scans collected at the start, middle, and end of the measurement line. Data were placed on absolute intensity scale using measured sample thicknesses. [135] Data were desmeared to remove instrumental slit smearing. [134] Data were analyzed using Irena package using the Unified Fit module. [134] WAXS data was analyzed using GSAS II though experiment limitations prevent accurate and reliable phase quantification. [137]

5.4 Results

5.4.1 Macro and Microstructure

The macrostructure and microstructure of the 2219-T87 SRFSW is presented by **Figure A5-5** and **Figure A5-6**, respectively. The HAZ was noted by coarsened grains compared to the base metal, the TMAZ by elongated and deformed grains, and the stir zone by fine equiaxed grains.

Grain size slightly increased from the base metal to the HAZ and decreased significantly moving from the TMAZ to the SZ where it reached a minimum, **Figure A5-7**. Macroprecipitate number and linear density steadily decreased from the BM to the SZ, **Table A5-1**.

5.4.2 Microhardness

Mid-thickness microhardness values (+/- 2 mm thickness) were averaged to create a mid-thickness averaged line graph, **Figure A5-8**, where error bars are 1σ. Microhardness values follow a 'W-shaped' curve as is characteristic of FSWs. Microhardness values steadily decrease from the BM to the TMAZ and slightly recover in the SZ. Highest values are observed in the BM and lowest in the retreating side TMAZ. A contour plot of microhardness is given by **Figure A5-9**.

5.4.3 X-ray Fluorescence (XRF)

The XRF spectra and resultant fit is given by **Figure A5-10**. **Table A5-2** compares the measured base metal composition with the accepted 2219 composition limits. The measured weight percent composition falls within the composition limits dictated by the standard. [5]

5.4.4 HTXRD

HTXRD data is presented as a stacked plot in **Figure A5-11** and as a background subtracted waterfall plot in **Figure A5-12**. The presence of three secondary phases was observed – precipitates θ and θ' (Al_2Cu) and an intermetallic ω (Al_7Cu_2Fe). The θ' precipitates are observed over a range of 175-350 °C with dissolution onset around 275-300 °C while θ is present over a higher temperature range (225-475 °C) and dissolution

starting between 400-425 °C. The intermetallic peaks remain relatively constant over all temperatures.

5.4.5 WAXS

Midthickness WAXS data is presented as a stacked plot (**Figure A5-13**) and waterfall plot (**Figure A5-14**). Three secondary phases are noted – precipitates θ' and θ (Al_2Cu) and intermetallic ω (Al_7Cu_2Fe). The θ' phase is prominent in the HAZ but peak intensity diminishes toward the stir zone. θ peak intensity increases toward the TMAZ before decreasing in the stir zone. Finally, the ω phase remains relatively constant throughout each weld zone.

5.4.6 Small-angle Neutron Scattering

Representative 2D SANS patterns are presented in **Figure A5-15**. Intensity is slightly asymmetric and observed to decrease from the base metal to the SZ. The TMAZ transition was not discernable owing to the relatively large beam size compared to the expected zone width. Two approaches were used to produce 1D I vs q plots: a simple azimuthal average, **Figure A5-16**, and via assignment of intensity wedges in the horizontal ($\pm$ 15°) and vertical (75-105°) range, **Figure A5-17**.

Asymmetry was confirmed by the intensity difference between the vertical and horizontal wedges. Representative base metal and stir zone patterns from each method were evaluated and are presented in **Figure A5-18**.

The q range of the horizontal wedge was greater than the vertical wedge owing to the larger Q range of the 2D detector in this direction. Intensity differences between the vertical and horizontal methods are insignificant in the stir zone, indicating relatively isotropic scattering for this region. However, in the base metal (and HAZ) the Guinier region is both broader and at a higher intensity for the vertical wedge compared to the horizontal wedge. Interpretation of this difference is hindered by the out of plane texture of the material.

Fitting

Two distinct Guinier regions with a low q power law slope were observed for the base metal and HAZ while a Porod's law slope (characteristic of scattering of sharp interfaces) approximates the stir zone measurements, **Figure A5-19**.

Figure A5-20 compares the radius of gyration (R_g) for each Guinier region (designated as R_g1 at high q and R_g2 at low q) for each averaging strategy. Of note, there were two positions (P11 and P13) which demonstrated a slight increase in intensity at high q. These were not considered as Guinier regions due to poor intensity resolution compared to background and instrument resolution as well as lack of appearance in the vertical wedge average.

On average the azimuthal case R_g values were between the vertical and horizontal with the vertical tending to be lower and horizontal higher, especially in the case of R_g2. The retreating side horizontal R_g2 values were greater than expected with a large degree of error likely due to incongruent data stitching in the retreating side HAZ and BM regions.

Stir Zone Subtraction

A stir zone subtracted intensity was achieved by calculating the difference between each scattering pattern and the averaged scattering intensity of the stir zone measurements. The modified patterns were then fit as above producing consistently lower R_g values (2.2-72.6 nm for R_g1 and 12.4-64 nm for R_g2) compared to azimuthal averaging, **Figure A5-21**. All R_g values are summarized in **Table A5-3**.

Volume Fraction

Neutron scattering contrast was calculated based upon the XRF composition as well as precipitate composition (Al_2Cu) and calculated density for a range of energies using IRENA. The Unified Fit determined invariant and neutron scattering contrast were used along with equation *5-1* to complete this calculation.

$$Q_v = \int_0^\infty I(q)q^2dq = 2\pi^2\left(\rho_p - \rho_m\right)^2 f_v(1 - f_v) \qquad (5\text{-}1)$$

where Q_v is the invariant, I is the intensity, q is the scattering vector, ρ_p and ρ_m are the scattering factor density for the precipitate and matrix, and f_v is the volume fraction. The

resulting relative volume fraction for the individual scattering populations L1 (high q region) and L2 (low q region) is given by **Figure A5-22** and that of the combined fitting levels (L1-L2) in **Figure A5-23**.

The calculated relative volume fraction is observed to decrease through the HAZ toward the stir zone for L1 and increase from the BM to HAZ for L2. The combined L1/L2 relative volume fraction decreases to the SZ.

5.4.7 USAXS/SAXS

The linearly interpolated SAXS summed intensity as a contour plot, **Figure A5-24**, shows a marked decrease in intensity from the BM and HAZ to the SZ. The slit-smeared azimuthal averaged I vs q plots are presented in **Figure A5-25**.

A low q power law slope and four Guinier regions were observed for the base metal and HAZ while a Porod's law slope (characteristic of scattering of sharp interfaces) and a single broad high q Guinier describes the stir zone measurements. The Unified Fit approach produced several R_g over four q ranges or fitting levels (L1-L4), where increasing integer represents a lower q range (e.g. L1 is high q and L4 represents low q), **Figure A5-26**. R_g values for each range were 2.34-5.06 nm for R_g1, 8.9-28.5 nm for R_g2, 50.4-225 nm for R_g3, and 318-640 nm for R_g4. R_g1 increased to the HAZ/TMAZ transition, R_g2 increased to the HAZ before decreasing to a minimum TMAZ and near HAZ/TMAZ transition, R_g3 remained constant in the BM but decreased to the near HAZ/TMAZ transition and TMAZ, and R_g4 decreased toward the SZ where it achieved a minimum.

Comparison

The correlation between microhardness, macroprecipitate number, and raw SAS intensity was explored by normalization as in **Figure A5-27**. Microhardness, macroprecipitate number, and SAS intensity decrease toward the TMAZ/SZ.

Comparison of USAXS/SAXS and SANS Rg values are given in **Figure A5-28**. Rg for L1 and the advancing side L2 was similar in tend and value while the retreating side L2 did not display a clear trend.

5.5 Discussion

5.5.1 Micro-Macrostructure

SRFSW macrostructure was hourglass shaped with and a sharper TMAZ/SZ transition on the advancing side compared to the retreating side. Weld defects were not observed. The BM, HAZ, TMAZ, and SZ were readily distinguished. Grain size increased in the HAZ, elongated in the TMAZ, and became equiaxed in the SZ. Grain size measurements were compared with a similar study of 2219-T87 SRFSW conducted by Anderson, **Table A5-4.** [121] BM and SZ grain size was comparable to that study while the HAZ and TMAZ differences may be attributable to variation in sampled location and/or processing parameters.

Macroprecipitate number and line density decreased toward the stir zone. Macroprecipitates are likely θ (Al_2Cu) due to their large relative size whereas the primary strengthening agent (θ') is frequently too small to be detected in optical microscopy. The decreased presence of these θ precipitates with increased temperature can be indicative of coarsening and/or the relative dissolution of θ' into θ. [58], [96]

5.5.2 Microhardness

Microhardness profiles were "W" and "hourglass" shaped distributions. 2219-T87 FSW microhardness results are directly proportional to macroprecipitate number/density as well as SAS intensity and indirectly proportional to grain size. The lowest microhardness values are observed on the retreating side of the weld aligns with higher expected temperatures on the retreating side compared to the advancing side, resulting in greater precipitate dissolution. [4],[5],[22],[23]

There is a slight recovery of microhardness in the SZ where the macroprecipitate number and density are at their lowest, suggesting that the recovery is at least partially associated with the smaller, equiaxed grain size and/or reprecipitation of fine θ' precipitates. [14], [57]

5.5.3 X-ray Fluorescence (XRF)

XRF provided a baseline composition of the bulk 2219-T87 and comparison to the alloy standard. The composition was well within the compositional limits and served as a basis for the initial aluminum matrix composition assumption that was used to calculate relative volume fraction. Inductively Coupled Plasma Optical Emission spectroscopy (ICP-OES) would offer precision determination of the alloy composition but was not available.

5.5.4 HTXRD

HTXRD data allows identification of significant secondary phases and provides precipitate dissolution temperature ranges prior to the WAXS experiment. Rietveld refinement was undertaken but not completed due to focus on phase identification and difficulties in accurately determining the volume fraction of the θ' phase. This determination was complicated due to the high degree of preferred orientation, broad peak shape, relatively low peak intensity compared to background, competing peak contributions from the Al phase, expectedly low volume fraction (< 5%), and identification of only two distinct peaks belonging to this phase within the measured 2θ range. [138] Therefore, only a qualitative understanding of precipitate evolution is possible.

All secondary phases were observed at 25 °C except for θ" which was not discernable. The precipitate sequence followed expectations with θ‘ transitioning to θ. The ω intermetallic peak intensity did not appreciably change over the temperature range implying relative thermal stability of this phase.

The θ' precipitates are observed over a range of 175-350 °C with dissolution onset around 275-300 °C while θ is primarily present over a higher temperature range (225-475 °C) and dissolution starting around 400 °C. The θ' peaks are broad inferring a small particle size but narrow slightly with increasing temperature, presumably as the particle coarsens. θ' peak intensity increases (175-225 °C) are comparable to the formation temperature (224 °C) reported by Kang et al in study of a 2219-T8 FSW, however, this is

not the case for θ which highlights limitations of comparing differing heating rates, tempers/ageing, and techniques. [58]

Of these factors, the primary limitation of this study is increased heat exposure due to the holding at a constant temperature for the duration of each measurement compared to a typical Differential Scanning Calorimetry (DSC) experiment. Therefore, this experiment serves only as an estimation of the temperature ranges at which these precipitates evolve or retain stability during the SRFSW process. Papazian elucidates, "The dissolution rate of GP zones and θ', and the formation rate of θ' and θ are dominated by their reaction kinetics during a DSC run, but that the dissolution rate of θ is dominated by its temperature dependent thermodynamic equilibrium. Thus, whereas the θ dissolution occurs at the same temperature regardless of the imposed heating rate, the other reactions occur at systematically higher temperatures when sufficient time is not allowed by the more rapid heating rates." [139]

Other potential sources of error in transition temperature determination are related to discrepancies between the programmed set temperatures and those measured, **Figure A5-29**. Both temperature values at the low end (175-250 °C) and high end (425-500 °C) of the temperature range saw temperatures exceed those programmed by 3-7 °C with higher temperatures overshooting toward the high end of that range. Additionally, differences in heating rate and time-at-temperature are observed between the high and low temperature regions with the low temperature region possessing lower heating rates (~18 °C/min compared to ~48 °C/min) and less time-at-temperature compared to the high temperature region. These factors rule out direction comparison between studies.

5.5.5 WAXS

Complementary study with WAXS provides phase identification and evolution across the SRFSW. WAXS data confirms the presence of three secondary phases – the precipitates θ' and θ (Al_2Cu) and intermetallic ω (Al_7Cu_2Fe). Only qualitative analysis of the WAXS data is possible though distinct trends in volume fraction evolution can be inferred based upon relative peak intensity. In these terms, the highest concentration of θ' and θ precipitates lie in the HAZ and thermomechanically affected zone (TMAZ), respectively,

while both reach a minimum concentration in the stir zone. Reprecipitation of θ' at some locations in the SZ is indicated by peak presence and supports this as the likely cause of microhardness recovery in this region. As in the HTXRD data, the θ' peak is broad in the base metal but sharpens considerably in the HAZ potentially indicating particle coarsening prior to dissolution. The intermetallic peak intensity is overall stable. These observations agree with other studies of 2219 and similar processes such as FSW. [58]

5.5.6 Small-angle Scattering

The azimuthally averaged SANS data showed two Guinier scattering regions which the radius of gyration (R_g) was 29-67 Å for Rg1 and 162-478 Å for Rg2 with USAXS/SAXS data showing comparable results. Differences between the SANS and USAXS/SAXS data can be partially attributed to the decreased specificity of SANS due to a considerably larger sampled area, increased uncertainty at high q, and slightly different sample location.

Using the simplified assumption that the scatterers are monodisperse spherical particles (equation 5-2),

$$R_g^2 = \frac{3}{5}R^2 \tag{5-2}$$

where Rg is the radius of gyration and R is the particle radius, produces 37.439-86.497 Å (3.74-8.65 nm) for Rg1 and 209.14-617.10 Å (20.91-61.71 nm) for Rg2. This indicates the predicted scatterer size range for direct TEM observation and characterization. Prior studies on precipitate size along with HTXRD and WAXS data presented here suggest θ' as the dominant scatterer for L1 and L2 (i.e. Rg1 and Rg2) though convolution from small θ precipitates is not discounted. The identity of the L3 scatterer is uncertain while L4 is likely to be θ due to decreased size in the SZ and lack of complete dissolution.

The raw SANS/SAXS and summed SAXS intensity indicate a loss of scatterer population towards the SZ and likely decreased in volume fraction. The invariant, Q_V, decreases toward the SZ for L1 and increases toward the SZ for L2 though the combined L1 and L2 levels show a decreased relative volume fraction toward the SZ. There are two possible interpretations; either that L1 level represents the θ' precipitates while L2 describes the θ

precipitates or more likely both L1 and L2 describe the θ’ precipitates and the relative volume fraction decreases toward the stir zone. Both interpretations have merit as the WAXS data suggests volume fraction toward the SZ decreases for θ’ and increases for θ. The semi-quantitative volume fraction is likely overestimated but indicative of overall trends. **[citation]** Direct observation of the precipitates is therefore required for complete interpretation.

5.6 Conclusion

Precipitation of 2219-T87 SRFSW was evaluated via complementary characterization techniques in terms of morphology, size, density, thermal characteristics, density, and relative volume fraction. HTXRD suggests coarsening and dissolution of fine θ’ precipitates and overageing of the larger θ precipitates to temperatures approximating the SZ. WAXS corroborates the HTXRD findings where θ’ peaks decrease to the TMAZ with some scattered peak intensity in the SZ suggesting reprecipitation while θ peak intensity increases in the HAZ and decreases to the SZ though without full dissolution. Small-angle scattering (SANS and SAXS) were employed to determine precipitate size, morphology, and relative volume fraction. Morphology was determined to be a disc/platelet. Two Guinier regions were observed in the SANS data and four Guinier regions for the USAXS/SAXS data. The high q scattering levels (L1 and L2) were determined to be related to the θ’ precipitates with size ranges of 2-9 nm and 20-61 nm depending on averaging strategy. Relative volume fraction was qualitatively interpreted to decrease in proportion to raw and summed intensity toward the SZ for the SANS/SAXS data. The invariant for both fitting levels was used to produce a semi-quantitative volume fraction which decreased toward the stir zone.

Corroboration of precipitate morphology, identity, and volume fraction will be conducted via TEM and APT experiments.

5.7 Acknowledgements

The authors would like to acknowledge partial support though the Manufacturing and Materials Joining Innovation Center (Ma^2JIC) University of Tennessee, Knoxville site. Ma^2JIC is funded by the National Science Foundation (NSF) through the

Industry/University Cooperative Research Center (I/UCRC) program award number IIP 1822186. This research used resources at the High Flux Isotope Reactor a DOE Office of Science User Facility operated by the Oak Ridge National Laboratory. This research used resources of the Advanced Photon Source, a U.S. Department of Energy (DOE) Office of Science user facility operated for the DOE Office of Science by Argonne National Laboratory under Contract No. DE-AC02-06CH11357. X-ray diffraction was performed at the Institute for Advanced Materials and Manufacturing (IAMM) Diffraction Facility, located at the University of Tennessee, Knoxville.

The authors would like to thank John Bohling for preparation of USAXS/SAXS/WAXS sample and Kevin Sisco for his assistance in microhardness testing.

Appendix

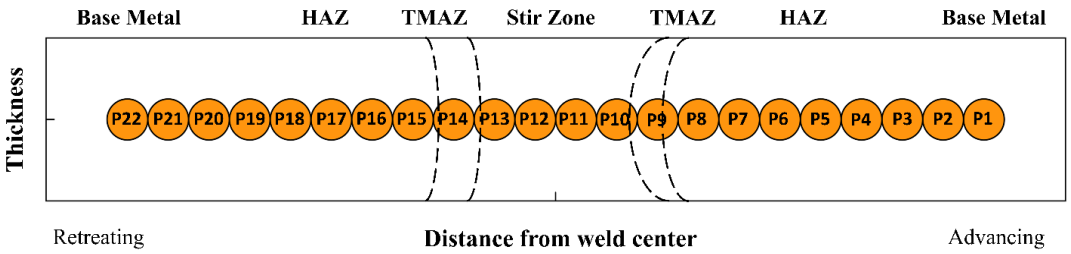

Figure A5-1 SANS measurement scheme with approximate weld zone locations

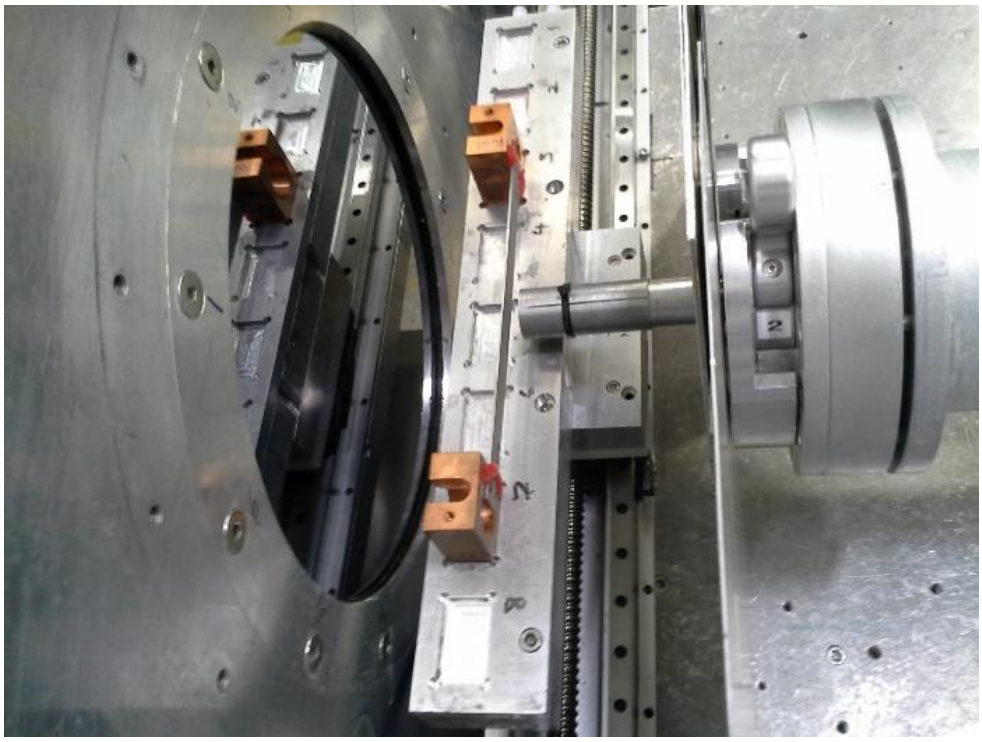

Figure A5-2 GP-SANS experiment setup

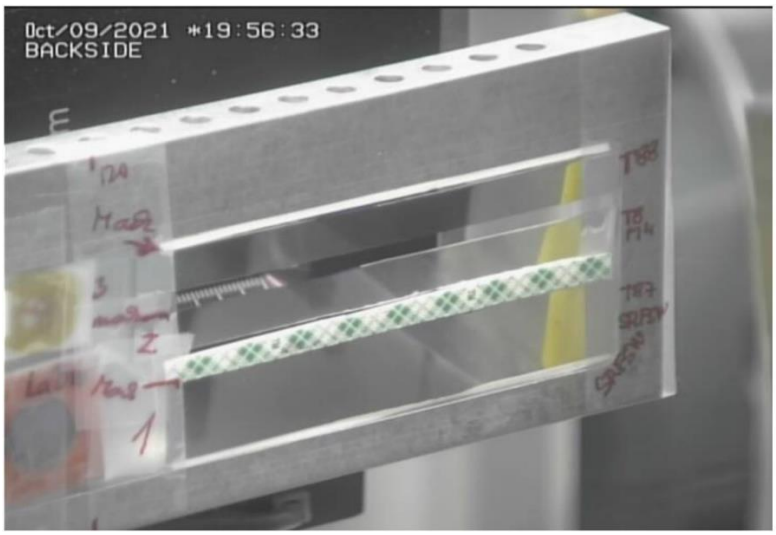

Figure A5-3 USAXS/SAXS/WAXS experiment setup

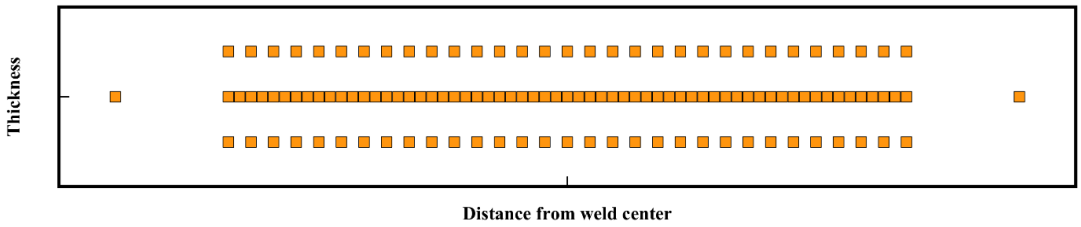

Figure A5-4 USAXS/SAXS/WAXS measurement scheme



Figure A5-5 2219-T87 SRFSW macrograph

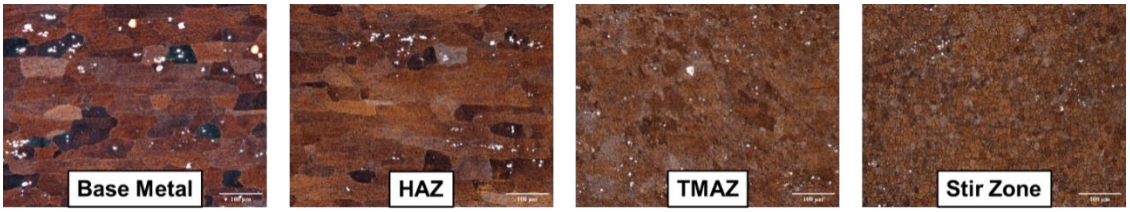

Figure A5-6 Micrographs of each weld zone in 2219-T87 SRFSW

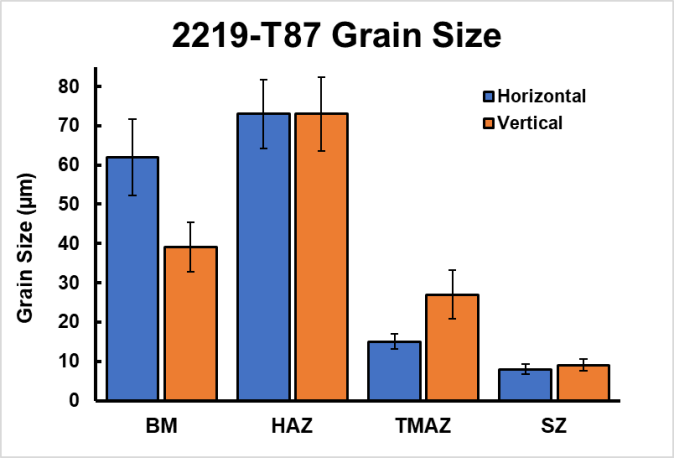

Figure A5-7 Horizontal and vertical grain sizes for each weld zone with standard deviation

Table A5-1: Image analysis of macroprecipitates from optical micrographs - number and linear number density for each weld zone is given

Weld Zone	Precipitate Number	Average Precipitate Number	Precipitate Density (#/µm)	Average Precipitate Density (#/µm)
Base Metal	115	107.33	.3496	.3263
	104		.31616	
	103		.31312	
HAZ	83	88.67	.25232	.2695
	93		.28272	
	90		.2736	
TMAZ	50	49.33	.152	.1500
	54		.16416	
	44		.13376	
Stir Zone	28	35.67	.08512	.1084
	42		.12768	
	37		.11248	

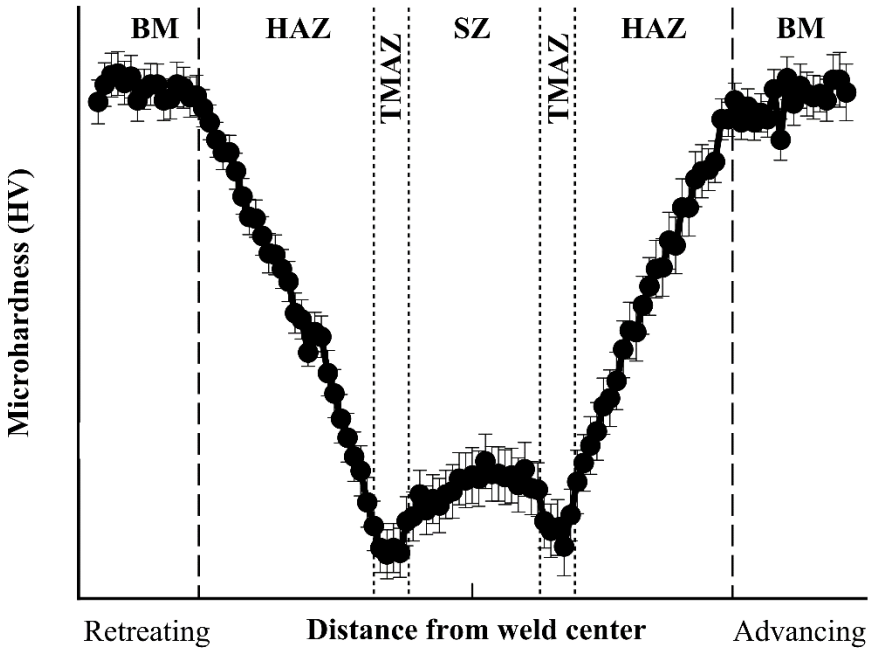

Figure A5-8 Mid-thickness averaged line microhardness (1σ error bars)

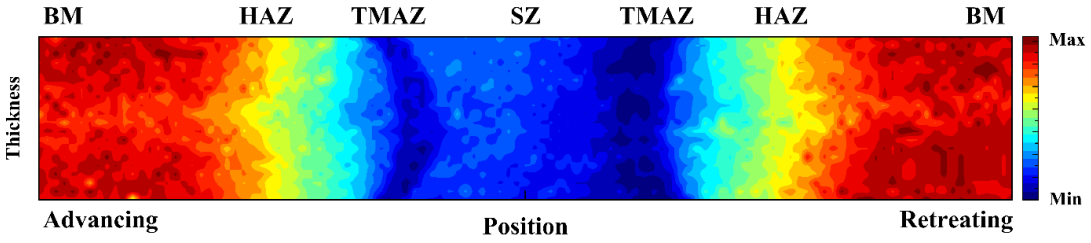

Figure A5-9 Microhardness contour plot

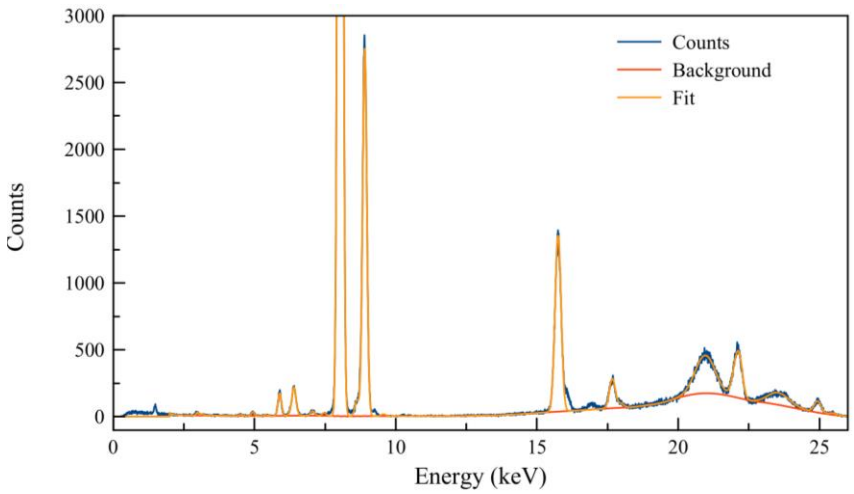

Figure A5-10 Fitted XRF spectra of the 2219-T87 base metal

Table A5-2: Composition of 2219-T87 base metal measured via XRF and 2219 composition limits (wt%) [5]

Element	Al	Cu	Fe	Mg	Mn	Si	Ti	V	Zn	Zr	Other
Limits	91.5-93.8	5.8-6.8	.3 max	.02 max	.2-.4	.2 max	.02-.1	.01-.15	.1 max	.1-.25	.15 max .05 max each
Measured	92.664	6.527	.173	*	.209	.114	.03867	.09651	.03148	.134	.0122(Ni)

* Magnesium concentration is unable to be detected by the instrument and is not reported.

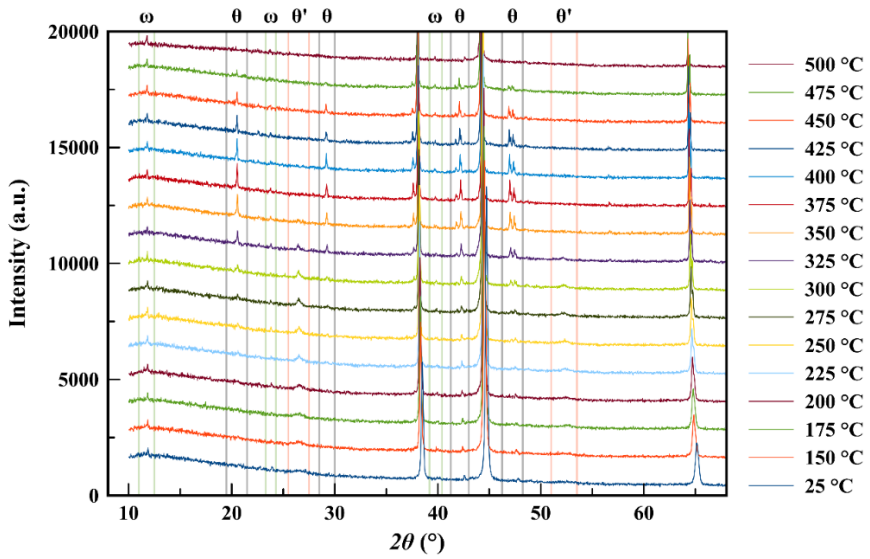

Figure A5-11 Stacked plot of 2219-T87 HTXRD data with secondary phases (ω, θ, and θ') noted

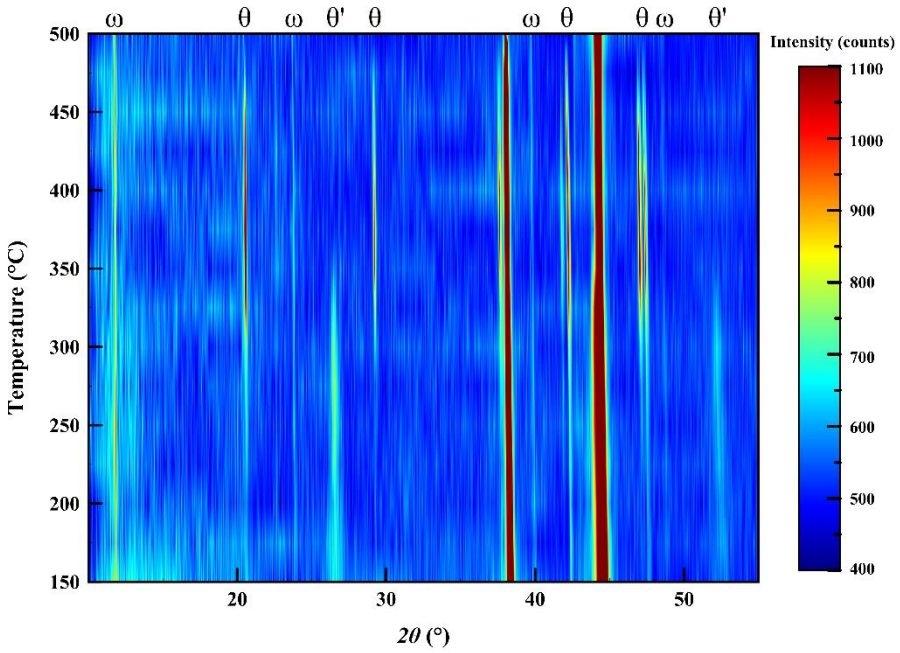

Figure A5-12 Waterfall plot of background subtracted 2219-T87 HTXRD data indicating secondary phases

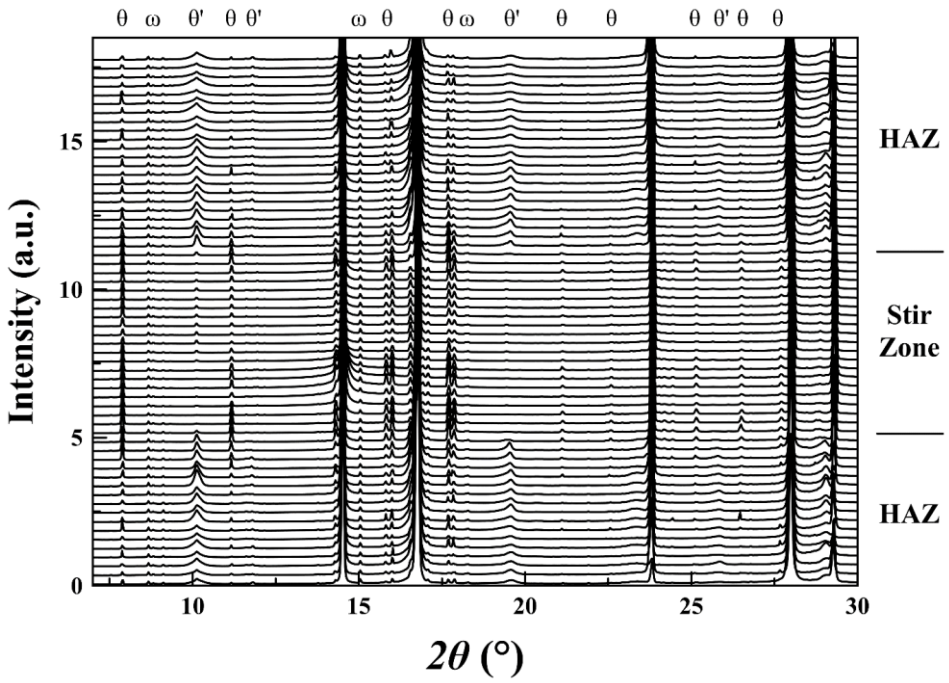

Figure A5-13 Stacked plot of WAXS data with secondary phases (ω, θ, and θ') noted

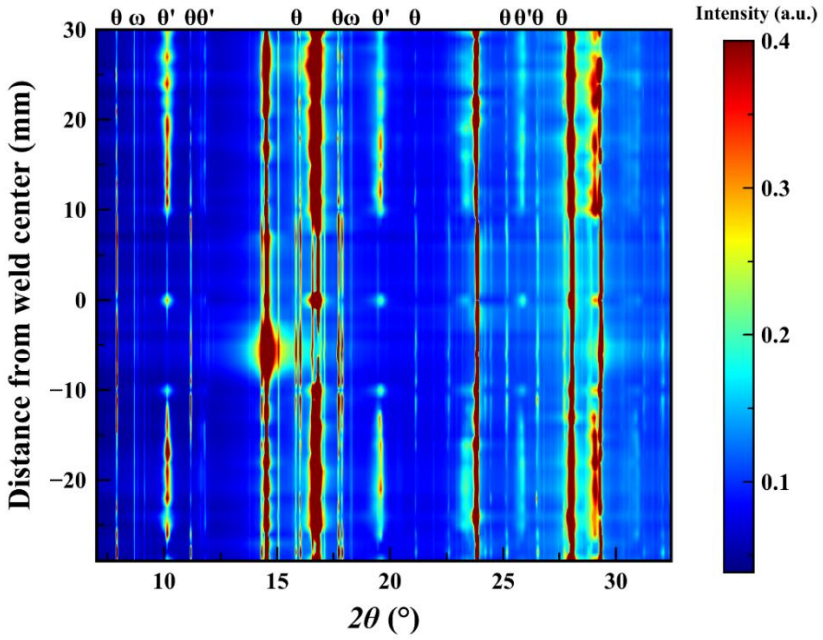

Figure A5-14 Waterfall plot of midthickness WAXS showing intensity related to position and 2θ with secondary phases noted

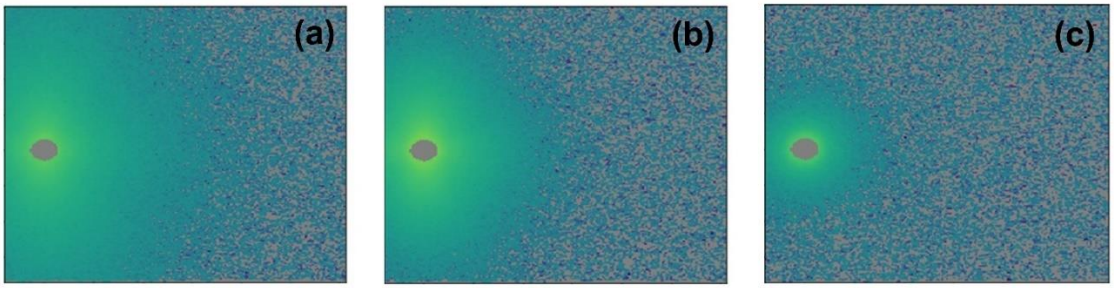

Figure A5-15 2D SANS patterns of 2219-T87 SRFSW for the (a) base metal, (b) HAZ, and (c) stir zone

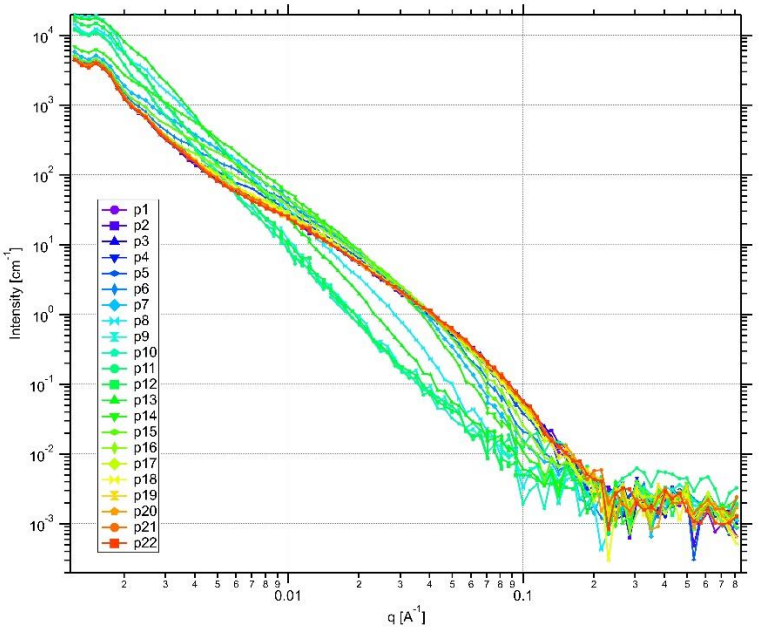

Figure A5-16 Azimuthally averaged SANS I vs q plots

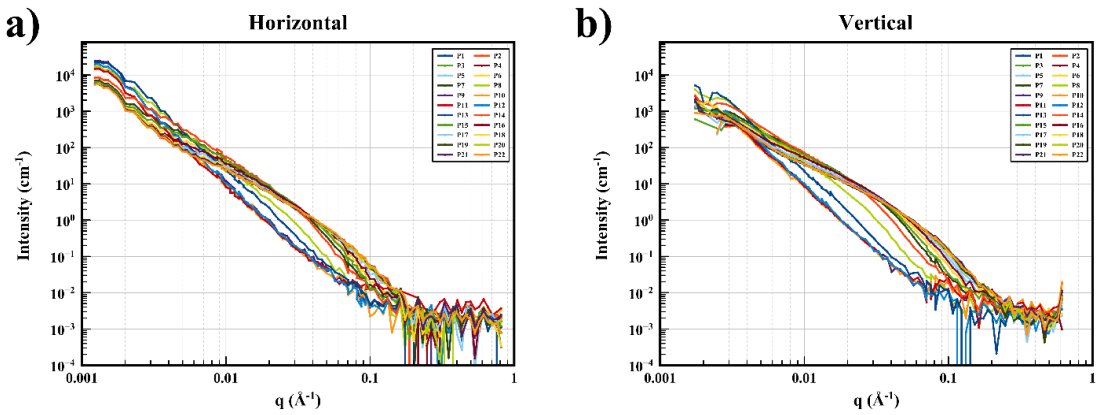

Figure A5-17 SANS I vs q plots for (a) horizontal and (b) vertical wedges

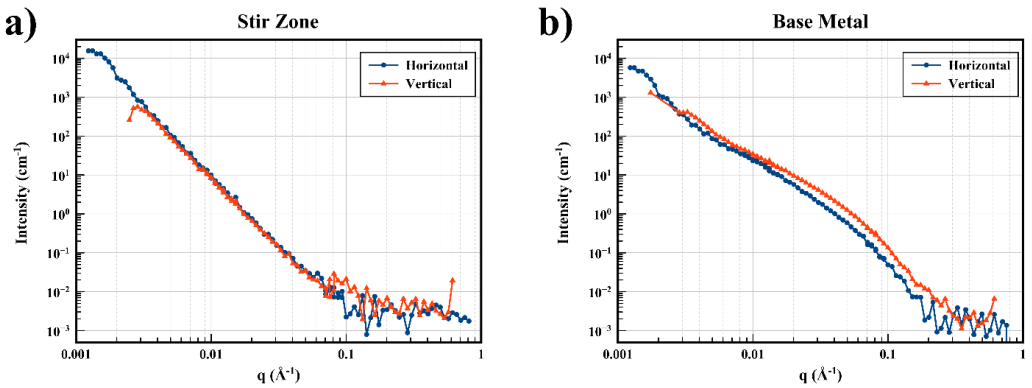

Figure A5-18 SANS I vs q plots comparing the horizontal and vertical wedge schemes (a) SZ and (b) BM

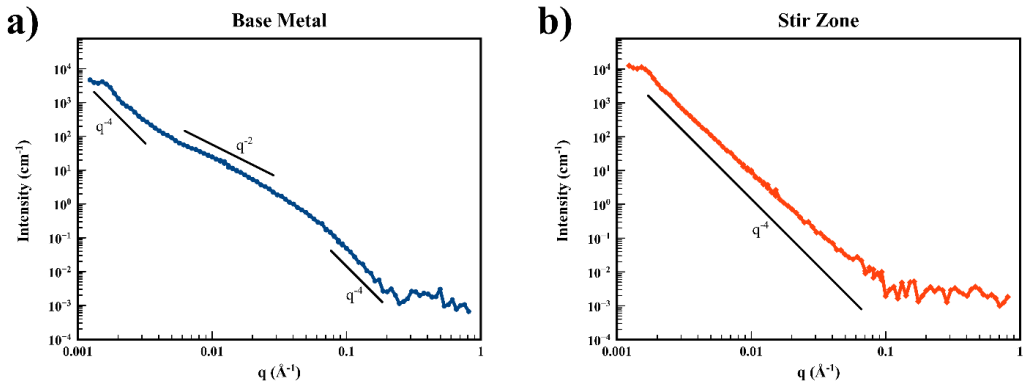

Figure A5-19 Fitting regions of the base metal and stir zone

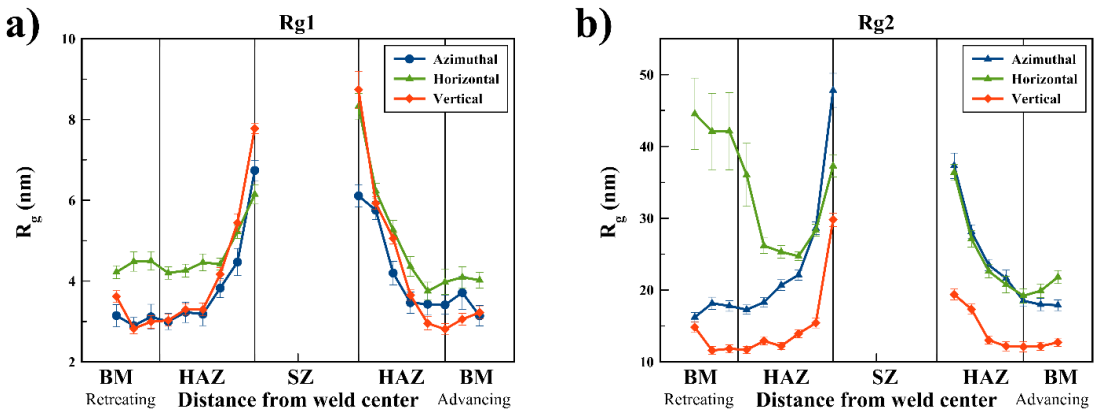

Figure A5-20 Comparison of Rg values for each averaging strategy (a) Rg1 and (b) Rg2

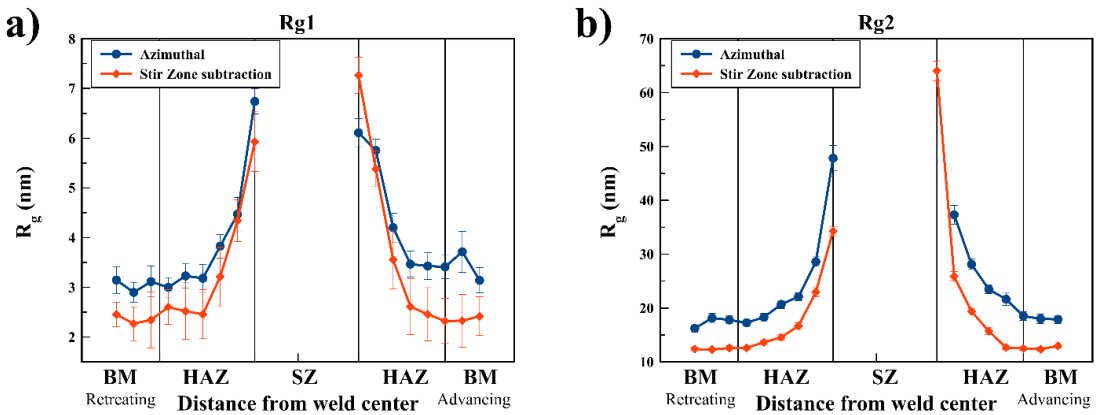

Figure A5-21 Rg comparison for azimuthal and stir zone subtraction methods (a) Rg1 and (b) Rg2

Table A5-3: R_g values for each averaging approach

	Rg1 (nm)	Rg2 (nm)
Azimuthal	2.89-6.74	16.2-47.8
Horizontal	3.75-8.32	19.2-44.5
Vertical	2.82-8.74	11.5-29.7
Stir Zone Subtraction	2.27-7.26	12.37-64

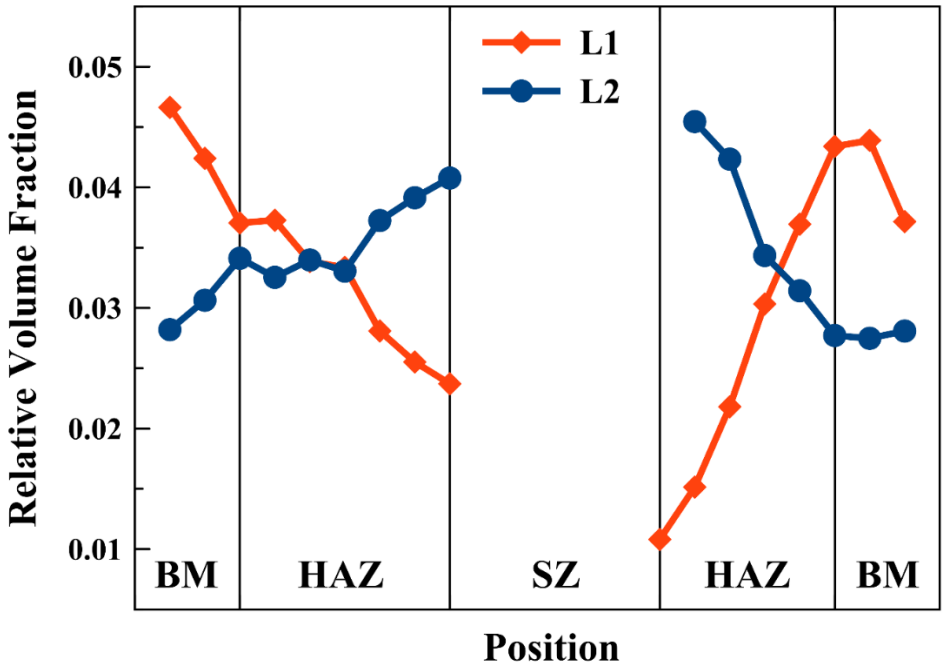

Figure A5-22 Relative volume fraction of the L1 and L2 scattering populations (3 point moving average)

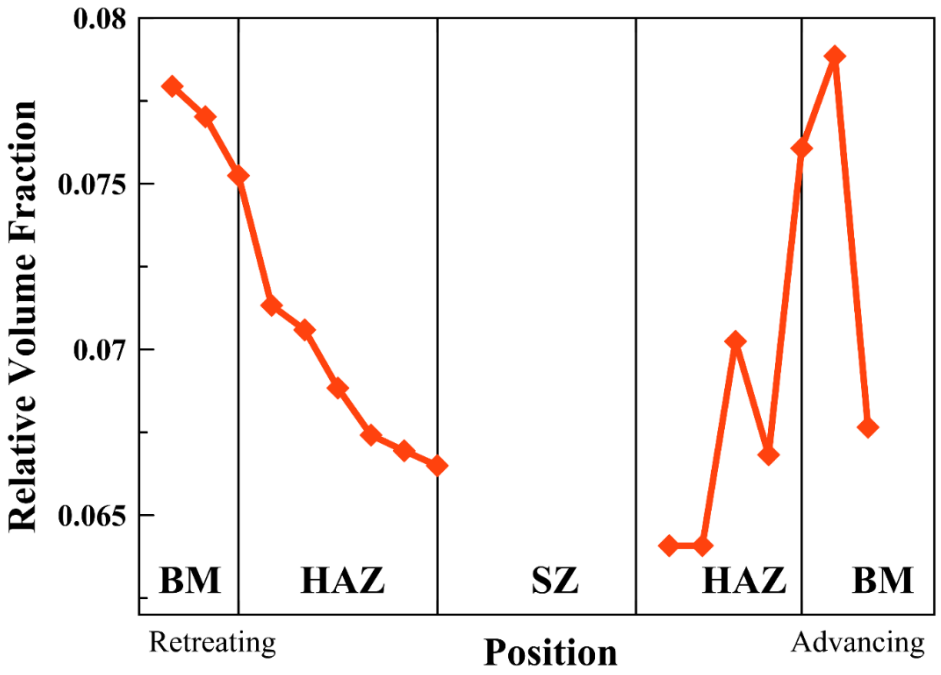

Figure A5-23 Relative volume fraction of the combined fitting levels (L1 and L2)

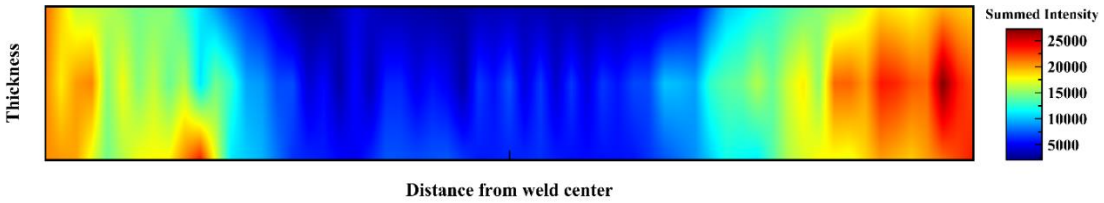

Figure A5-24 2219-T87 SRFSW SAXS summed intensity

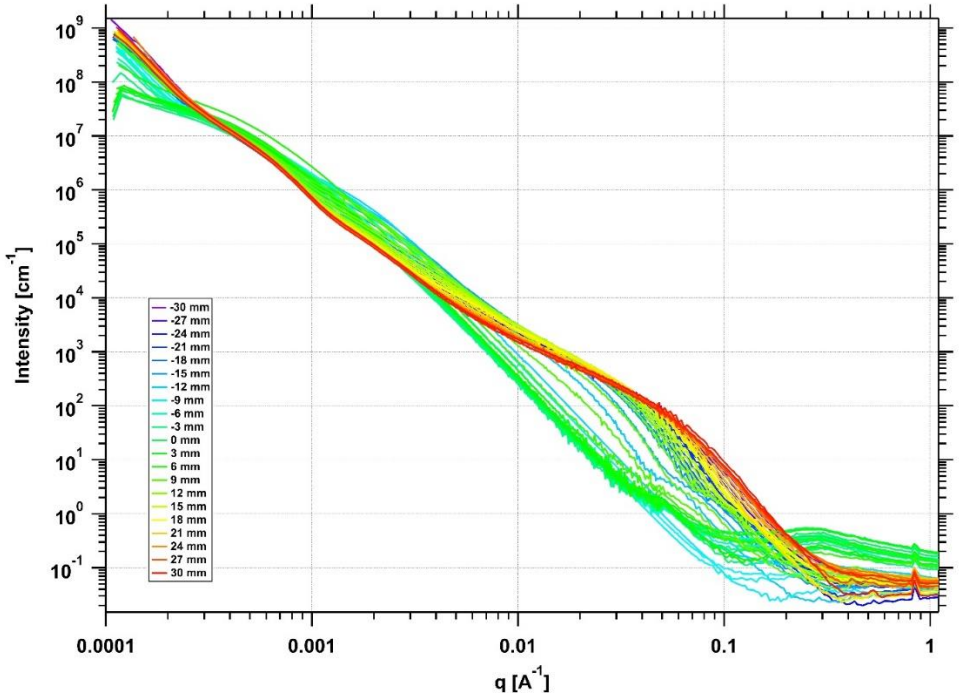

Figure A5-25 Slit-smeared USAXS/SAXS/WAXS I vs q plots at weld midthickness

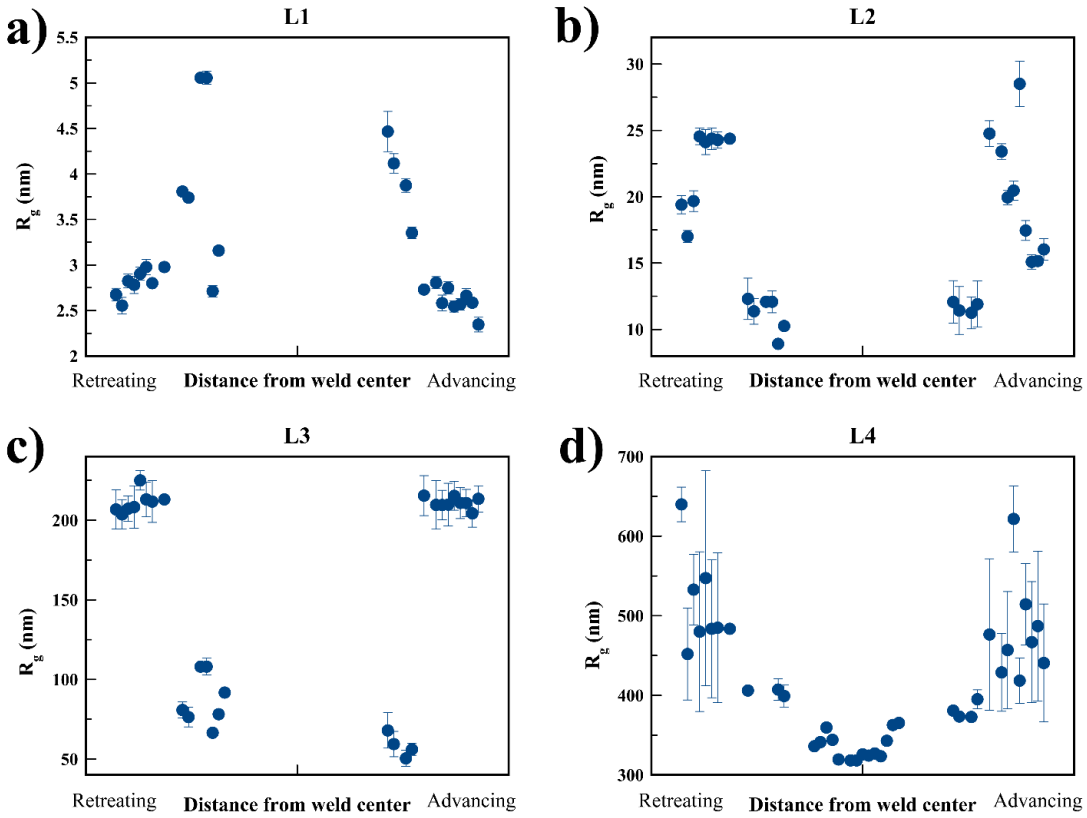

Figure A5-26 Midline USAXS/SAXS radius of gyration for (a) L1, (b) L2, (c) L3, and (d) L4

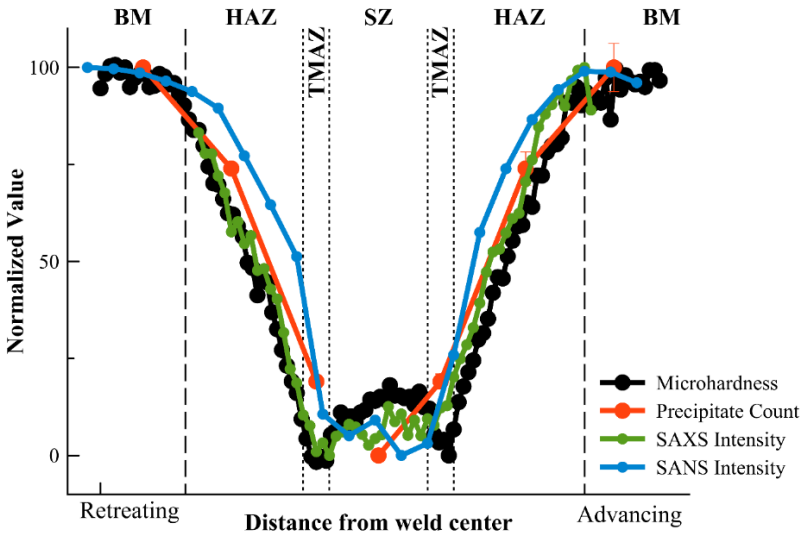

Figure A5-27 Normalized microhardness, macroprecipitate number, SAXS intensity, and SANS intensity correlation

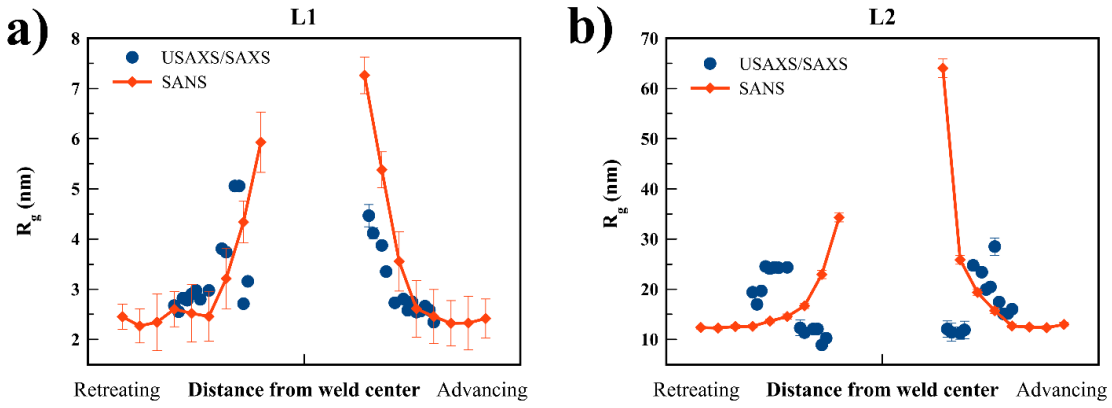

Figure A5-28 Comparison of midline USAXS/SAXS AND SANS radius of gyration (a) L1 and (b) L2

Table A5-4: Grain size comparison for 2219-T87 SRFSW

	Horizontal		Vertical	
	Measured	**Anderson**	**Measured**	**Anderson**
Base Metal	62 ± 9.7	49 ± 14.1	39 ± 6.3	26 ± 2.3
HAZ	73 ± 8.8	66 ± 6.9	73 ± 9.4	28 ± 1.6
TMAZ	15 ± 1.9	90 ± 5.6	27 ± 6.2	59 ± 7.9
Stir Zone	8 ± 1.2	8-12 ± 0.3-0.5	9 ± 1.5	8-12 ± 0.3-0.5

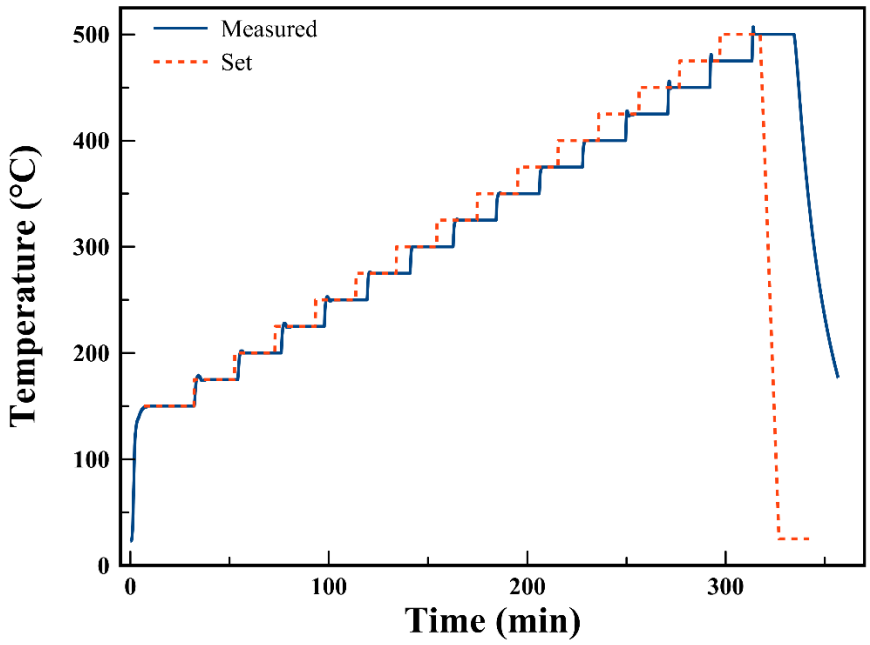

Figure A5-29 2219-T87 HTXRD experiment temperature vs time profile

REFERENCES

[1] J. R. Davis & Associates and ASM International, Eds., *Aluminum and aluminum alloys*. in ASM specialty handbook. Materials Park, OH: ASM International, 1993.

[2] J. G. Kaufman, *Introduction to aluminum alloys and tempers*. Materials Park, OH: ASM International, 2000.

[3] G. E. Dieter, *Mechanical metallurgy*, 3rd ed. in McGraw-Hill series in materials science and engineering. New York: McGraw-Hill, 1986.

[4] T. H. Courtney, *Mechanical behavior of materials*, 2. ed. Long Grove, Illinois: Waveland Press, 2005.

[5] K. Anderson, J. Weritz, and J. G. Kaufman, Eds., "2219 and Alclad 2219: High-Temperature Alloy," in *Properties and Selection of Aluminum Alloys*, ASM International, 2019, pp. 319–322. doi: 10.31399/asm.hb.v02b.a0006611.

[6] M. Niedzinski, "The Evolution of Constellium Al-Li Alloys for Space Launch and Crew Module Applications," Feb. 11, 2019. [Online]. Available: https://www.lightmetalage.com/news/industry-news/aerospace/article-the-evolution-of-constellium-al-li-alloys-for-space-launch-and-crew-module-applications/

[7] NASA MSFC, "Space Launch System Core Stage." Apr. 27, 2021. [Online]. Available: https://www.nasa.gov/sites/default/files/atoms/files/sls_core_stage_fact_sheet_04262021_508.pdf

[8] J. C. Pilet, D. Diecidue-Conners, M. Worden, M. Guillot, and K. Welzyn, "External Tank Program - Legacy of Success," presented at the AIAA Space 2011 Conference and Exposition, Long Beach, CA, Sep. 2011, p. 51. [Online]. Available: https://ntrs.nasa.gov/api/citations/20120001570/downloads/20120001570.pdf

[9] D. S. MacKenzie, "Metallurgy of Heat Treatable Aluminum Alloys," in *Heat Treating of Nonferrous Alloys*, G. E. Totten, Ed., ASM International, 2016, pp. 65–113. doi: 10.31399/asm.hb.v04e.a0006287.

[10] American National Standard Institue (ANSI), "ANSI H35.1/H35.1M-2017: Alloy and Temper Designation Systems for Aluminum." 2017.

[11] Kaiser Aluminum & Chemical Sales, Inc, *Welding Kaiser Aluminum*, 1st ed. 1967.

[12] R. J. Rioja and J. Liu, "The Evolution of Al-Li Base Products for Aerospace and Space Applications," *Metall and Mat Trans A*, vol. 43, no. 9, pp. 3325–3337, Sep. 2012, doi: 10.1007/s11661-012-1155-z.

[13] K. Anderson, J. Weritz, and J. G. Kaufman, Eds., "2195: Al-Li Plate Alloy," in *Properties and Selection of Aluminum Alloys*, ASM International, 2019, pp. 316–316. doi: 10.31399/asm.hb.v02b.a0006608.

[14] P. L. Threadgill, A. J. Leonard, H. R. Shercliff, and P. J. Withers, "Friction stir welding of aluminium alloys," *International Materials Reviews*, vol. 54, no. 2, pp. 49–93, Mar. 2009, doi: 10.1179/174328009X411136.

[15] R. S. Mishra and Z. Y. Ma, "Friction stir welding and processing," *Materials Science and Engineering: R: Reports*, vol. 50, no. 1–2, pp. 1–78, Aug. 2005, doi: 10.1016/j.mser.2005.07.001.

[16] A. Heidarzadeh *et al.*, “Friction stir welding/processing of metals and alloys: A comprehensive review on microstructural evolution,” *Progress in Materials Science*, vol. 117, p. 100752, Apr. 2021, doi: 10.1016/j.pmatsci.2020.100752.
[17] J. Defalco, “Friction stir welding vs. fusion welding,” *Weld. j*, vol. 85, no. 3, pp. 42–44, 2006.
[18] S. Malarvizhi and V. Balasubramanian, “Fatigue crack growth resistance of gas tungsten arc, electron beam and friction stir welded joints of AA2219 aluminium alloy,” *Materials & Design*, vol. 32, no. 3, pp. 1205–1214, Mar. 2011, doi: 10.1016/j.matdes.2010.10.019.
[19] S. Malarvizhi and V. Balasubramanian, “Effect of welding processes on AA2219 aluminium alloy joint properties,” *Transactions of Nonferrous Metals Society of China*, vol. 21, no. 5, pp. 962–973, May 2011, doi: 10.1016/S1003-6326(11)60808-X.
[20] P. L. Threadgill and A. J. Leonard, “Macro and Microstructural Features of Friction Stir Welds in Various Materials,” TWI, Abington, UK, TWI members report 693/1999, 1999.
[21] P. Sadeesh *et al.*, “Studies on Friction Stir Welding of AA 2024 and AA 6061 Dissimilar Metals,” *Procedia Engineering*, vol. 75, pp. 145–149, 2014, doi: 10.1016/j.proeng.2013.11.031.
[22] J. H. Ouyang and R. Kovacevic, “Material flow and microstructure in the friction stir butt welds of the same and dissimilar aluminum alloys,” *J. of Materi Eng and Perform*, vol. 11, no. 1, pp. 51–63, Feb. 2002, doi: 10.1007/s11665-002-0008-0.
[23] A. Simar and M.-N. Avettand-Fènoël, “State of the art about dissimilar metal friction stir welding,” *Science and Technology of Welding and Joining*, vol. 22, no. 5, pp. 389–403, Jul. 2017, doi: 10.1080/13621718.2016.1251712.
[24] K. Fuse and V. Badheka, “Bobbin tool friction stir welding: a review,” *Science and Technology of Welding and Joining*, vol. 24, no. 4, pp. 277–304, May 2019, doi: 10.1080/13621718.2018.1553655.
[25] G.-Q. Wang, Y.-H. Zhao, and Y.-Y. Tang, “Research Progress of Bobbin Tool Friction Stir Welding of Aluminum Alloys: A Review,” *Acta Metall. Sin. (Engl. Lett.)*, vol. 33, no. 1, pp. 13–29, Jan. 2020, doi: 10.1007/s40195-019-00946-8.
[26] P. J. Withers and H. K. D. H. Bhadeshia, “Residual stress. Part 2 – Nature and origins,” *Materials Science and Technology*, vol. 17, no. 4, pp. 366–375, Apr. 2001, doi: 10.1179/026708301101510087.
[27] N. S. Rossini, M. Dassisti, K. Y. Benyounis, and A. G. Olabi, “Methods of measuring residual stresses in components,” *Materials & Design*, vol. 35, pp. 572–588, Mar. 2012, doi: 10.1016/j.matdes.2011.08.022.
[28] A. D. Krawitz, *Introduction to diffraction in materials, science, and engineering*. New York: John Wiley, 2001.
[29] E. Kula and V. Weiss, Eds., *Residual Stress and Stress Relaxation*. Boston, MA: Springer US, 1982. doi: 10.1007/978-1-4899-1884-0.
[30] M. T. Hutchings, Ed., *Introduction to the characterization of residual stress by neutron diffraction*. Boca Raton, FL: Taylor & Francis, 2005.
[31] S. Kou, *Welding metallurgy*, 2nd ed. Hoboken, N.J: Wiley-Interscience, 2003.

[32] K. Masubuchi, “Residual Stresses and Distortion,” in *Welding, Brazing, and Soldering*, D. L. Olson, T. A. Siewert, S. Liu, and G. R. Edwards, Eds., ASM International, 1993, pp. 1094–1102. doi: 10.31399/asm.hb.v06.a0001475.
[33] F. A. Kandil, J. D. Lord, A. T. Fry, and P. Grant, “A review of residual stress measurement methods - a guide to technique selection.,” 2001.
[34] J. Guo, H. Fu, B. Pan, and R. Kang, “Recent progress of residual stress measurement methods: A review,” *Chinese Journal of Aeronautics*, vol. 34, no. 2, pp. 54–78, Feb. 2021, doi: 10.1016/j.cja.2019.10.010.
[35] W. Woo, Z. Feng, X. Wang, and S. A. David, “Neutron diffraction measurements of residual stresses in friction stir welding: a review,” *Science and Technology of Welding and Joining*, vol. 16, no. 1, pp. 23–32, Jan. 2011, doi: 10.1179/136217110X12731414739916.
[36] X.-L. Wang, S. Spooner, and C. R. Hubbard, “Theory of the Peak Shift Anomaly due to Partial Burial of the Sampling Volume in Neutron Diffraction Residual Stress Measurements,” *J Appl Crystallogr*, vol. 31, no. 1, pp. 52–59, Feb. 1998, doi: 10.1107/S0021889897008261.
[37] G. A. Webster, “Polycrystalline materials - Determinations of residual stresses by neutron diffraction,” *ISO/TTA3 Technology Trends Assessment*, vol. Geneva, 2001.
[38] L. Vegard, “Die Konstitution der Mischkristalle und die Raumfüllung der Atome,” *Z. Physik*, vol. 5, no. 1, pp. 17–26, Jan. 1921, doi: 10.1007/BF01349680.
[39] H. Jamshidi Aval, “Microstructure and residual stress distributions in friction stir welding of dissimilar aluminium alloys,” *Materials & Design*, vol. 87, pp. 405–413, Dec. 2015, doi: 10.1016/j.matdes.2015.08.050.
[40] J. Altenkirch, A. Steuwer, M. Peel, D. G. Richards, and P. J. Withers, “The effect of tensioning and sectioning on residual stresses in aluminium AA7749 friction stir welds,” *Materials Science and Engineering: A*, vol. 488, no. 1–2, pp. 16–24, Aug. 2008, doi: 10.1016/j.msea.2007.10.055.
[41] M. Prime, T. Gnaupelherold, J. Baumann, R. Lederich, D. Bowden, and R. Sebring, “Residual stress measurements in a thick, dissimilar aluminum alloy friction stir weld,” *Acta Materialia*, vol. 54, no. 15, pp. 4013–4021, Sep. 2006, doi: 10.1016/j.actamat.2006.04.034.
[42] R. P. Martukanitz, P. R. Howell, E. A. Payzant, S. Spooner, and C. R. Hubbard, “Neutron diffraction studies of welds of aerospace aluminum alloys,” Oak Ridge National Lab.(ORNL), Oak Ridge, TN (United States), 1996.
[43] G. Albertini, G. Bruno, B. D. Dunn, F. Fiori, W. Reimers, and J. S. Wright, “Comparative neutron and X-ray residual stress measurements on Al-2219 welded plate,” *Materials Science and Engineering: A*, vol. 224, no. 1–2, pp. 157–165, Mar. 1997, doi: 10.1016/S0921-5093(96)10546-3.
[44] W. Xu, J. Liu, and H. Zhu, “Analysis of residual stresses in thick aluminum friction stir welded butt joints,” *Materials & Design*, vol. 32, no. 4, pp. 2000–2005, Apr. 2011, doi: 10.1016/j.matdes.2010.11.062.
[45] A. Wilm, “Physikalisch-metallurgische Untersuchungen über magnesiumhaltige Aluminiumlegierungen,” *Metallurgie: Zeitschrift für de gesamte Hüttenkunde*, vol. 8, no. 8, pp. 225–227, 1911.

[46] D. S. MacKenzie, “Metallurgy of Heat Treatable Aluminum Alloys,” in *Aluminum Science and Technology*, K. Anderson, J. Weritz, and J. G. Kaufman, Eds., ASM International, 2018, pp. 411–437. doi: 10.31399/asm.hb.v02a.a0006509.
[47] W. D. Callister and D. G. Rethwisch, *Materials science and engineering: an introduction*, 9th edition. Hoboken, NJ: Wiley, 2014.
[48] A. Biswas, D. J. Siegel, C. Wolverton, and D. N. Seidman, “Precipitates in Al–Cu alloys revisited: Atom-probe tomographic experiments and first-principles calculations of compositional evolution and interfacial segregation,” *Acta Materialia*, vol. 59, no. 15, pp. 6187–6204, Sep. 2011, doi: 10.1016/j.actamat.2011.06.036.
[49] J. M. Silcock and T. J. Heal, “The θ’ structure in aluminium–copper alloys,” *Acta Cryst*, vol. 9, no. 8, pp. 680–680, Aug. 1956, doi: 10.1107/S0365110X56001820.
[50] M. Natan and R. A. Chihoski, “Relationship between microstructure, hardness and electrical conductivity of 2219 aluminium,” *J Mater Sci*, vol. 18, no. 11, pp. 3288–3298, Nov. 1983, doi: 10.1007/BF00544153.
[51] Y. C. Chen, J. C. Feng, and H. J. Liu, “Precipitate evolution in friction stir welding of 2219-T6 aluminum alloys,” *Materials Characterization*, vol. 60, no. 6, pp. 476–481, Jun. 2009, doi: 10.1016/j.matchar.2008.12.002.
[52] J. Kang, Z.-C. Feng, G. S. Frankel, I. W. Huang, G.-Q. Wang, and A.-P. Wu, “Friction Stir Welding of Al Alloy 2219-T8: Part I-Evolution of Precipitates and Formation of Abnormal Al2Cu Agglomerates,” *Metall and Mat Trans A*, vol. 47, no. 9, pp. 4553–4565, Sep. 2016, doi: 10.1007/s11661-016-3648-7.
[53] R. W. Fonda and J. F. Bingert, “Precipitation and grain refinement in a 2195 Al friction stir weld,” *Metall and Mat Trans A*, vol. 37, no. 12, pp. 3593–3604, Dec. 2006, doi: 10.1007/s11661-006-1054-2.
[54] R. Yoshimura, T. J. Konno, E. Abe, and K. Hiraga, “Transmission electron microscopy study of the evolution of precipitates in aged Al–Li–Cu alloys: the θ′ and T1 phases,” *Acta Materialia*, vol. 51, no. 14, pp. 4251–4266, Aug. 2003, doi: 10.1016/S1359-6454(03)00253-2.
[55] C. Sigli, F. De Geuser, A. Deschamps, J. Lépinoux, and M. Perez, “Recent advances in the metallurgy of aluminum alloys. Part II: Age hardening,” *Comptes Rendus Physique*, vol. 19, no. 8, pp. 688–709, Dec. 2018, doi: 10.1016/j.crhy.2018.10.012.
[56] E. Gumbmann, W. Lefebvre, F. De Geuser, C. Sigli, and A. Deschamps, “The effect of minor solute additions on the precipitation path of an Al Cu Li alloy,” *Acta Materialia*, vol. 115, pp. 104–114, Aug. 2016, doi: 10.1016/j.actamat.2016.05.050.
[57] E. Gumbmann, F. De Geuser, C. Sigli, and A. Deschamps, “Influence of Mg, Ag and Zn minor solute additions on the precipitation kinetics and strengthening of an Al-Cu-Li alloy,” *Acta Materialia*, vol. 133, pp. 172–185, Jul. 2017, doi: 10.1016/j.actamat.2017.05.029.
[58] B. Decreus, A. Deschamps, F. de Geuser, and C. Sigli, “Influence of Natural Ageing and Deformation on Precipitation in an Al-Cu-Li Alloy: Influence of Natural Ageing and Deformation on Precipitation…,” *Adv. Eng. Mater.*, vol. 15, no. 11, pp. 1082–1085, Nov. 2013, doi: 10.1002/adem.201300098.

[59] F. De Geuser and A. Deschamps, “Precipitate characterisation in metallic systems by small-angle X-ray or neutron scattering,” *Comptes Rendus Physique*, vol. 13, no. 3, pp. 246–256, Apr. 2012, doi: 10.1016/j.crhy.2011.12.008.
[60] G. Oertelt, S. Babu, S. David, and E. A. Kenik, “Effect of thermal cycling on friction stir welds of 2195 aluminum alloy,” *Welding journal*, vol. 80, pp. 71s–79s, Mar. 2001.
[61] T. F. Kelly and M. K. Miller, “Atom probe tomography,” *Review of Scientific Instruments*, vol. 78, no. 3, p. 031101, Mar. 2007, doi: 10.1063/1.2709758.
[62] D. B. Williams and C. B. Carter, *Transmission electron microscopy: a textbook for materials science*, 2nd ed. New York: Springer, 2008.
[63] W. Chen and P. Pareige, “Using atom probe tomography in the study of semiconductor nanowires,” in *Semiconductor Nanowires*, Elsevier, 2015, pp. 305–326. doi: 10.1016/B978-1-78242-253-2.00011-6.
[64] S. Esmaeili, X. Wang, D. J. Lloyd, and W. J. Poole, “On the precipitation-hardening behavior of the Al−Mg−Si−Cu alloy AA6111,” *Metall and Mat Trans A*, vol. 34, no. 13, pp. 751–763, Mar. 2003, doi: 10.1007/s11661-003-1003-2.
[65] Z. M. Wang and R. N. Shenoy, “Microstructural Characterization of Aluminum-Lithium Alloys 1460 and 2195.” Feb. 1998. [Online]. Available: https://ntrs.nasa.gov/citations/19980017087
[66] P. Panagos *et al.*, “Characterising precipitate evolution in multi-component cast aluminium alloys using small-angle X-ray scattering,” *Journal of Alloys and Compounds*, vol. 703, pp. 344–353, May 2017, doi: 10.1016/j.jallcom.2017.01.293.
[67] J. T. Buswell, E. A. Little, R. B. Jones, and R. N. Sinclair, “Proceedings of 2nd International Symposium on Environmental Degradation of Materials in Nuclear Reactors,” San Diego, CA, 1985.
[68] C. Genevois, A. Deschamps, A. Denquin, and B. Doisneaucottignies, “Quantitative investigation of precipitation and mechanical behaviour for AA2024 friction stir welds,” *Acta Materialia*, vol. 53, no. 8, pp. 2447–2458, May 2005, doi: 10.1016/j.actamat.2005.02.007.
[69] J. M. Papazian, “A calorimetric study of precipitation in aluminum alloy 2219,” *MTA*, vol. 12, no. 2, pp. 269–280, Feb. 1981, doi: 10.1007/BF02655200.
[70] J. M. Papazian, “Calorimetric Studies of Precipitation and Dissolution Kinetics in Aluminum Alloys 2219 and 7075,” *MTA*, vol. 13, no. 5, pp. 761–769, May 1982, doi: 10.1007/BF02642389.
[71] K. S. Arora, S. Pandey, M. Schaper, and R. Kumar, “Microstructure Evolution during Friction Stir Welding of Aluminum Alloy AA2219,” *Journal of Materials Science & Technology*, vol. 26, no. 8, pp. 747–753, Jan. 2010, doi: 10.1016/S1005-0302(10)60118-1.
[72] G. H. Li, L. Zhou, S. F. Luo, Z. Y. Du, J. C. Feng, and F. X. Meng, “Microstructure and mechanical properties of self-reacting friction stir welded AA2219-T87 aluminium alloy,” *Science and Technology of Welding and Joining*, vol. 25, no. 2, pp. 142–149, Feb. 2020, doi: 10.1080/13621718.2019.1648719.
[73] M. Khushaim, T. Boll, J. Seibert, F. Haider, and T. Al-Kassab, “Characterization of Precipitation in Al-Li Alloy AA2195 by means of Atom Probe Tomography and

Transmission Electron Microscopy," *Advances in Condensed Matter Physics*, vol. 2015, pp. 1–11, 2015, doi: 10.1155/2015/647468.
[74] M. Avalos-Borja, P. P. Pizzo, and L. A. Larson, "Transmission electron microscopy characterization of microstructural features of Al-Li-Cu alloys," 1983.
[75] P. Chen and B. Bhat, "Time-Temperature-Precipitation Behavior in Al-Li Alloy 2195," Mar. 2002.
[76] J. A. Schneider, A. C. Nunes, P. S. Chen, and G. Steele, "TEM study of the FSW nugget in AA2195-T81," *J Mater Sci*, vol. 40, no. 16, pp. 4341–4345, Aug. 2005, doi: 10.1007/s10853-005-2808-8.
[77] H. Qin, H. Zhang, and H. Wu, "The evolution of precipitation and microstructure in friction stir welded 2195-T8 Al–Li alloy," *Materials Science and Engineering: A*, vol. 626, pp. 322–329, Feb. 2015, doi: 10.1016/j.msea.2014.12.026.
[78] D. E. Taylor, "Effects of Processing Parameters on the Embrittlement of Self Reacting Friction Stir Welds," Master's Thesis, Louisiana State University, 2009.
[79] J. C. Lippold, *Welding metallurgy and weldability*. Hoboken, New Jersey: John Wiley & Sons Inc, 2015.
[80] G. Bjorkman, M. Cantrell, and R. Carter, "Self-Reacting Friction Stir Welding for Aluminum Alloy Circumferential Weld Applications," presented at the ASM Aeromat 2003, [Online]. Available: https://ntrs.nasa.gov/citations/20030061190
[81] VEQTER, "Neutron Diffraction." https://www.veqter.co.uk/residual-stress-measurement/neutron-diffraction
[82] A. Mohr and H. G. Priesmeyer, "Experimental correlation between the elemental composition and the lattice dimensions in alloys using AlCu as a model substance," presented at the 4th International Conference on Applications of Nuclear Techniques: Neutrons and their Applications, G. Vourvopoulos and T. Paradellis, Eds., Crete, Greece, Mar. 1995, pp. 350–355. doi: 10.1117/12.204176.
[83] J. D. Verhoeven, *Fundamentals of physical metallurgy*. New York: Wiley, 1975.
[84] M. Ashby and M. F. Ashby, Eds., *Engineering materials and processes desk reference*. Amsterdam: Elsevier, Butterworth-Heinemann, 2009.
[85] D. S. Sivia, *Elementary scattering theory: for X-ray and neutron users*. Oxford ; New York: Oxford University Press, 2011.
[86] C. Rabe, "Structural investigations using small angle scattering techniques and contrast variation," Humboldt-Universität zu Berlin, Berlin, 2014.
[87] N. Murthy, "Recent Developments in Small-Angle X-Ray Scattering," *Spectroscopy*, vol. 32, no. 11, pp. 18–24, Nov. 2017.
[88] M.-N. Avettand-Fènoël, F. De Geuser, and A. Deschamps, "Effect of the ageing on precipitation spatial distribution in stationary shoulder friction stir welded AA2050 alloys," *Materials Characterization*, vol. 154, pp. 193–199, Aug. 2019, doi: 10.1016/j.matchar.2019.06.006.
[89] J. F. dos Santos *et al.*, "Understanding precipitate evolution during friction stir welding of Al-Zn-Mg-Cu alloy through in-situ measurement coupled with simulation," *Acta Materialia*, vol. 148, pp. 163–172, Apr. 2018, doi: 10.1016/j.actamat.2018.01.020.

[90] F. Zhang *et al.*, “In situ structural characterization of ageing kinetics in aluminum alloy 2024 across angstrom-to-micrometer length scales,” *Acta Materialia*, vol. 111, pp. 385–398, Jun. 2016, doi: 10.1016/j.actamat.2016.03.058.
[91] B. Malard, F. De Geuser, and A. Deschamps, “Microstructure distribution in an AA2050 T34 friction stir weld and its evolution during post-welding heat treatment,” *Acta Materialia*, vol. 101, pp. 90–100, Dec. 2015, doi: 10.1016/j.actamat.2015.08.068.
[92] F. De Geuser, B. Malard, and A. Deschamps, “Microstructure mapping of a friction stir welded AA2050 Al–Li–Cu in the T8 state,” *Philosophical Magazine*, vol. 94, no. 13, pp. 1451–1462, May 2014, doi: 10.1080/14786435.2014.887862.
[93] A. Steuwer *et al.*, “A combined approach to microstructure mapping of an Al–Li AA2199 friction stir weld,” *Acta Materialia*, vol. 59, no. 8, pp. 3002–3011, May 2011, doi: 10.1016/j.actamat.2011.01.040.
[94] F. D. Geuser, F. Bley, A. Denquin, and A. Deschamps, “Mapping the microstructure of a friction-stir welded (FSW) Al-Li-Cu alloy,” *J. Phys.: Conf. Ser.*, vol. 247, p. 012034, Oct. 2010, doi: 10.1088/1742-6596/247/1/012034.
[95] A. Sullivan and J. D. Robson, “Microstructural properties of friction stir welded and post-weld heat-treated 7449 aluminium alloy thick plate,” *Materials Science and Engineering: A*, vol. 478, no. 1–2, pp. 351–360, Apr. 2008, doi: 10.1016/j.msea.2007.06.025.
[96] M. Dumont, A. Steuwer, A. Deschamps, M. Peel, and P. Withers, “Microstructure mapping in friction stir welds of 7449 aluminium alloy using SAXS,” *Acta Materialia*, vol. 54, no. 18, pp. 4793–4801, Oct. 2006, doi: 10.1016/j.actamat.2006.06.015.
[97] A. Sullivan, N. Kamp, and J. D. Robson, “Microstructural Evolution in AA7449 Plate Subject to Friction Stir Welding and Post Weld Heat Treatment,” *MSF*, vol. 519–521, pp. 1181–1186, Jul. 2006, doi: 10.4028/www.scientific.net/MSF.519-521.1181.
[98] M. Dumont, W. Lefebvre, B. Doisneau-Cottignies, and A. Deschamps, “Characterisation of the composition and volume fraction of η′ and η precipitates in an Al–Zn–Mg alloy by a combination of atom probe, small-angle X-ray scattering and transmission electron microscopy,” *Acta Materialia*, vol. 53, no. 10, pp. 2881–2892, Jun. 2005, doi: 10.1016/j.actamat.2005.03.004.
[99] G. Bokuchava, Y. Gorshkova, R. Fernández Serrano, G. González-Doncel, and G. Bruno, “Characterization of Precipitation in 2000 Series Aluminum Alloys using Neutron Diffraction, SANS and SEM Methods,” *Romanian Reports in Physics*, vol. 71, p. 502, Mar. 2019.
[100] H. Dawson *et al.*, “Impact of friction stir welding on the microstructure of ODS steel,” *Journal of Nuclear Materials*, vol. 486, pp. 129–137, Apr. 2017, doi: 10.1016/j.jnucmat.2016.12.033.
[101] D. Bardel *et al.*, “Coupled precipitation and yield strength modelling for non-isothermal treatments of a 6061 aluminium alloy,” *Acta Materialia*, vol. 62, pp. 129–140, Jan. 2014, doi: 10.1016/j.actamat.2013.09.041.
[102] M. West, B. Jasthi, P. Hosemann, and V. Sodesetti, “Friction Stir Welding of Oxide Dispersion Strengthened Alloy MA956,” in *Friction Stir Welding and*

Processing VI, R. Mishra, M. W. Mahoney, Y. Sato, Y. Hovanski, and R. Verma, Eds., Hoboken, NJ, USA: John Wiley & Sons, Inc., 2011, pp. 33–40. doi: 10.1002/9781118062302.ch5.
[103] A. Etienne, N. J. Cunningham, Y. Wu, and G. R. Odette, "Effects of friction stir welding and post-weld annealing on nanostructured ferritic alloy," *Materials Science and Technology*, vol. 27, no. 4, pp. 724–728, Apr. 2011, doi: 10.1179/1743284710Y.0000000038.
[104] M. H. Mathon, V. Klosek, Y. de Carlan, and L. Forest, "Study of PM2000 microstructure evolution following FSW process," *Journal of Nuclear Materials*, vol. 386–388, pp. 475–478, Apr. 2009, doi: 10.1016/j.jnucmat.2008.12.163.
[105] P. Miao *et al.*, "The microstructure and strength properties of MA957 nanostructured ferritic alloy joints produced by friction stir and electro-spark deposition welding," *Journal of Nuclear Materials*, vol. 367–370, pp. 1197–1202, Aug. 2007, doi: 10.1016/j.jnucmat.2007.03.232.
[106] R. Mishra and H. Sidhar, *Friction Stir Welding of 2XXX Aluminum Alloys Including Al-Li Alloys*. Elsevier, 2017. doi: 10.1016/C2015-0-04519-1.
[107] R. K. Gupta, R. Panda, A. K. Mukhopadhyay, A. K. V, P. Sankaravelayutham, and K. George, "Study of Aluminum Alloy AA2219 After Heat Treatment," *Metal Science and Heat Treatment*, vol. 57, Oct. 2015, doi: 10.1007/s11041-015-9888-0.
[108] H. J. Liu, J. C. Hou, and H. Guo, "Effect of welding speed on microstructure and mechanical properties of self-reacting friction stir welded 6061-T6 aluminum alloy," *Materials & Design*, vol. 50, pp. 872–878, Sep. 2013, doi: 10.1016/j.matdes.2013.03.105.
[109] L. Trueba, M. A. Torres, L. B. Johannes, and D. Rybicki, "Process optimization in the self-reacting friction stir welding of aluminum 6061-T6," *Int J Mater Form*, vol. 11, no. 4, pp. 559–570, Jul. 2018, doi: 10.1007/s12289-017-1365-4.
[110] A. L. Lafly, D. Alléhaux, F. Marie, C. Dalle Donne, and G. Biallas, "Microstructure and Mechanical Properties of the Aluminium Alloy 6056 Welded by Friction Stir Welding Techniques," *Weld World*, vol. 50, no. 11–12, pp. 98–106, Nov. 2006, doi: 10.1007/BF03263466.
[111] F. Marie, D. Allehaux, and B. Esmiller, "Development of the Bobbin Tool technique on various aluminium alloys," presented at the TWI's Fifth International Symposium on Friction Stir Welding, Metz, France, Sep. 2004.
[112] C. A. Schneider, W. S. Rasband, and K. W. Eliceiri, "NIH Image to ImageJ: 25 years of image analysis," *Nat Methods*, vol. 9, no. 7, pp. 671–675, Jul. 2012, doi: 10.1038/nmeth.2089.
[113] E04 Committee, "Test Methods for Determining Average Grain Size," ASTM International. doi: 10.1520/E0112-13R21.
[114] P. Cornwell, J. Bunn, C. M. Fancher, E. A. Payzant, and C. R. Hubbard, "Current capabilities of the residual stress diffractometer at the high flux isotope reactor," *Review of Scientific Instruments*, vol. 89, no. 9, p. 092804, Sep. 2018, doi: 10.1063/1.5037593.
[115] J. R. Bunn, C. M. Fancher, E. A. Payzant, P. A. Cornwell, W. B. Bailey, and R. Gregory, "The high intensity diffractometer for residual stress analysis (HIDRA), a third generation residual stress mapping neutron diffractometer at the high flux

isotope reactor," *Review of Scientific Instruments*, vol. 94, no. 3, p. 035101, Mar. 2023, doi: 10.1063/5.0122250.
[116] M. Popovici *et al.*, "Multiwafer focusing neutron monochromators and applications," presented at the International Symposium on Optical Science and Technology, J. L. Wood and I. S. Anderson, Eds., San Diego, CA, Nov. 2001, pp. 21–32. doi: 10.1117/12.448073.
[117] C. M. Fancher *et al.*, "*pyRS* : a user-friendly package for the reduction and analysis of neutron diffraction data measured at the High Intensity Diffractometer for Residual Stress Analysis," *J Appl Crystallogr*, vol. 54, no. 6, pp. 1886–1893, Dec. 2021, doi: 10.1107/S1600576721010554.
[118] J. R. Davis, Ed., *Metals Handbook Desk Edition*, 2nd ed. ASM International, 1998. doi: 10.31399/asm.hb.mhde2.9781627081993.
[119] W. Y. Li *et al.*, "Effects of tool rotational and welding speed on microstructure and mechanical properties of bobbin-tool friction-stir welded Mg AZ31," *Materials & Design*, vol. 64, pp. 714–720, Dec. 2014, doi: 10.1016/j.matdes.2014.07.023.
[120] D. Alléhaux and F. Marie, "Mechanical and Corrosion Behaviour of the 2139 Aluminium-Copper Alloy Welded by the Friction Stir Welding Using the Bobbin Tool Technique," *MSF*, vol. 519–521, pp. 1131–1138, Jul. 2006, doi: 10.4028/www.scientific.net/MSF.519-521.1131.
[121] K. Anderson, "Characterization of the evolution of 2219-T87 aluminum as a function of the self-reacting friction stir welding process," The University of Alabama, 2019. [Online]. Available: http://ir.ua.edu/handle/123456789/6481
[122] Q. Wen, W. Li, V. Patel, Y. Gao, and A. Vairis, "Investigation on the Effects of Welding Speed on Bobbin Tool Friction Stir Welding of 2219 Aluminum Alloy," *Met. Mater. Int.*, vol. 26, no. 12, pp. 1830–1840, Dec. 2020, doi: 10.1007/s12540-019-00450-9.
[123] S. Thangaraju, M. Heilmaier, B. S. Murty, and S. S. Vadlamani, "On the Estimation of True Hall-Petch Constants and Their Role on the Superposition Law Exponent in Al Alloys," *Adv. Eng. Mater.*, vol. 14, no. 10, pp. 892–897, Oct. 2012, doi: 10.1002/adem.201200114.
[124] B. D. Cullity and S. R. Stock, *Elements of X-ray diffraction*, 3. ed. Upper Saddle River, NJ: Prentice Hall, 2001.
[125] P. Virtanen *et al.*, "SciPy 1.0: fundamental algorithms for scientific computing in Python," *Nat Methods*, vol. 17, no. 3, pp. 261–272, Mar. 2020, doi: 10.1038/s41592-019-0686-2.
[126] W. Rietz, "Friction-Stir Welding - Heavy Inclusions in Bi-metallic welds of Al 2219/2195," ASM International, Pine Mountain, GA, 20080036591, Jun. 2008. [Online]. Available: https://ntrs.nasa.gov/api/citations/20080036591/downloads/20080036591.pdf
[127] S. Delijaicov *et al.*, "Microhardness and residual stress of dissimilar and thick aluminum plates AA7181-T7651 and AA7475-T7351 using bobbin, top, bottom, and double-sided FSW methods," *Int J Adv Manuf Technol*, vol. 108, no. 1–2, pp. 277–287, May 2020, doi: 10.1007/s00170-020-05370-2.

[128] H. Jamshidi Aval, “Microstructure and residual stress distributions in friction stir welding of dissimilar aluminium alloys,” *Materials & Design*, vol. 87, pp. 405–413, Dec. 2015, doi: 10.1016/j.matdes.2015.08.050.
[129] Q. Wen, W. Li, V. Patel, L. Bergmann, B. Klusemann, and J. F. dos Santos, “Assessing the Bonding Interface Characteristics and Mechanical Properties of Bobbin Tool Friction Stir Welded Dissimilar Aluminum Alloy Joints,” *Acta Metall. Sin. (Engl. Lett.)*, vol. 34, no. 1, pp. 125–134, Jan. 2021, doi: 10.1007/s40195-020-01101-4.
[130] M. Agilan, G. Phanikumar, and D. Sivakumar, “Tensile behaviour and microstructure evolution in friction stir welded 2195–2219 dissimilar aluminium alloy joints,” *Weld World*, vol. 66, no. 2, pp. 227–237, Feb. 2022, doi: 10.1007/s40194-021-01217-w.
[131] J. Altenkirch, A. Steuwer, M. J. Peel, and P. J. Withers, “The extent of relaxation of weld residual stresses on cutting out cross-weld test-pieces,” *Powder Diffr.*, vol. 24, no. S1, pp. S31–S36, Jun. 2009, doi: 10.1154/1.3152580.
[132] F. Geuser, B. Malard, and A. Deschamps, “Microstructure mapping of a friction stir welded AA2050 Al–Li–Cu in the T8 state,” *Philosophical Magazine*, vol. 94, Apr. 2014, doi: 10.1080/14786435.2014.887862.
[133] G. D. Wignall *et al.*, “The 40 m general purpose small-angle neutron scattering instrument at Oak Ridge National Laboratory,” *J Appl Crystallogr*, vol. 45, no. 5, pp. 990–998, Oct. 2012, doi: 10.1107/S0021889812027057.
[134] J. Ilavsky and P. R. Jemian, “*Irena* : tool suite for modeling and analysis of small-angle scattering,” *J Appl Crystallogr*, vol. 42, no. 2, pp. 347–353, Apr. 2009, doi: 10.1107/S0021889809002222.
[135] J. Ilavsky *et al.*, “Development of combined microstructure and structure characterization facility for *in situ* and *operando* studies at the Advanced Photon Source,” *J Appl Crystallogr*, vol. 51, no. 3, pp. 867–882, Jun. 2018, doi: 10.1107/S160057671800643X.
[136] J. Ilavsky, “*Nika* : software for two-dimensional data reduction,” *J Appl Crystallogr*, vol. 45, no. 2, pp. 324–328, Apr. 2012, doi: 10.1107/S0021889812004037.
[137] B. H. Toby and R. B. Von Dreele, “*GSAS-II* : the genesis of a modern open-source all purpose crystallography software package,” *J Appl Crystallogr*, vol. 46, no. 2, pp. 544–549, Apr. 2013, doi: 10.1107/S0021889813003531.
[138] L. B. McCusker, R. B. Von Dreele, D. E. Cox, D. Louër, and P. Scardi, “Rietveld refinement guidelines,” *J Appl Crystallogr*, vol. 32, no. 1, pp. 36–50, Feb. 1999, doi: 10.1107/S0021889898009856.
[139] J. M. Papazian, “Calorimetric Studies of Precipitation and Dissolution Kinetics in Aluminum Alloys 2219 and 7075,” *MTA*, vol. 13, no. 5, pp. 761–769, May 1982, doi: 10.1007/BF02642389.

VITA

Benjamin J. Wing was born in Oak Ridge, Tennessee to parents Scott and Christaline Wing. He is the eldest of three children with two younger brothers, Jonathan and Joseph. He received his bachelor's degree in Materials Science and Engineering with a minor in Chemistry from the University of Tennessee- Knoxville in 2013. Following graduation, he was employed as an Emergency Department scribe, trainer, and manager. In 2018, he returned to the University of Tennessee- Knoxville to pursue graduate studies in Materials Science and Engineering. He graduated with a master's degree in 2020 and a PhD in 2023. His dissertation is focused on the characterization of residual stress and precipitate evolution in aluminum 2xxx series self-reacting friction stir welds. Outside of his thesis project, Benjamin is an active member of the Oak Ridge Chapter of ASM where he serves as publicity chair.

Benjamin is currently pursuing postdoctoral positions.